ELECTRONIC STRUCTURE AND OPTICAL PROPERTIES OF MONOLAYER SEMICONDUCTORS: A COMPUTATIONAL STUDY

A DISSERTATION SUBMITTED TO

THE GRADUATE SCHOOL OF ENGINEERING AND SCIENCE

OF BILKENT UNIVERSITY

IN PARTIAL FULFILLMENT OF THE REQUIREMENTS FOR

THE DEGREE OF

DOCTOR OF PHILOSOPHY

IN

PHYSICS

By

Yağmur Aksu Korkmaz

September 2021

ELECTRONIC STRUCTURE AND OPTICAL PROPERTIES OF MONOLAYER SEMICONDUCTORS: A COMPUTATIONAL STUDY

By Yağmur Aksu Korkmaz

September 2021

We certify that we have read this dissertation and that in our opinion it is fully adequate, in scope and in quality, as a dissertation for the degree of Doctor of Philosophy.

Ceyhun Bulutay(Advisor)

Cem Sevik(Co-Advisor)

Oğuz Gülseren

Bekir Sıtkı Kandemir

Engin Durgun

Mehmet Emre Taşgın

Approved for the Graduate School of Engineering and Science:

Ezhan Karaşan
Director of the Graduate School

ABSTRACT

ELECTRONIC STRUCTURE AND OPTICAL PROPERTIES OF MONOLAYER SEMICONDUCTORS: A COMPUTATIONAL STUDY

Yağmur Aksu Korkmaz
Ph.D. in Physics
Advisor: Ceyhun Bulutay
Co-Advisor: Cem Sevik
September 2021

Interest on monolayer semiconductors is rapidly growing in recent years. One of the prominent members is hexagonal boron nitride (h-BN). At room temperature, it harbors an environment similar to semiconductor vacuum for point defects which is crucial for stable and controllable spin states. This qualification makes h-BN a suitable medium for quantum technological applications. First-principles calculations are essential in order to characterize such systems. Density functional theory (DFT) is one of the most reliable methods used for these type of calculations. Recently, a variant called as DFT-1/2, has been proposed to calculate the band gaps of the materials more accurately without a significant additional computational cost. In the first part of thesis, we have compared the results of DFT and DFT-1/2 for carbon impurities (C_B, C_N), single vacancies (V_B, V_N), double vacancy (divacancy) and Stone-Wales defect in monolayer h-BN. Subsequently, results from computationally expensive techniques such as hybrid or GW are presented and compared with the obtained DFT-1/2 results. Especially for the defect states seemingly hidden in valence or conduction band, DFT-1/2 technique is instrumental in revealing these states while widening the band gap. Thus, we recommend the DFT-1/2 method for a quick screening of candidate band gap defect states.

Another outstanding group of semiconductors is transition metal dichalcogenides (TMDs). They owe their advantages to optically addressable valley and bringing optics and mechanics together as in valleytronics, thanks to their high flexibility. In the second part of this thesis, ten TMDs including their janus counterparts (JTMDs), namely, MoS_2, $MoSe_2$, $MoTe_2$, WS_2, WSe_2, WTe_2, MoSSe, MoSeTe, WSSe, and WSeTe have been computationally studied. To begin with, the electronic band structure of the specified materials have been computed using DFT followed by hybrid calculations over these, with the addition of spin-orbit

coupling. Biaxial and uniaxial strain calculations are subsequently performed. JTMDs were previously proclaimed to have a good piezoelectric characteristic. According to our DFT results, JTMDs exhibit band structure and electronic properties in between its constituent TMDs, and in this respect they do not display an outstanding behaviour. Based on the acquired DFT data, spinless and spinful $\mathbf{k}\cdot\mathbf{p}$ parameters are extracted by fitting around optically active K valley. With the help of $\mathbf{k}\cdot\mathbf{p}$ parametrization, linear and circular dichroic behaviours are studied for unstrained and strained cases. In consideration of all these materials, WTe_2 displays the largest linear dichroic responsitivity for uniaxial strain, since it has the smallest band gap and the greatest uniaxial deformation potential at the K valley. Thus, we propose monolayer WTe_2 membranes to be considered for optical polarization based strain measurements, as well as, strain adjustable optical polarizers.

Keywords: hBN, Density functional theory, Two dimensional materials, Defect, Vacancy, k.p method, (Janus) Transition metal dichalcogenide, linear and circular dichroism.

ÖZET

TEK KATMANLI YARI İLETKENLERİN ELEKTRONİK VE OPTİK ÖZELLİKLERİ: HESAPLAMALI BİR ÇALIŞMA

Yağmur Aksu Korkmaz
Fizik, Doktora
Tez Danışmanı: Ceyhun Bulutay
İkinci Tez Danışmanı: Cem Sevik
Eylül 2021

Son yıllarda, tek katmanlı yarı iletkenlere olan ilgi hızla artmaktadır. Altıgen boron nitrit (h-BN) bu grubun önemli üyelerinden biridir. Oda sıcaklığında boron nitrit, nokta kusurları için yarı iletken vakuma benzer bir ortam sağlamaktadır ki bu durum istikrarlı ve kontrol edilebilen spin durumları için son derece caziptir. Bu özellik, h-BN'i kuantum teknolojik uygulamalar için uygun bir ortam haline getirmektedir. Temel ilkeler yöntemleri bu türden sistemlerin karakteristiğini hesaplamak için gereklidir. Yoğunluk fonksiyon teorisi (YFT) bu tip hesaplamalar için kullanılan güvenilir metodların başındadır. Yakın zaman önce, malzemelerin bant aralığını kayda değer bir ek kaynak gerektirmeden daha isabetli bir şekilde hesaplamak için, YFT-1/2 olarak bilinen bir türev önerilmiştir. Tezin ilk kısmında, tek katmanlı h-BN içerisindeki karbon safsızlığı (C_B, C_N), tek atom boşlukları (V_B, V_N), çift atom boşluğu (divacancy) ve Stone-Wales kusuru için YFT ve YFT-1/2 sonuçları karşılaştırılmıştır. Peşi sıra, hibrit veya GW gibi hesaplama açısından pahalı olan tekniklerle elde edilmiş yayınlanmış sonuçlar derlenerek ve YFT-1/2 ile elde edilen sonuçlarla karşılaştırılmıştır. Bilhassa, değerlik ve iletim bandında gizlenmiş olan kusur seviyeleri için, YFT-1/2 tekniğinin bant aralığını arttırarak bu seviyeleri ortaya çıkarma konusunda etkin olduğu tespit edilmiştir. Dolayısıyla, bant aralığında bulunan kusur seviyelerinin hızlı bir tasnifi için, YFT-1/2 metodunun kullanılmasını öneriyoruz.

Geçiş metal dikalkojenleri (GMDler), yarı iletkenler arasında önde gelen gruplardan bir diğeridir. Bunu, hem esnek hem de optik olarak erişilebilir vadileri sayesinde optik ve mekanik üstünlükleri bir arada barındırmalarına borçludurlar. Tezin ikinci kısmında, iki yüzlü türleri (İYGMDler) ile beraber 10 adet GMDini, yani, MoS_2, $MoSe_2$, $MoTe_2$, WS_2, WSe_2, WTe_2, MoSSe, MoSeTe, WSSe,

ve WSeTe'u hesaplamalı olarak çalıştık. Öncelikli olarak, bu malzemelerin elektronik bant yapısını, YFT ve üzerine hibrit hesaplarıyla spin-yörünge etkileşimi de ekleyerek elde ettik. Devamında, çift ve tek eksenli gerilme hesaplarını yaptık. İYGMDlerinin iyi bir piezoelektrik karakteristiğine sahip olduğu daha önce beyan edilmiştir. Kendi YFT sonuçlarımıza göre, İYGMDleri, bant yapısı ve elektronik özellikleri düşünüldüğünde, iki GMD bileşenlerinin arasında sonuçlar göstermektedir ve bu itibarla sıra dışı bir davranışları gözlemlenmemiştir. Optik olarak etkin K vadisi cevresine uydurularak, elde edilen YFT verisi ile spinsiz ve spinli $\mathbf{k} \cdot \mathbf{p}$ parametreleri elde edilmiştir. $\mathbf{k} \cdot \mathbf{p}$ parametrizasyonun yardımı ile, gerilmesiz ve gerilmeli durumlar için, çizgisel ve dairesel çiftrenkli davranışlar çalışılmıştır. Bütün bu malzemeler dikkate alındığında, en küçük bant aralığına ve K vadisinde en büyük tek eksenli gerilme potansiyeline sahip olmasıyla birlikte, WTe_2 tek eksenli gerilme altında en büyük çizgisel çiftrenkli duyarlılığı sergilemiştir. Nitekim, gerilmeyle ayarlanabilen optik polarizasyonların yanı sıra optik polarizasyon tabanlı gerilme ölçümleri için de WTe_2 zarlarının denemesini tavsiye ediyoruz.

Anahtar sözcükler: hBN, Yoğunluk fonksiyon teorisi, İki boyutlu malzemeler, Kusur, Atom boşluğu, k.p metodu, (İki yüzlü) Geçiş Metal Dikalkojeni, Çizgisel ve dairesel çiftrenklilik.

Acknowledgement

I would like to thank my advisor Prof. Ceyhun Bulutay and co-advisor Prof. Cem Sevik for their guidance throughout my research and their help with the struggles of my PhD life.

I would like to thank my Thesis Committee members Prof. Oğuz Gülseren, Prof. Bekir Sıtkı Kandemir, Prof. Engin Durgun and Prof. Mehmet Emre Taşgın for their advices that moved my thesis one step further.

I would like to thank Bilkent Physics Department for giving the opportunity to complete my graduate studies.

I would also like to thank TUBITAK ULAKBIM for providing an environment to fully perform the numerical calculations reported in this thesis at, High Performance and Grid Computing Center (TRUBA resources).

I am grateful to my colleagues for their support during my time in Bilkent Physics Department.

I am very thankful to my mother Nevin, my father Yılmaz and my sister Selin for their endless love and support along with my life. I would also like to thank my cat Halley for her love. Finally, I want to thank my husband Mustafa for his love, patience and encouragement through my life.

Contents

1 Introduction **1**

1.1 h-BN Defects with DFT-1/2 1

1.2 (J)TMDs with $\mathbf{k} \cdot \mathbf{p}$ Method 3

2 DFT 1/2 Method and Applications **7**

2.1 Theory 7

2.1.1 Exchange-Correlation Effects 7

2.1.2 Basics of the DFT-1/2 Variant 10

2.2 Our DFT-1/2 Results 13

2.3 h-BN defects: DFT vs DFT-1/2 14

2.3.1 Carbon Impurities 15

2.3.2 Vacancies 17

2.3.3 Stone-Wales Defect 22

2.4 Computational Budget Comparison With Higher Order Methods . 24

3 Pristine and Janus Transition Metal Dichalcogenides with $\mathbf{k} \cdot \mathbf{p}$ Method **28**

3.1 Theory 28

3.1.1 Parameter Fitting Expressions 30

3.1.2 Dichroism within $\mathbf{k} \cdot \mathbf{p}$ Hamiltonian 31

3.1.3 $\partial\mathcal{H}/\partial k_\epsilon$ Expressions 32

3.1.4 Approximate Analytical Expressions 33

3.2 Results 34

3.2.1 DFT Results 34

3.2.2 $\mathbf{k} \cdot \mathbf{p}$ Results 38

4 Conclusions **49**
4.1 h-BN Defects with DFT-1/2 49
4.2 (J)TMDs with $\mathbf{k}\cdot\mathbf{p}$ Method 50
4.3 Suggestions for further research 50

A h-BN Defects with DFT and DFT-1/2 **69**
A.1 Computational Details 69
A.2 Tables For Defect Energies For Small and Large Supercells 70
A.3 Electronic Band Structures with PBE and PBE-1/2 71
A.4 Electronic Band Structures with HSE and LDA-1/2 79
A.5 Additional Electronic Band Structures of C_N defect 81

B (Janus) Transition Metal Dichalcogenides with $\mathbf{k}\cdot\mathbf{p}$ Method **83**
B.1 Computational Details 83
B.2 DFT Results w/o SOC for TMDs 84
B.3 DFT Results Under Strain 85
B.4 $\mathbf{k}\cdot\mathbf{p}$ vs DFT Spinless Results for MX_2 and MXX' 93
B.5 Dichroism Results 99
B.6 Effective Mass, DFT and $\mathbf{k}\cdot\mathbf{p}$ and Tables 106

List of Figures

2.1 Band gap vs. *CUT* graph for BN. 14
2.2 Band structure for monolayer *h*-BN pristine calculated with (a) LDA (blue) and LDA-1/2 (red) (b) PBE (blue) and PBE-1/2 (red). 15
2.3 Schematic representation of carbon impurities (C_B, C_N), single vacancies (V_B, V_N), double vacancy (DV) and Stone-Wales (SW) defect. B, N and C atoms are colored in green, grey and brown. . 16
2.4 C_B defect energy levels placed in the band gap (not to scale) calculated with LDA, LDA-1/2, PBE and PBE-1/2. 17
2.5 C_N defect energy levels placed in the band gap (not to scale) calculated with LDA, LDA-1/2 with N only, LDA-1/2 with N and C, PBE, PBE-1/2 with N only, and PBE-1/2 with N and C. 18
2.6 V_N defect energy levels placed in the band gap (not to scale) calculated with LDA, LDA-1/2, PBE and PBE-1/2. 19
2.7 Electronic band structures and charge densities near CB (blue) with spin up V_N state (red) with LDA (left) and LDA-1/2 (right). B and N atoms are colored in green and grey. 20
2.8 V_B defect energy levels placed in the band gap (not to scale) calculated with LDA, LDA-1/2, PBE and PBE-1/2. Here, the Fermi level is set to spin up HOMO. 21
2.9 Electronic band structures and charge densities near VB (blue) with spin up V_B state (red) with PBE (left) and PBE-1/2 (right). B and N atoms are colored in green and grey. 22
2.10 DV defect energy levels placed in the band gap (not to scale) calculated with LDA, LDA-1/2, PBE and PBE-1/2. 23

2.11 SW defect energy levels placed in the band gap (not to scale) calculated with LDA, LDA-1/2, PBE and PBE-1/2. 24
2.12 Band structure around VB (blue) including SW defect for spin up state (red) with LDA (left) and LDA-1/2 (right) and their charge densities. B and N atoms are colored in green and grey. 25

3.1 The electronic band structures of MoXX' and WXX' with PBE (gray/dashed) and PBE+SOC (blue/solid). 35
3.2 The band structure change of MXX' under (a) biaxial strain (b) uniaxial strain. 38
3.3 (a) Top and side view of JTMDs. (b) High symmetry points corresponding for hexagonal and orthorhombic (tetragonal) lattice, respectively. 39
3.4 Spin up bands with SOC for $\mathbf{k}\cdot\mathbf{p}$ (solid lines) vs DFT(•). 40
3.5 Spin down bands with SOC for $\mathbf{k}\cdot\mathbf{p}$ (solid lines) vs DFT(•). . . . 41
3.6 Isoenergy contours with SOC for $\mathbf{k}\cdot\mathbf{p}$ (solid lines) vs DFT (dashed lines) for spin up case at K valley. The energies (0.025, 0.05, 0.1, 0.15, 0.2 eV) are represented with (black, blue, turquoise, red and green lines). 42
3.7 Isoenergy contours with SOC for $\mathbf{k}\cdot\mathbf{p}$ (solid lines) vs DFT (dashed lines) for spin down case at K valley. The energies (0.025, 0.05, 0.1, 0.15, 0.2 eV) are represented with (black, blue, turquoise, red and green lines). 43
3.8 The linear dichroism variation under uniaxial-only strain at the K point for the spin-down transition (left). $\eta_L(\epsilon_{xx} = 0.1)$ and transition energy values for the ten (J)TMDs (right). 44
3.9 For WSe_2, WTe_2, and janus WSeTe spin-down transition, (a) the linear and circular dichroism variation ($\eta_{L,C}$) at K valley without strain and the deviation from unstrained case ($\Delta\eta_{L,C}$) at K point under (b) biaxial-only, (c) uniaxial-only, (d) shear-only strain. $[-0.25, +0.25]$ square area around the K point in 1/Å along each direction is demonstrated. 46
3.10 Identical calculations are considered with previous figure, except the trigonal warping term of the $\mathbf{k}\cdot\mathbf{p}$ Hamiltonian is not included. 47

A.1 Band structure and DOS for C_B defect spin up (left) and spin down (right) calculated with (a) PBE and (b) PBE-1/2. 73
A.2 Band structure and DOS for C_N defect spin up (left) and spin down (right) calculated with (a) PBE and (b) PBE-1/2. 74
A.3 Band structure and DOS for V_N defect spin up (left) and spin down (right) calculated with (a) PBE and (b) PBE-1/2. 75
A.4 Band structure and DOS for V_B defect spin up (left) and spin down (right) calculated with (a) PBE and (b) PBE-1/2. 76
A.5 Band structure and DOS for DV defect spin up (left) and spin down (right) calculated with (a) PBE and (b) PBE-1/2. 77
A.6 Band structure and DOS for SW defect spin up (left) and spin down (right) calculated with (a) PBE and (b) PBE-1/2. 78
A.7 HSE06 and LDA-1/2 electronic band structure for C_B (left) and C_N (right) defects. 79
A.8 HSE06 and LDA-1/2 electronic band structure for V_N (left) and V_B (right) defects. 80
A.9 HSE06 and LDA-1/2 electronic band structure for DV (left) and SW (right) defects. 80
A.10 PBE-1/2 (left) and LDA-1/2 (right) C_N spin polarized band structures of with C and N correction. 81
A.11 PBE-1/2 (left) and LDA-1/2 (right) C_N spin polarized band structures of with only N correction. 82

B.1 The electronic band structures calculated with PBE(gray dashed lines) and PBE+SOC (dark blue solid lines) for MX_2 and WX_2. . 84
B.2 MoS_2, $MoSe_2$, $MoTe_2$ band structures under -2%,-1%,1%,2% biaxial strain vs without strain. 85
B.3 WS_2, WSe_2, WTe_2 with -2%,-1%,1%,2% band structures under -2%,-1%,1%,2% biaxial strain vs without strain. 86
B.4 MoSSe, MoSTe, MoSeTe band structures under -2%,-1%,1%,2% biaxial strain vs without strain. 87
B.5 WSSe, WSTe, WSeTe band structures under -2%,-1%,1%,2% biaxial strain vs without strain. 88

B.6 MoS_2, $MoSe_2$, $MoTe_2$ band structures under -2%,-1%,1%,2% uniaxial strain vs without strain. 89
B.7 Band graphs of WS_2, WSe_2, WTe_2 band structures under -2%,-1%,1%,2% uniaxial strain vs without strain. 90
B.8 Band graphs of MoSSe, MoSTe, MoSeTe band structures under -2%,-1%,1%,2% uniaxial strain vs without strain. 91
B.9 Band graphs of WSSe, WSTe, WSeTe band structures under -2%,-1%,1%,2% uniaxial strain vs without strain. 92
B.10 MoX_2 and WX_2 spinless band structures with $\mathbf{k}\cdot\mathbf{p}$ (solid lines) vs DFT(•). 93
B.11 $MoXX'$ and WXX' spinless band structures with $\mathbf{k}\cdot\mathbf{p}$ (solid lines) vs DFT(•). 94
B.12 MoX_2 and WX_2 isoenergy contours with $\mathbf{k}\cdot\mathbf{p}$ (solid lines) vs DFT (dashed lines) for spinless case at K valley. The energies (0.025, 0.05, 0.1, 0.15, 0.2 eV) are represented with (black, blue, turquoise, red and green lines). 95
B.13 $MoXX'$ and WXX' isoenergy contours with $\mathbf{k}\cdot\mathbf{p}$ (solid lines) vs DFT (dashed lines) for spinless case at K valley. The energies (0.025, 0.05, 0.1, 0.15, 0.2 eV) are represented with (black, blue, turquoise, red and green lines). 95
B.14 MoX_2 and WX_2 spin up band structures with $\mathbf{k}\cdot\mathbf{p}$ (solid lines) vs DFT(•). 96
B.15 MoX_2 and WX_2 spin down band structures with $\mathbf{k}\cdot\mathbf{p}$ (solid lines) vs DFT(•). 97
B.16 MoX_2 and WX_2 isoenergy contours with $\mathbf{k}\cdot\mathbf{p}$ (solid lines) vs DFT (dashed lines) for spin up case at K valley. The energies (0.025, 0.05, 0.1, 0.15, 0.2 eV) are represented with (black, blue, turquoise, red and green lines). 98
B.17 MoX_2 and WX_2 isoenergy contours with $\mathbf{k}\cdot\mathbf{p}$ (solid lines) vs DFT (dashed lines) for spin down case at K valley. The energies (0.025, 0.05, 0.1, 0.15, 0.2 eV) are represented with (black, blue, turquoise, red and green lines). 98

B.18 The linear dichroism (with spinless Hamiltonian) variation under uniaxial-only strain at the K point for the spin-down transition (left). $\eta_L(\epsilon_{xx} = 0.1)$ and transition energy values for the ten (J)TMDs (right). 99
B.19 In order to compare our results in Fig. 3.9(b) with Ref. [141], for monolayer MoS_2 without strain, circular dichroism (η_C) is calculated with including (a) only the symmetric and asymmetric terms (b) the trigonal warping term (c) all terms. $[-0.3, +0.3]$ square area around the K point in $\sqrt{3}/a$ units with a is the lattice constant along each direction is demonstrated. 99
B.20 For WSe_2, WTe_2, and janus WSeTe with spinless Hamiltonian, (a) the linear and circular dichroism variation ($\eta_{L,C}$) at K valley without strain and the deviation from unstrained case ($\Delta\eta_{L,C}$) at K point under (b) biaxial-only, (c) uniaxial-only, (d) shear-only strain. 100
B.21 For WSe_2, WTe_2, and janus WSeTe with only the symmetric term included for spin down transition, (a) the linear and circular dichroism variation ($\eta_{L,C}$) at K valley without strain and the deviation from unstrained case ($\Delta\eta_{L,C}$) at K point under (b) biaxial-only, (c) uniaxial-only, (d) shear-only strain. 101
B.22 Identical calculations are considered with previous figure, with symmetric and asymmetric terms of the $\mathbf{k} \cdot \mathbf{p}$ Hamiltonian are included together. 102
B.23 For MoS_2, $MoSe_2$ and their janus MoSSe spin-down transition, (a) the linear and circular dichroism variation ($\eta_{L,C}$) at K valley without strain and the deviation from unstrained case ($\Delta\eta_{L,C}$) at K point under (b) biaxial-only, (c) uniaxial-only, (d) shear-only strain. 103
B.24 Identical calculations are considered with previous figure, but for $MoSe_2$, $MoTe_2$ and their Janus MoSeTe. 104
B.25 Identical calculations are considered with previous figure, but for WS_2, WSe_2 and their Janus WSSe. 105

List of Tables

2.1 Band gaps calculated for AlN, BN, GaN and InN using DFT and DFT-1/2. 13

2.2 Band gaps from previous studies for AlN, BN, GaN and InN using HSE, *GW* and PBE-1/2. 13

2.3 2D *h*-BN spin polarized defect energies. VBM is chosen as the reference point of the defect energy measurements. For HSE calculations, * is used for states lost in CB. 26

3.1 Band Gaps Calculated with PBE and HSE compared with and without SOC where the band gaps refer to KK points for direct materials and ΓK points for indirect materials designated with I (MoSTe and WSTe). 36

3.2 Splittings in CB and VB calculated with PBE and HSE[a] where the splittings are calculated at K point for CB and VB, except for MoSTe and WSTe at Γ point for VB. For all splitting calculations $E^{\downarrow}_{\mathrm{CB/VB}} - E^{\uparrow}_{\mathrm{CB/VB}}$ formula is used. 37

3.3 Spinless $\mathbf{k}\cdot\mathbf{p}$ parameters a (Å) f_1 (eV), f_2 (eV), f_4 (eV), f_5 (eV), α (eV Å^2), β (eV Å^2), κ (eV Å^2) and η (eV Å^3). 39

3.4 Spinful $\mathbf{k}\cdot\mathbf{p}$ parameters f_1 (eV), f_2 (eV), α (eV Å^2), β (eV Å^2), κ (eV Å^2) and η (eV Å^3). 42

A.1 Spin polarized defect states calculated with LDA for small and large supercells where energies are aligned from HOMO level. . . . 71

A.2 Spin polarized defect states calculated with LDA-1/2 for small and large supercells where energies are aligned from HOMO level. . . . 71

A.3 Spin polarized defect states calculated with PBE for small and large supercells where energies are aligned from HOMO level. . . . 72
A.4 Spin polarized defect states calculated with PBE-1/2 for small and large supercells where energies are aligned from HOMO level. . . . 72

B.1 (J)TMD effective masses with and without SOC in units of m_0. . 106
B.2 Band gaps with -2%,-1%-0%,1%,2% biaxial strain (in eV units). . 107
B.3 Band gaps with biaxial strain and 0% strain with HSE over PBE (in eV units). 107
B.4 Band gaps with -2%,-1%-0%,1%,2% uniaxial strain (along x axis) (in eV units). 108
B.5 Band gaps with uniaxial strain (along x axis) and 0% strain with HSE over PBE (in eV units). 108
B.6 $\mathbf{k} \cdot \mathbf{p}$ parameters f_4 and f_5 calculated based on PBE and HSE results (in eV units). 109

Chapter 1

Introduction

1.1 *h*-BN Defects with DFT-1/2

For single photon emitters and optically addressable qubits, defect centers in semiconductors with a large band gap are promising candidates [1, 2, 3, 4, 5]. Specific to each environment, distinctive characteristic electronic structure arises for varied defect types. For this purpose, the density functional theory (DFT) [6] is widely preferred for band structure calculations of solid state materials. Here, the holy grail is how to account for the exchange-correlation energy. Most commonly, generalize gradient approximation (GGA) [7] and localized density approximation (LDA) [8] are preferred. Even though, these approximations produce results which are mostly in fair agreement with experiments, they find the band gap energies smaller [9]. This is a major obstacle to achieve accurate calculations for optical properties. Hybrid functional (HSE) [10] over regular DFT calculations of *GW* [11] quasiparticle approach, increase the precision of numerical calculations. However, they increase the necessary computational time and memory at the same time, when compared with the regular DFT counterpart.

A simple improvement over LDA and GGA is offered by Ferreira, Marques and Teles [12] which is called as DFT-1/2 technique. This method is inspired by

self-consistent Kohn-Sham DFT method [13] and transition state concept proposed by Slater [14] which is adopted for DFT by Janak [15]. DFT-1/2 method (can be specialized as LDA-1/2 or GGA-1/2) requires one additional step over regular DFT. A parameter called CUT is determined and used for correction of self-energy potential so that it eventually modifies the elemental pseudopotential. With this step, DFT-1/2 produces enhanced band gap values without using more computational resources than DFT. Extra information over the theory is available from section 2.1 and relevant papers [12, 16]. Various studies adopted this simple yet effective method for popular materials to find the band structures and band gaps more precisely [16, 17, 18, 19, 20, 21]. One of the recent studies, Guilhon et. al [22] developed this method further in order to get correct band gaps for 2D materials and they achieved results very close to GW [23]. LDA and PBE calculations found the band gap of 2D h-BN 4.61 eV [23, 24] and 4.74 eV [25] while GGA-1/2 enhances the value up to 6.62 eV [22]. HSE calculation get this value as 5.68 eV [26] which is still the closest value among all compared with experimentally measured 6 eV [27].

DFT-1/2 technique has been further improved over the years. Xue et. al [28] put attention on Group IV covalently bonded semiconductors such as diamond, Ge, Si etc. and propose removing 1/4 electron with additional correction to self energy potential for these materials. Another work [21] pointed out that, for antiferromagnetic transition-metal oxides, DFT-1/2 does not conduct the band gap development as well as the materials presented in the original work. Spatial separation of the conduction and valence bands might be the barrier in front of this enhancement. Regardlessly, this postulate of DFT-1/2 achieves a good improvement over Group III-V semiconductors [12, 16].

Point defects using LDA-1/2 or GGA-1/2 are also studied [29, 30] besides the pristine systems. Similarly, NV center in diamond is investigated by Lucatto et. al [31] using GGA-1/2. Defects in h-BN may be a good candidate for accomplishing such a work, since it has a large band gap and it is efficient as a single photon emitter [32, 33, 34, 35, 36]. Vacancy and doping defects [37, 38, 39, 40, 41, 42, 43, 44, 45, 46, 47, 48, 49, 50, 51, 52, 53, 54, 55, 56, 57, 58] should be investigated genuinely so as to give a chance on discovering the quantum emission process in detail [59, 60]. Up to now, using GW [38], constrained DFT, DFT,

charge transition levels [61, 62], zero phonon line [59] and hyperfine tensors [63] are identified. Yet, a study using DFT-1/2 over monolayer h-BN defects is not present.

In this thesis, using GGA-1/2 and LDA-1/2, we have examined the energy spectra of various neutral defects for monolayer h-BN. Starting our work with carbon impurities of C_B and C_N, we have continued with single vacancies V_B and V_N, double vacancy (DV), finally investigated Stone-Wales (SW) defect. Considering the electronegativity opposition of B and N atoms [12], we have only modified self-energy potential of N atom for DFT-1/2 technique. However, consideration of the electronegativity of C which is close to both B and N, creates and ambiguity [28]. For the special case of C substitution with N atom, correction to both of the atoms has been considered for our calculation, where no numeral changes have been observed. Additionally, we have added HSE and GW results in order to compare with DFT-1/2. This also helped to understand the computational cost differences of disparate methods. LDA-1/2 is found to be an effective technique for revealing the defect states buried inside of CB or VB, which is the main finding of this part.

1.2 (J)TMDs with $\mathbf{k} \cdot \mathbf{p}$ Method

Transition metal dichalcogenides (TMDs) are constructed by placing a metal M atom (M = Mo, W, etc.) layer between two chalcogene X atom (X = S, Se, or Te) layers. Considering their physical properties [64], This type of 2D materials have been studied greatly. They are proposed as potential optical emitters [65] and transistors [66, 67] by their semiconductor characteristics. Moreover, research areas such as photodetectors [68], phototransistors, piezotronics [69], valleytronics [70, 71] over TMDs have gained interest. A new type of TMD (MX_2) called Janus TMD (MXX') [72, 73] are formed similarly to the pristine TMDs. Here, two different chalcogene atoms are used to form these type of materials and they are fabricated experimentally by using chemical vapor deposition (CVD) technique [74, 75]. MoSSe is constructed by either selenizing or sulfurizing one of the

chalcogene layers. This process causes out-of plane mirror symmetry breaking for JTMD materials and encourages piezoelectric behaviour [76].

Recently published experimental research shows that strain can be used as a parameter of controlling the optical and dynamical properties of JTMD heterostructures such as $MoSSe/MoS_2$, MoSSe/WSSe, and WSSe/MoSSe [77, 78, 79]. Numerous theoretical studies are available for (J)TMDs on flexoelectric [80], piezoelectric [76, 81],transport [82, 83, 84] and optical [85] physical features. Possible applications for these materials can be listed as solar power harvesting [86, 87, 88, 89, 90], water splitting [91, 92, 93, 94, 95, 96], optoelectronics [97, 98, 99], gas sensing [100, 101, 102, 103] and valleytronics [104, 105, 106].

Yet, strain analysis with optical-polarization and polarization photodetection with high-accuracy, remains unnoticed but carry potential for (J)TMDs. Remembering that polarization is an important feature of an electromagnetic wave, such as its wavelength, strain dependence can be used to control the materials with dichroic behaviour. This type of the materials exhibit good absorption in accordance with the polarization of the resonant photon. TMDs have exhibited a robust valley selective circular dichroism (CD) along with the broken C_3 symmetry [107, 108, 109, 110, 70, 71]. Alternatively, valley Zeeman effect [111, 112] is another feature caused by nonzero Berry curvature [71, 113]. One of the areas that CD is employed in TMDs is photosensitive meta-materials [114]. Different from CD, in case of linear dichroism (LD), the absorption is distinguished for two orthogonal linear polarizations. At the K point of CBM and VBM, pristine TMDs have in-plane symmetry that causes the LD to vanish. With uniaxial strain, the point group symmetry of TMDs change from D_{3h} to C_{2v}, which is causing LD as a non-vanishing property and turning these materials into possible polarization based photodetectors with effective performance [115].

The DFT method [116, 117, 10] is one of the most preferred technique on theoretical calculations in this area. However, the computational cost increases for the situations such as, getting the correct band gap, the calculations with spin-orbit coupling addition, or systems under strain. $\mathbf{k} \cdot \mathbf{p}$ method is an alternative to DFT, which is simple yet effective on characterizing the electronic and optical properties [118]. Correct parametrization is critical for this technique. Up to

now, several studies have been achieved on monolayer TMD $\mathbf{k} \cdot \mathbf{p}$ parametrization [119, 120, 121, 122, 123, 113], however (J)TMDs aren't investigated by this technique.

In this thesis, the electronic and optical features of ten different monolayer (J)TMDs are calculated: MoS_2, $MoSe_2$, $MoTe_2$, WS_2, WSe_2, WTe_2, MoSSe, MoSeTe, WSSe, and WSeTe. To begin with, the electronic band structures with DFT and HSE with SOC have been calculated. Next, inspired by the strain effects over (J)TMDs [124], the change at K valley, that is created by uniaxial and biaxial strain, is examined. Using these DFT results, $\mathbf{k} \cdot \mathbf{p}$ parameters are acquired for spinless and spinful cases. In order to get an accurate fit at K valley, electron-hole asymmetry, triagonal warping, cubic terms [119, 120] are added, and then strain term [123] is included. Lastly, CD and LD features of (J)TMDs are explored by using the $\mathbf{k} \cdot \mathbf{p}$ band structure obtained previously. Our main discovery is, among all the materials, WTe_2 has the largest LD response, because it has the smallest band gap and broad deformation at K valley when uniaxial strain is considered. According to these results, unlike having a better piezoelectricty [76] compared to TMDs, JTMDs do not exhibit unique properties. As a matter of fact, JTMDs display the features between their counterpart pristine TMDs. The underlying reason is that janus materials break mirror symmetry [76] and CD is known to arise from in-plane 3-fold rotational symmetry [109].

The strain effects considered in this thesis only include direct band gap (J)TMDs for unstrained and strained cases [121]. Direct band gap materials have stronger optical transitions compared with their indirect equivalents [125]. Though, the valley characteristics can be obtained for indirect band gap materials or strained systems by using $\mathbf{k} \cdot \mathbf{p}$ method. In this situation, instead of only focusing a specific valley such as K, all high symmetry points should be considered in the $\mathbf{k} \cdot \mathbf{p}$ calculations [126]. The cost for this computation increase such as, the number of the bands change from 4-8 to 15 bands for spinless case [127]. Another unavoidable difficulty is the increment in the $\mathbf{k} \cdot \mathbf{p}$ parameters.

The remainder of the thesis is organized as follows. The $\mathbf{k} \cdot \mathbf{p}$ method and dichroism are described thoroughly in Theory part Section 3.1 and the details of DFT calculations are given at Appendix B.1. Subsequently, unstrained and strained electronic band structures are demonstrated for (J)TMDs. Based on

these calculations, strain and spin-orbit results are analyzed in order to get $\mathbf{k} \cdot \mathbf{p}$ parameters. Additionally, CD and LD are calculated under biaxial, uniaxial and shear strain for all (J)TMDs. Finally, all the discoveries are reviewed. Further findings are presented in Appendix B.

Chapter 2

DFT 1/2 Method and Applications

2.1 Theory

2.1.1 Exchange-Correlation Effects

DFT is one of the most reliable technique that allows one to calculate the electronic structure and the properties of atoms, molecules and solids. DFT is proposed in 1964 with a paper written by Hohenberg-Kohn [6]. It suggests how a system with N electrons under an external potential can be analyzed by using functionals depending on the electron charge density.

To describe this system the Hamiltonian can be written as a combination of kinetic energy, external potential and Coulomb interaction:

$$H = T + V + U, \tag{2.1}$$

where

$$T \equiv \frac{1}{2}\int \nabla\psi^*(\mathbf{r})\nabla\psi(\mathbf{r})d\mathbf{r}, \tag{2.2}$$

$$V \equiv \int v(\mathbf{r})\psi^*(\mathbf{r})\psi(\mathbf{r})d\mathbf{r}, \tag{2.3}$$

$$U = \frac{1}{2}\int \frac{1}{|\mathbf{r}-\mathbf{r}'|}\psi^*(\mathbf{r})\psi^*(\mathbf{r}')\psi(\mathbf{r})\psi(\mathbf{r}')d\mathbf{r}d\mathbf{r}'. \tag{2.4}$$

The electron density is $n(\mathbf{r}) = (\Psi, \psi^*(\mathbf{r})\psi(\mathbf{r})\Psi))$ which is denoted as a function of the ground state ψ and depends on the external potential functional $v(\mathbf{r})$. For any external potential, $F[n(\mathbf{r})]$ is defined as a functional of Kinetic and Coulomb interaction energy [6]

$$F[n(\mathbf{r})] \equiv (\Psi, (T+U)\Psi), \tag{2.5}$$

Using these, the energy functional can be written as [6]

$$E_v[n] = \int v(\mathbf{r})n(\mathbf{r})d\mathbf{r} + F[n] \tag{2.6}$$

$$= \int v(\mathbf{r})n(\mathbf{r})d\mathbf{r} + \frac{1}{2}\int \frac{n(\mathbf{r})n(\mathbf{r}')}{|\mathbf{r}-\mathbf{r}'|}d\mathbf{r}d\mathbf{r}' + G[n]. \tag{2.7}$$

For a N particle system $N = \int n(\mathbf{r})d\mathbf{r}$, E_v gives the ground state energy for interacting inhomogeneous gas under external potential. In Equation 2.7, a new functional $G[n]$ is introduced. In 1965, Kohn-Sham [13] assigned exchange and correlation effects to $G[n]$.

$$G[n] \equiv T_s[n] + E_{xc}[n], \tag{2.8}$$

where T_s is the kinetic energy and E_{xc} is the exchange correlation energy, depending on $n(\mathbf{r})$. Exchange-correlation energy is defined as

$$E_{xc}[n] = \int n(\mathbf{r})\epsilon_{xc}(n(\mathbf{r}))d\mathbf{r}. \tag{2.9}$$

Here, ϵ_{xc} is exchange-correlation energy in a uniform gas per electron [13]. Using the stationary property, we get following equation [13]

$$\delta n(\mathbf{r})\left\{\varphi(\mathbf{r}) + \frac{\delta T_s[n]}{\delta n(\mathbf{r})} + \mu_{xc}(n(\mathbf{r}))\right\}d\mathbf{r} = 0, \tag{2.10}$$

where

$$\varphi(\mathbf{r}) = v(\mathbf{r}) + \int \frac{n(\mathbf{r}')}{|\mathbf{r}-\mathbf{r}'|}d\mathbf{r}', \tag{2.11}$$

$$\mu_{xc}(n) = \frac{d(n\epsilon_{xc}(n))}{dn}, \tag{2.12}$$

the chemical potential is defined with $\mu_{xc}(n)$.
By using these parameters, one-electron Schrödinger equation is written

$$\left\{\frac{1}{2}\nabla^2 + [\varphi(\mathbf{r}) + \mu_{xc}\left(n(\mathbf{r})\right)]\right\}\psi_i(\mathbf{r}) = \epsilon_i\psi_i(\mathbf{r}), \tag{2.13}$$

with the definition of the electron density defined for N electrons

$$n(\mathbf{r}) = \sum_{i=1}^{N} |\psi_i(\mathbf{r})|^2. \tag{2.14}$$

Assuming that one knows $n(\mathbf{r})$ in the beginning and places this into $\varphi(\mathbf{r})$ and $\mu_{xc}(n)$, it is possible to solve the one-particle Schrödinger equation and obtain the new electron density. This self-consistent process enables to find the energy as [13]

$$E = \sum_{1}^{N}\epsilon_i - \frac{1}{2}\int\int\frac{n(\mathbf{r}')n(\mathbf{r})}{|\mathbf{r}-\mathbf{r}'|}d\mathbf{r}d\mathbf{r}' + \int n(\mathbf{r})\left[\epsilon_{xc}\left(n(\mathbf{r})\right) - \mu_{xc}\left(n(\mathbf{r})\right)\right]d\mathbf{r}. \tag{2.15}$$

This formulation given shows how the exchange and correlation effects helps to find the energy self consistently for local density approximation (LDA).
Later, based on Kohn-Sham's method, this approximation is moved a step further by a new one called generalized gradient approximation (GGA) proposed by Perdew-Burke-Ernzerhof [7] which is improved from PW91 by Perdew-Wang [128]. A common point between LDA and GGA is to define the energy as a combination of exchange and correlation [7]

$$E_{xc} = E_x + E_c, \tag{2.16}$$

$$E_{xc}^{GGA}\left[n_\uparrow, n_\downarrow\right] = \int d\mathbf{r}n\epsilon_x^{unif}F_{xc}(r_s,\zeta,s), \tag{2.17}$$

where $n = n_\uparrow + n_\downarrow$ and F_{xc} is an analytical function. LDA gives [13]

$$E_{xc}[n] = E_x[n] + \int n(\mathbf{r})\epsilon_c\left(n(\mathbf{r})\right)d\mathbf{r}, \tag{2.18}$$

where E_x is defined as exchange energy of a Hartree-Fock system and ϵ_c is the correlation energy of the homogeneous electron gas. This equation for GGA is denoted as [7]

$$E_c^{GGA}\left[n_\uparrow, n_\downarrow\right] = \int d\mathbf{r}n[\epsilon_c^{unif}(r_s,\zeta) + H(r_s,\zeta,t)]. \tag{2.19}$$

Here, r_s is Seitz radius $n = 3/4\pi r_s^3$, $\zeta = (n_\uparrow - n_\downarrow)/n$ is relative spin polarization and $t = |\nabla n|/2\phi k_s n$ is the dimensionless density gradient. The difference between Equation 2.18 and 2.19 is a correction done by H function. For a slowly varying t, H is a constant found by numerical calculations of GGA, and when t is varying rapidly, the correlation vanishes.

In LDA, for a slowly-varying system where the main charge distribution lie, the exchange potential is found as [13]

$$v_x(\mathbf{r}) = -\left(\frac{3}{2\pi}\right) k_F(\mathbf{r}), \tag{2.20}$$

where $k_F(\mathbf{r}) \equiv \{3\pi^2 n(\mathbf{r})\}^{\frac{1}{3}}$. This equation is improved in GGA method as

$$E_x^{GGA} = \int d^3r n \epsilon_x^{unif}(n) F_x(s). \tag{2.21}$$

Here, the potential is found to be $-3e^2 k_F/4\pi$. Function $F_x(s) = 1 + \kappa - \kappa/(1 + \mu s^2/\kappa)$ has the parameters $\mu = 0.219$ and $\kappa = 0.804$ ($\mu = 0.235$, $\kappa = 0.967$). When the atomization energies of some molecules are compared, GGA obtains very close values to experimental ones compared to LDA.

2.1.2 Basics of the DFT-1/2 Variant

From the previous section, with the details of exchange-correlation functionals, we have learned that using DFT, the electronic structure of a material can be calculated self-consistently with the knowledge of the charge density and external potential. LDA and GGA functionals are very good approximations to calculate these properties yet they underestimate the band gap compared to the experimental values. Hybrid (HSE) calculations over the DFT ones or switching to quasi-particle calculations (GW) with the starting point LDA/GGA gives better results. However, these methods increase the computational budget.

Ferreira et. al proposed a new method called LDA-1/2 [12] and later extended to GGA-1/2 [16] that allows to find the band gaps close to experimental ones without any additional computational cost to regular LDA/GGA calculations. This theory starts with introducing us the Slater-Johnson $X\alpha$ method [14]. This method allows us to calculate eigenvalues $\epsilon_{iX\alpha}$ of an occupied/unoccupied spin

orbital ($n_i = 1$ or $n_i = 0$) by taking the derivation of total energy $\langle E_{iX\alpha} \rangle$ with respect to the occupation number. Also, with using this method, the transition state is found to be the half of the occupation number of the spin orbitals and the excitation energy is found by taking the difference between initial and final ϵ_i.

Later, Janak [15] has proven that $X\alpha$ method can be used in DFT method that has been discussed in previous section. Based on Slater-Johnson and Janak's formulation, Ferreira et. al expressed the eigenvalues as [12, 16]

$$\frac{\partial E}{\partial f_\alpha} = e_\alpha(f_\alpha), \tag{2.22}$$

where, E is the total energy and f_α is the occupation of Kohn-Sham state. If we want to find the transition state energy, we take the difference of the ground state ($f_\alpha = 0$) energy and the ion energy ($f_\alpha = -1$). With the half-ion technique it is found as

$$E_\alpha(0) - E_\alpha(-1) = \int_{-1}^{0} \frac{\partial E}{\partial f_\alpha} df_\alpha, \tag{2.23}$$

$$= e_\alpha(-1/2), \tag{2.24}$$

as suggested in $X\alpha$ method. Second derivative will give the self-energy

$$\frac{\partial e_\alpha}{\partial f_\alpha} = 2S_\alpha, \tag{2.25}$$

resulting $e_\alpha(0) - S_\alpha = e_\alpha(-1/2)$ and $E(0) - E(-1) = e_\alpha(0) - S_\alpha = e_\alpha(-1/2)$ [12, 16]. Here, self-energy S_α and self-energy potential V_s parameters are important.

$$S_\alpha = \int d^3 r n_\alpha(\mathbf{r}) V_s(\mathbf{r}), \tag{2.26}$$

where $n = \psi_\alpha^* \psi_\alpha$, resembling the exchange-correlation functional definitions. The self-energy and the self-energy potential can be written as [12, 16]

$$\begin{aligned} S_\alpha = & \int\int d\mathbf{r} d\mathbf{r}' \frac{n_\alpha(\mathbf{r}) n_\alpha(\mathbf{r}')}{|\mathbf{r} - \mathbf{r}'|} + \frac{1}{2} \int\int d\mathbf{r} d\mathbf{r}' n_\alpha(\mathbf{r}) \frac{\delta^2 E_{xc}}{\delta n(\mathbf{r}) \delta n(\mathbf{r}')} n_\alpha(\mathbf{r}') \\ & + \int\int d\mathbf{r} d\mathbf{r}' \frac{n_\alpha}{|\mathbf{r} - \mathbf{r}'|} \sum_\beta f_\beta \frac{\partial n_\beta(\mathbf{r}')}{\partial f_\alpha} \\ & + \frac{1}{2} \int\int d\mathbf{r} d\mathbf{r}' n_\alpha \frac{\delta^2 E_{xc}}{\delta n(\mathbf{r}) \delta n(\mathbf{r}')} \sum_\beta f_\beta \frac{\partial n_\beta(\mathbf{r}')}{\partial f_\alpha}, \end{aligned} \tag{2.27}$$

$$V_s(\mathbf{r}) = \int d\mathbf{r}' \frac{n_\alpha(\mathbf{r}')}{|\mathbf{r}-\mathbf{r}'|} + \frac{1}{2}\int d\mathbf{r}' \frac{\delta^2 E_{xc}}{\delta n(\mathbf{r})\delta n(\mathbf{r}')} n_\alpha(\mathbf{r}') + \int d\mathbf{r}' \frac{\sum_\beta f_\beta \frac{\partial n_\beta(\mathbf{r}')}{\partial f_\alpha}}{|\mathbf{r}-\mathbf{r}'|} + \frac{1}{2}\int d\mathbf{r}' \frac{\delta^2 E_{xc}}{\delta n(\mathbf{r})\delta n(\mathbf{r}')} \sum_\beta f_\beta \frac{\partial n_\beta(\mathbf{r}')}{\partial f_\alpha}. \tag{2.28}$$

Self-energy (and, so does the self-energy potential) changes according to how much the function is localized. If it is spread the self energy potential becomes very small, if it is localized self energy is maximized. For half-ion the self-energy potential is found to be $V_s(r) = V_s(0,r) - V_s(-1/2,r)$ [12, 16]. When the self-energy is added to all the atoms in the whole crystal, V_s diverges. Ferreira et. al [12, 16] applied a trim function to V_s so that this potential does not overlap the neighbouring atoms

$$\Theta(\mathbf{r}) = \begin{cases} \left[1 - (\frac{r}{CUT})^n\right]^3, & r \leq CUT \\ 0, & r > CUT \end{cases} \tag{2.29}$$

and $V_s' = \Theta(r)V_s(r)$. It is suggested to use $n = 8$, which gives good results.

Improvement over DFT-1/2 has continued in recent years. One example is shell-LDA-1/2 method by Xue et. al [28]. By following the steps of original DFT-1/2 method, in shell-LDA-1/2, the trim function in Equation 2.29 is slightly modified with two radius r_{in} and r_{out} to compare with CUT parameter. r_{in} and r_{out} are determined by calculating where the band gap starts to increase to the point correction diverges. As a result, they prevented the problem of the interaction with external self-energy potential or the self-energy potential correction accuracy where the hole is very close to the atom. With this correction, for covalent semiconductors, the band gap values become closer to experimental ones [28].

As we have mentioned in the introduction, a recent paper by Guilhon et. al [22] adapted DFT-1/2 for 2D materials and managed to obtain the same performance with previous results for 3D materials [12, 16]. In that work, they have improved the technique by going through the orbital distribution of valence band maximum (VBM) and conduction band minimum (VBM) to decide whether stripping half an electron only from VB or both VB and CB is necessary. According to their findings, while for some materials, applying DFT-1/2 technique only to VB, gives the same results with VB+CB correction and for the others, both corrections are required to accomplish a gap value at GW approximation level.

2.2 Our DFT-1/2 Results

Inspired by the previous DFT-1/2 studies, we have applied this method to 2D hexagonal Group III-N compounds. For these calculations, we adhere to the original DFT-1/2 method by subtracting half electron from VB for the anion N as recommended in this paper [12] . According to our results presented in Table 2.1, only BN has a direct band gap. While for indirect gap materials LDA-1/2 gives larger gap values, PBE-1/2 performs better with direct gap BN.

	PBE	**PBE-1/2**	**LDA**	**LDA-1/2**
AlN	3.26(ΓM)	5.16	3.39	5.27
	2.94 (ΓK)	4.93	3.07	5.05
BN	4.65 (KK)	6.64	4.59	6.59
GaN	1.96 (ΓK)	3.45	2.39	3.97
InN	0.41 (ΓK)	1.84	0.65	2.09
	0.63 ($\Gamma\Gamma$)	2.12	0.76	2.27

Table 2.1: Band gaps calculated for AlN, BN, GaN and InN using DFT and DFT-1/2.

When we compare our results with previous studies presented in Table 2.2, HSE values are either smaller or very close to our PBE-1/2 values. However, except for BN, DFT-1/2 still underestimates the band gap compared with *GW* results. Our PBE-1/2 values compared with the previous ones presented in Table 2.2 match with slight differences.

	HSE	**GW**	**PBE-1/2 (VB/VB+CB)**
AlN	4.04 (ΓK) [129]	5.57 (ΓM) [130]	4.87/4.87 [22]
BN	5.68 (KK) [129]	6.86 (ΓK)[130]	6.62/6.85 [22]
GaN	3.23 (ΓK) [129]	5.00 (ΓK) [130], 4.1 [131]	3.64/3.81 [22]
InN	1.35 (ΓK) [129]	5.76 ($\Gamma\Gamma$) [130], 1.7 [131]	1.90/1.98 [22]

Table 2.2: Band gaps from previous studies for AlN, BN, GaN and InN using HSE, *GW* and PBE-1/2.

From these hexagonal N compounds, we select the direct gap BN to examine the properties using DFT and DFT-1/2. First, *CUT* value should be decided for

maximized band gap value. We calculated the band gaps for $CUT = 1.0 - 4.0\ a_0$ and plotted in Figure 2.1. According to these results, we decided to use $CUT = 2.5\ a_0$ and plotted DFT and DFT-1/2 band structures in Figure 2.2 with this value.

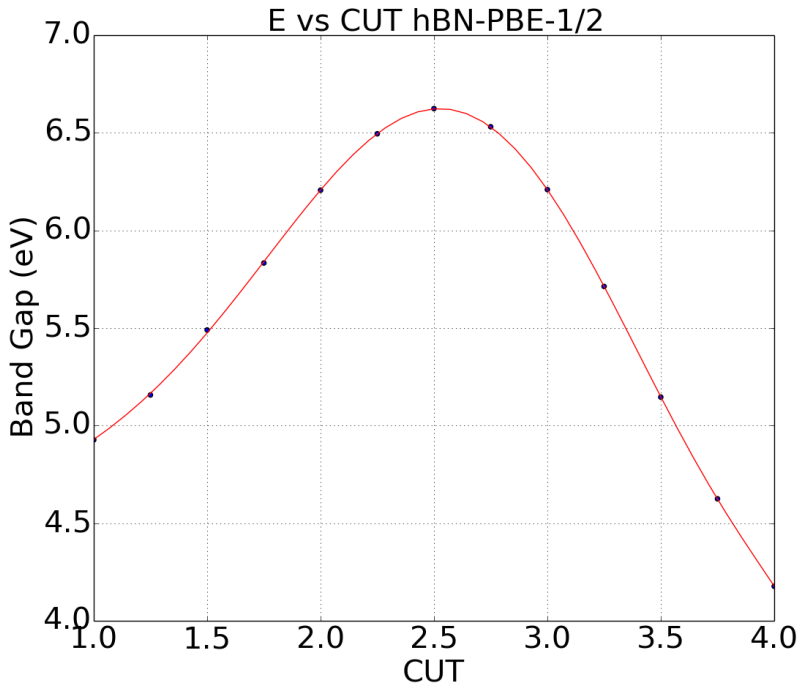


Figure 2.1: Band gap vs. CUT graph for BN.

Generally, defected structures have some flat bands between the VB and CB, but if the band gap is small, it is difficult to identify such states. From the pristine h-BN in Figure 2.2, it is seen that both LDA-1/2 and PBE-1/2 expands the band gap good enough so that one can explore the electronic properties of defected h-BN crystal.

2.3 h-BN defects: DFT vs DFT-1/2

We begin by calculating the band structure of pristine h-BN to check the differences with the defected system by using identical supercell size for both.

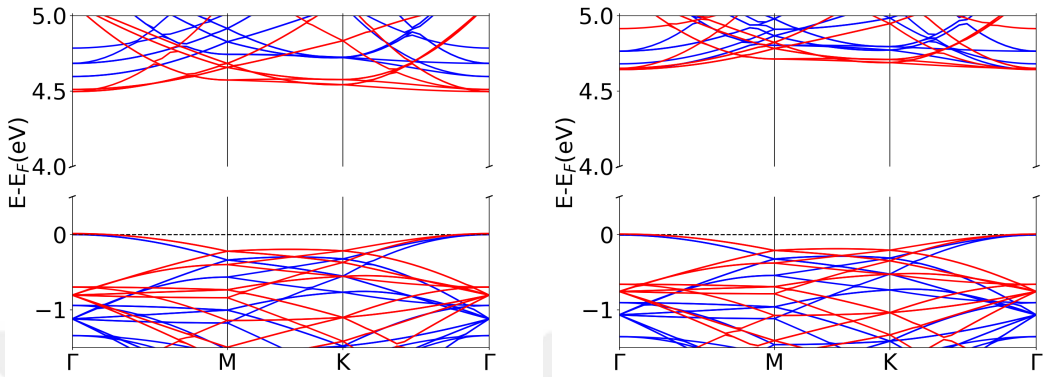


Figure 2.2: Band structure for monolayer h-BN pristine calculated with (a) LDA (blue) and LDA-1/2 (red) (b) PBE (blue) and PBE-1/2 (red).

In accordance with the results, direct band gap value from VB to CB at ΓΓ is found almost indistinguishable for LDA/PBE as 4.63/4.64 eV. Additionally, the transition energy from Γ to K is 4.82/4.94 eV. When DFT-1/2 technique is applied, the band gap (at ΓΓ) and the transition energy (at ΓK) are found as 6.64/6.59 eV and 6.83/6.81 eV for (PBE-1/2)/(LDA-1/2), respectively. The experimental band gap is reported as 6 eV [27], which is 25% larger than DFT values and 10% smaller than DFT-1/2 ones. From Figure 2.2, it is observed that DFT-1/2 method maintains the band dispersion while increasing the band gap effectively. This behaviour is in agreement with many 2D materials analyzed previously with the same method [22]. The defect types which are going to be analyzed are shown in Figure 2.3.

2.3.1 Carbon Impurities

Carbon impurities are formed by substituting a carbon (C) atom with boron (B) or nitrogen (N) atom (C_B or C_N). This type of defected crystals have their space and point group symmetries as *P-6m2* and D_{3h}. The energy levels for these impurities are obtained and presented in Figure 2.4 and 2.5. Fermi level is chosen for all defect energies as the highest occupied molecular orbital (HOMO) at zero temperature and displayed with dashed line. Arrows indicate the occupied defect

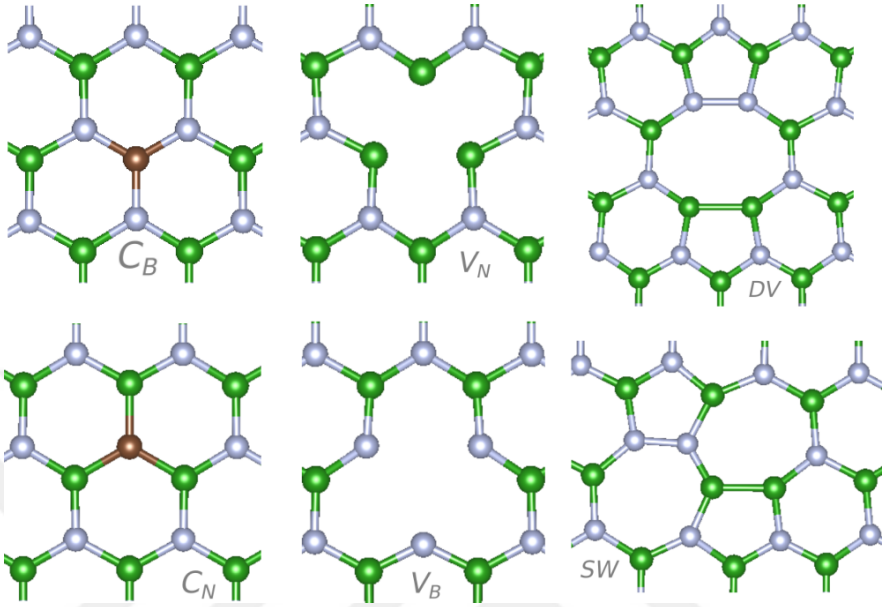


Figure 2.3: Schematic representation of carbon impurities (C_B, C_N), single vacancies (V_B, V_N), double vacancy (DV) and Stone-Wales (SW) defect. B, N and C atoms are colored in green, grey and brown.

states with negative or zero energies and vice versa for unoccupied ones.

According to the calculations, spin down states appear to be unoccupied and the exact opposite for spin up states for both C_B and C_N in Figure 2.4 and 2.5. As demonstrated in previous calculations [132, 43], while C_B Fermi level is closer to CB, for C_N it is shifted to VB. While B or N atom is replaced by a C atom, because of the differences of group III and V, an electron is added or removed to/from the system. This can be the underlying cause of Fermi level shift.

In comparison with DFT, undoubtedly PBE-1/2 and LDA-1/2 enhances the band gap for both impurities. As shown in third and sixth panels in Figure 2.5, when DFT-1/2 improvement is performed not only for N but also C atom, the defect levels are moved a little bit in accordance with the increased band gap. The acquired results show that each approach exhibits different energy levels for mentioned defects. Besides, as presented in Appendix A.2, for 10×10×1 and 6×6×1 supercells this situation becomes more complex. Checking with many

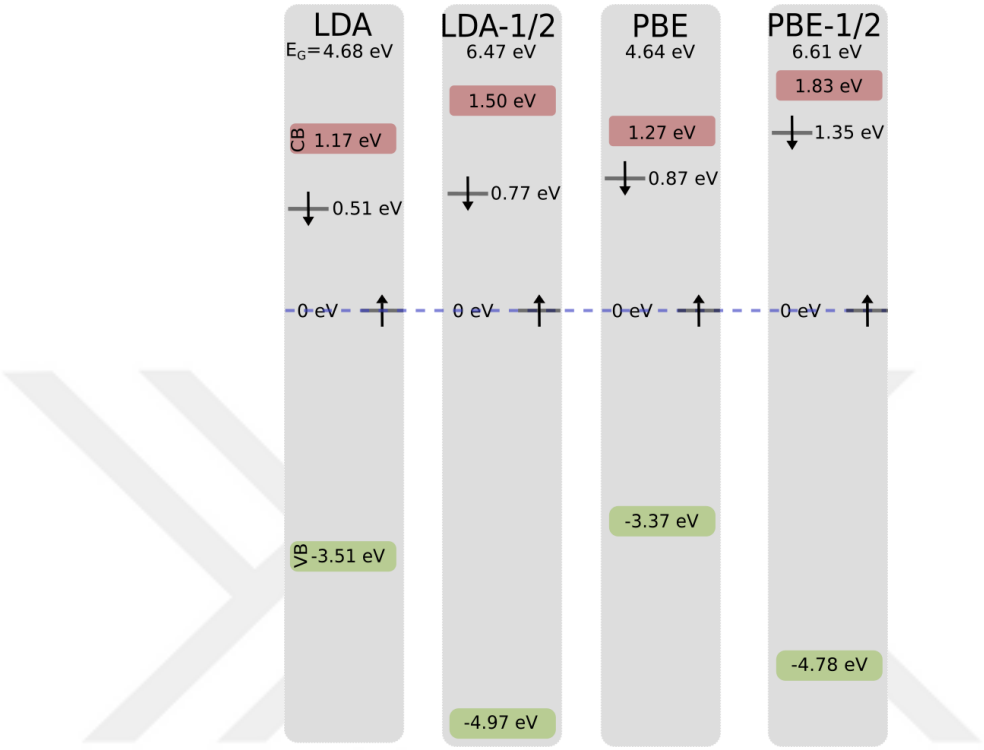


Figure 2.4: C_B defect energy levels placed in the band gap (not to scale) calculated with LDA, LDA-1/2, PBE and PBE-1/2.

previous results for C_B and C_N displayed supercell size and pseudopotential dependence may change the energy levels. Yet, band gaps and band structures are similar with the ones we have obtained [37, 132, 43].

2.3.2 Vacancies

We have created two single vacancies by taking out a boron or nitrogen atom (V_B or V_N) and a divacancy (DV) by extracting both atoms. Subsequently, the space and point group symmetries become *Amm2* ($C_{2\nu}$) and *6/Pm* (C_s), respectively.

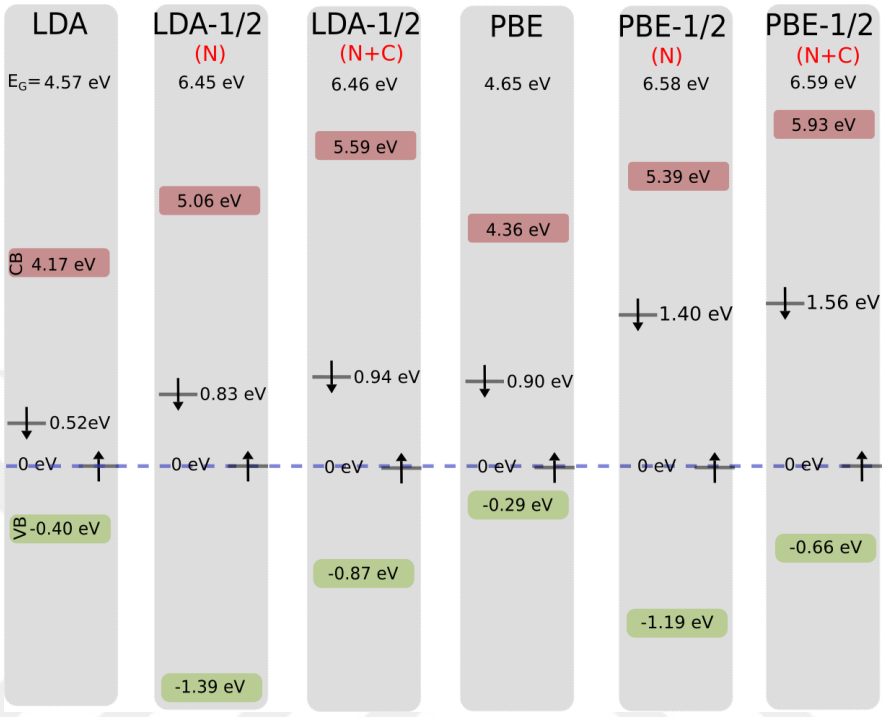


Figure 2.5: C_N defect energy levels placed in the band gap (not to scale) calculated with LDA, LDA-1/2 with N only, LDA-1/2 with N and C, PBE, PBE-1/2 with N only, and PBE-1/2 with N and C.

2.3.2.1 Single Vacancy

Calculations with different functionals showed distinct spin down and up layouts. This is caused by the buried defect states of V_N inside of CB, shown as in Figure 2.6. Further, total number of defect states has changed. Comparison with previous publications [132, 32] two unoccupied states are observed with few meV difference for PBE.

Our 10×10×1 supercell data provided in Appendix A.2 for LDA calculations give similar results with PBE, while 6×6×1 supercell ones are unable to identify all unoccupied states [37]. Previously, it was suggested that considering sample largeness as a parameter, one can create a surface defect to re-position the band gap in silicon [133].

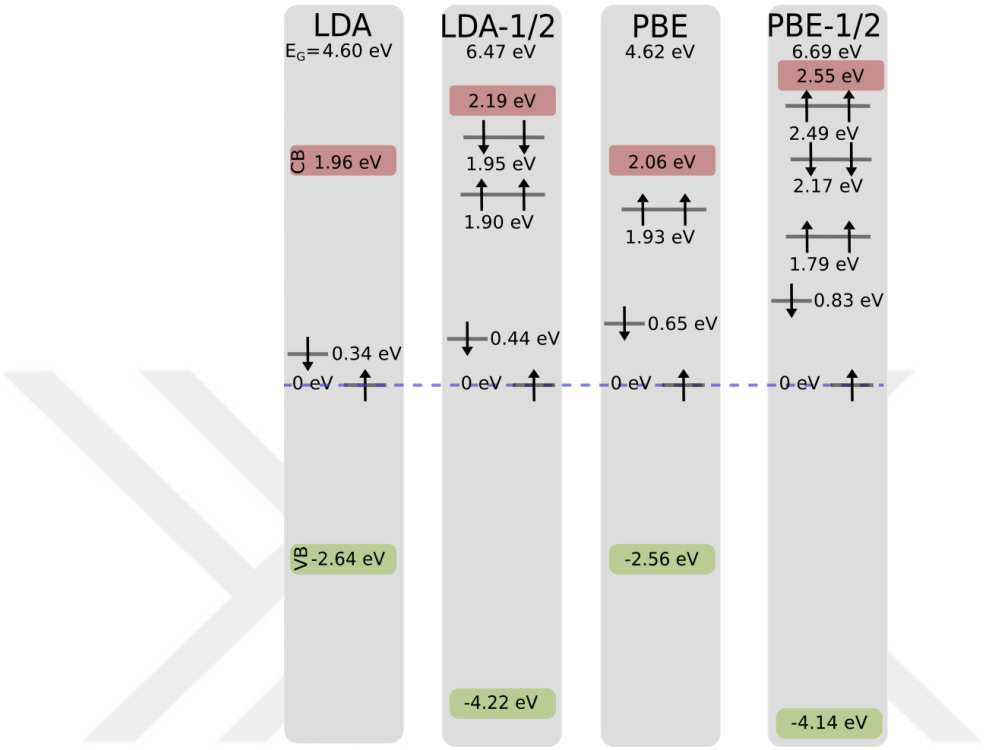


Figure 2.6: V_N defect energy levels placed in the band gap (not to scale) calculated with LDA, LDA-1/2, PBE and PBE-1/2.

As mentioned earlier, LDA and LDA-1/2 calculations showed some difference in CB. In Figure 2.7, detailed band structure graph for CB shows the defect states with red lines. They are supported with localized charge density inset graphs displaying almost identical behaviour. For LDA-1/2, the double degenerate spin up defect states appear in the band gap region and display flat behaviour like expected as a defect essentiality. However, these states are broader and hidden in CB for LDA calculations. Due to the greater increase in the band gap, PBE-1/2 method exposes additional states from CB. According to these results, LDA-1/2 is useful to discover the defect layout of V_N.

For V_B shown in Figure 2.8, we observe two double degenerate spin up and down states occupied/unoccupied where they are close to CB or VB, with LDA. As the band gap becomes larger with LDA-1/2 method, these states are shifted

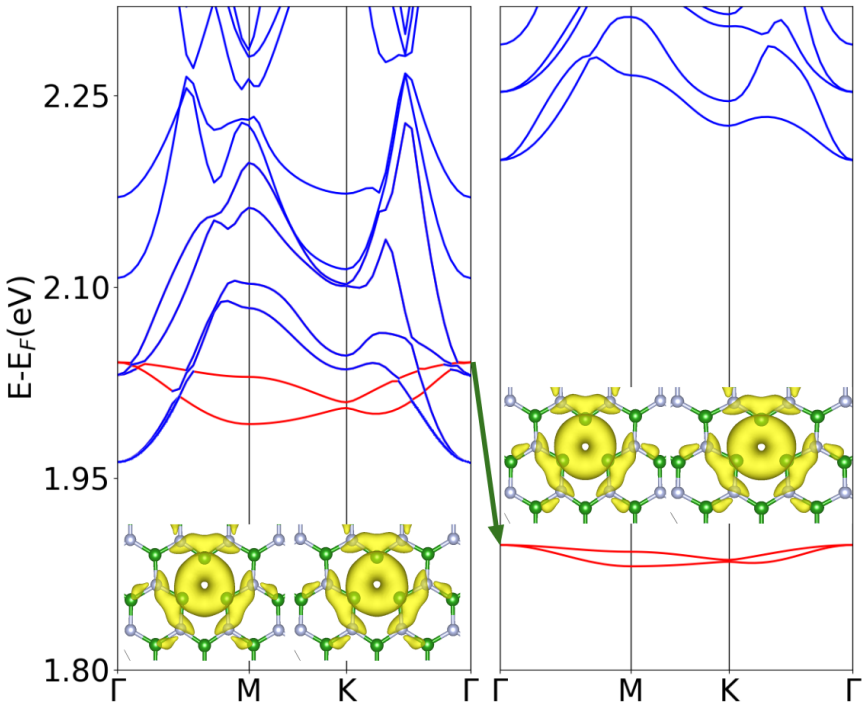


Figure 2.7: Electronic band structures and charge densities near CB (blue) with spin up V_N state (red) with LDA (left) and LDA-1/2 (right). B and N atoms are colored in green and grey.

while their double degenerate nature is maintained. However, this picture changes when PBE-1/2 method is used. In PBE, we see the same arrangement of spin up and down states with slight differences of energies with LDA. But for PBE-1/2 results, double degenerate spin down states disappear in VB.

As shown in Figure 2.9, for PBE, there are two spin down states very close to VB. With PBE-1/2, these states become buried inside of VB unexpectedly, proved by the localized charge density inset graphs that they are preserved as defect states. Checking with previous studies shows different number of states, making an impact that V_B is a very puzzling and complex type of defect [132, 37].

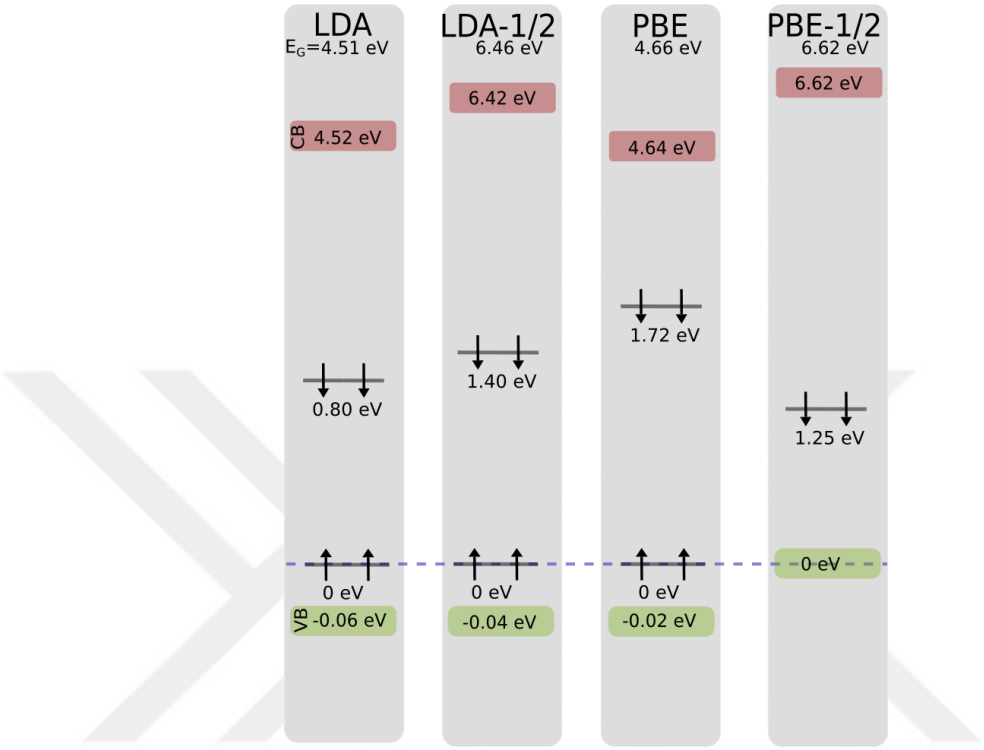


Figure 2.8: V_B defect energy levels placed in the band gap (not to scale) calculated with LDA, LDA-1/2, PBE and PBE-1/2. Here, the Fermi level is set to spin up HOMO.

2.3.2.2 Double Vacancy

An additional vacancy we have studied is divacancy (DV) which emerges from boron and nitrogen vacancies nearby. As discussed in the beginning of this section, the space and point group symmetries are different from single vacancies. Additionally, number of defect states also differ.

In the first place, double degenerate singlet states are known to be different from single vacancies [37]. Arising from B-B and N-N bonds, with regular DFT calculations three defect states appear while four are expected in the band gap [37]. This behaviour is validated with one occupied and two unoccupied spin degenerate states occurring according to our DFT calculations presented

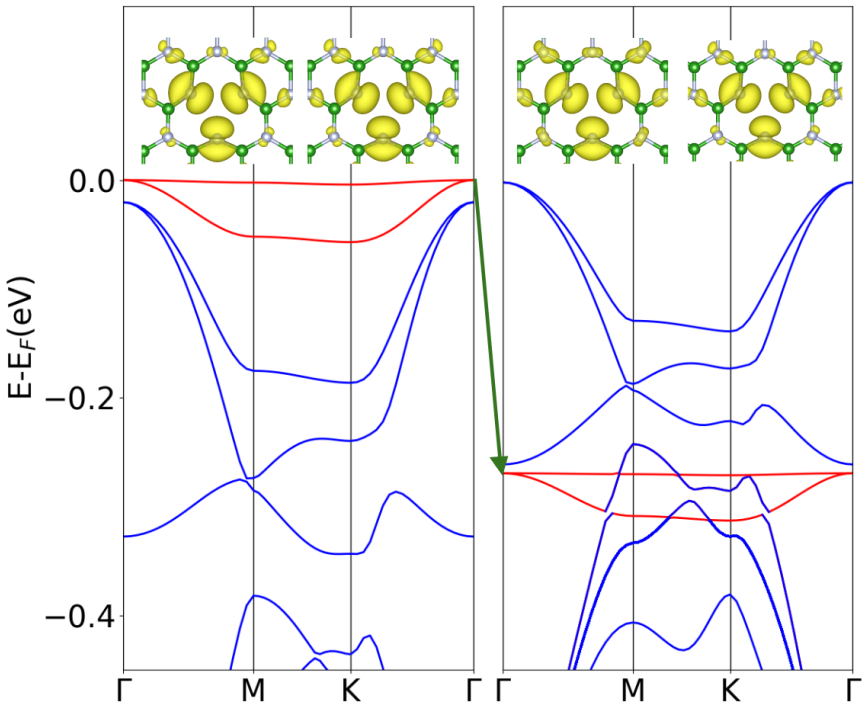


Figure 2.9: Electronic band structures and charge densities near VB (blue) with spin up V_B state (red) with PBE (left) and PBE-1/2 (right). B and N atoms are colored in green and grey.

in Figure 2.10. The fourth expected occupied state is exposed due to DFT-1/2 methods. Examining the defect states shows us while half of the states are close to CB and the other half to VB. This outcome is reasonable since divacancy is the combination of two single vacancies V_B and V_N.

2.3.3 Stone-Wales Defect

Last defect we are going to discuss is Stone-Wales (SW). Around the center, the B-N bond is rotated with 90° angle, so that the defect is created. By this procedure, this defect is distinct from previous ones since any atom is not removed

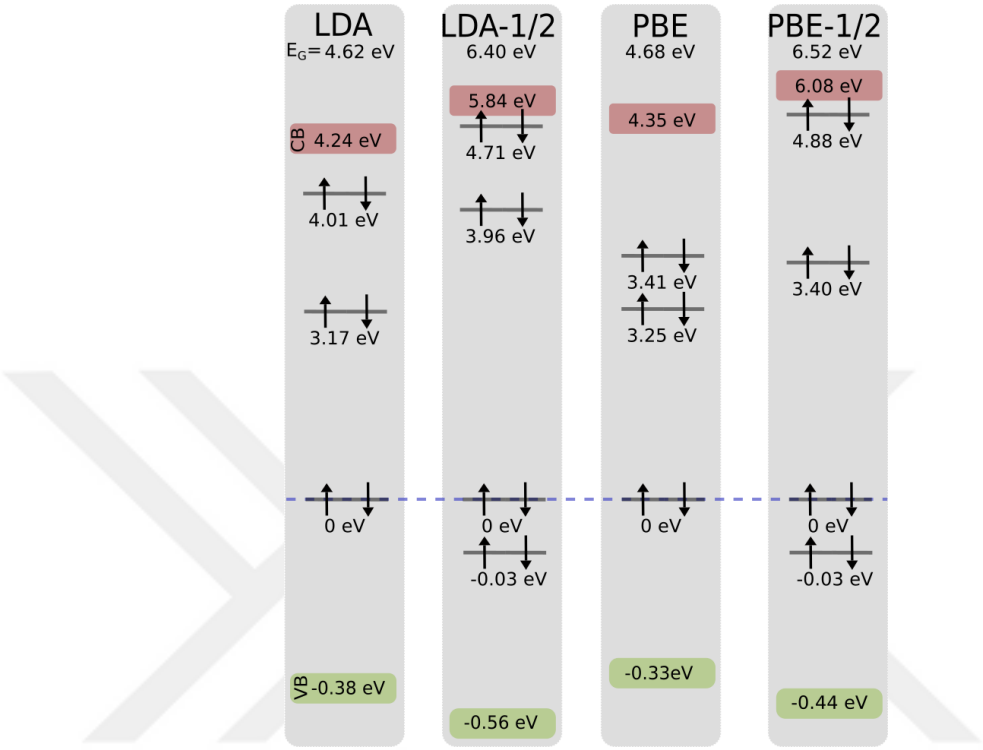


Figure 2.10: DV defect energy levels placed in the band gap (not to scale) calculated with LDA, LDA-1/2, PBE and PBE-1/2.

from the system or changed by another. Consequently, the space and point group symmetries change into $6/Pm$ and C_S (it was D_{3h} for pristine). Recalling DV symmetries, SW and DV defects show some resemblance. So that, their spectra might be alike. The pristine structure has bond energies larger than DV and SW defect bond energies since the symmetry is broken for B-B and N-N bonds.

We look for spin degenerate singlet states [43] in accordance with these parallelism of SW and DV defects. Our predictions are confirmed as shown in Figure 2.11. As reported in Figure 2.12, we have found two singlet states (one occupied and one unoccupied) as this number changes to three states when DFT-1/2 calculations are considered. One occupied double degenerate singlet state becomes observable above VB as the band gap increases. Figure 2.12 inset graphs of the charge density calculations show the flat defect band (which is indicated with red). Compared with LDA calculations, it can be commented as LDA-1/2 is successful of extracting the buried defect state from VB as it maintains the

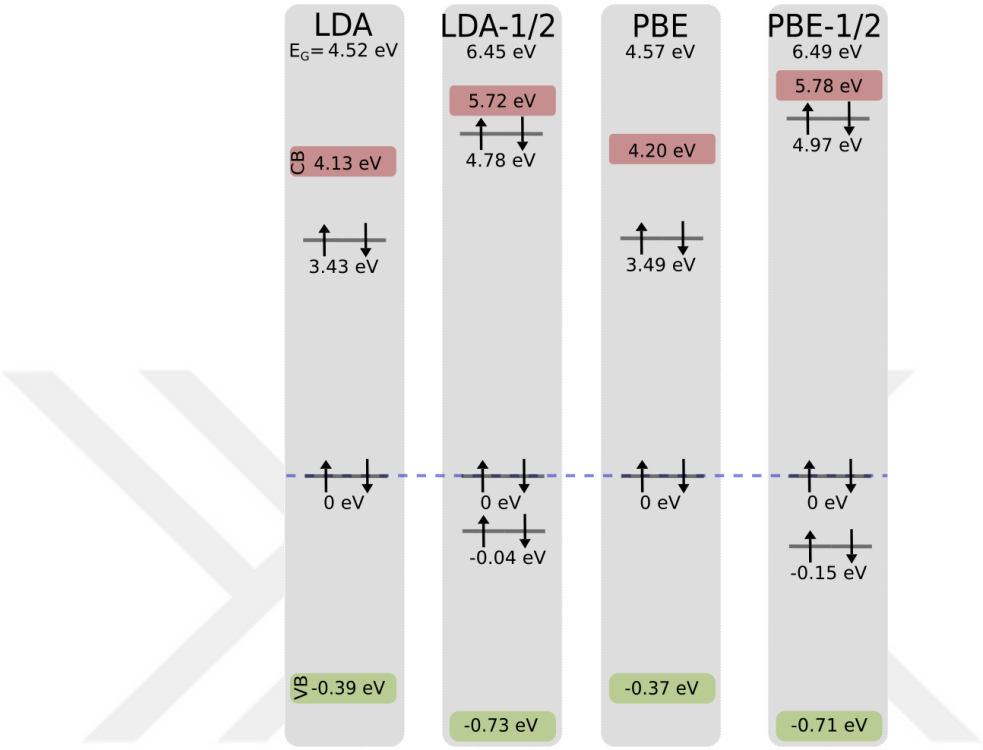


Figure 2.11: SW defect energy levels placed in the band gap (not to scale) calculated with LDA, LDA-1/2, PBE and PBE-1/2.

charge density localization. One earlier study [43] is available for SW calculations to make a comparison, which is consistent with our results.

2.4 Computational Budget Comparison With Higher Order Methods

In this part of the thesis, we wanted to address the differences of DFT and DFT-1/2 methods. At this point, for h-BN, we referred to post-DFT method results in order to crosscheck the validity of DFT-1/2. Results calculated with two higher order techniques are compiled in Table 2.3: hybrid functional (HSE06) and many body quasiparticle approach (GW) [25]. For LDA-1/2 and GW results, analogous spin structure is obtained, but some extra defect states appeared in

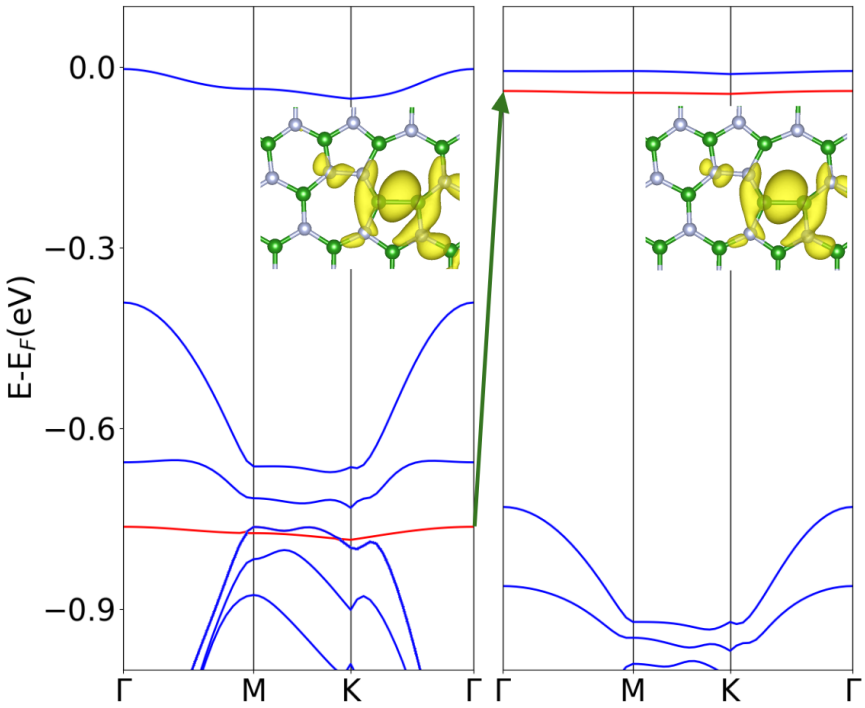


Figure 2.12: Band structure around VB (blue) including SW defect for spin up state (red) with LDA (left) and LDA-1/2 (right) and their charge densities. B and N atoms are colored in green and grey.

each group. Here, in some cases, a discrepancy in energy levels around 1 eV or more is spotted. Besides, comparison of single shot G_0W_0 and GW studies [37, 38] shows difference in defect energies by 0.9 eV, which can be checked from Table 2.3.

As documented in Appendix A.4, systematic HSE calculations over LDA-1/2 demonstrate reasonably close results to GW for both defect types. Particularly, the greater band gap with LDA-1/2 method enables to acquire higher defect energy levels placed according to VBM, when compared with HSE. A former study [22] revealed that, estimated band gap values using DFT-1/2 method closely fit with GW rather than HSE.

In Table 2.3, spin-polarized hybrid results are added, which are obtained from a previous work [132]. However, expense of the calculations restricted us to get the same set of results. Considering all of the results, HSE calculations are unable to identify a few defect states that are disappeared in CB, so it can be said that

Table 2.3: 2D h-BN spin polarized defect energies. VBM is chosen as the reference point of the defect energy measurements. For HSE calculations, * is used for states lost in CB.

	G_0W_0 **(eV)**	**HSE06 [132] (eV)**	**LDA-1/2 (eV)**
$\mathbf{C}_B$	3.97 ↑, 7.47 ↓ [38]	3.74 ↑, * ↓	4.97 ↑, 5.74 ↓
$\mathbf{C}_N$	0.08 ↑, 3.20 ↓ [37]	0.41 ↑, 2.51 ↓	1.39 ↑, 2.22 ↓
$\mathbf{V}_B$	0.15 ↑↓, 0.15 ↑, 2.84 ↓, 3.43 ↑, 4.64 ↓ [37]	2.5 ↑, 2.1 ↓, 3.2↓	0.04 ↑↑, 1.44 ↓↓
$\mathbf{V}_N$	3.09 ↑, 6.36 ↓ [38], 2.93 ↑, 5.42 ↓, 6.63 ↑↑ [37]	3.29 ↑, 4.68 ↓, * ↑↑	4.22 ↑, 4.66 ↓, 6.12 ↑↑, 6.41 ↓↓
DV	0.18 ↑↓, 5.70 ↑↓, 5.78 ↑↓ [37]	-	0.53 ↑↓, 0.56 ↑↓, 4.49 ↑↓, 5.24 ↑↓
SW	-	-	0.69 ↑↓, 0.73 ↑↓, 5.47 ↑↓

our LDA-1/2 results exhibit closer resemblance with GW set rather than HSE.

Lastly, we want to discuss the computational cost of DFT-1/2 calculations of systems with defects. As a beginning, DFT-1/2 method does not need any additional computational time and memory, compared to DFT except one time generation of self-energy corrected atomic pseudopotential. The need for number of cores and computational time will now be set side by side for DFT and DFT-1/2. If the system is rather simple (like C_B or C_N) or spinless calculations are considered, they increase by 4-6 times, which is acceptable. However, as the defect systems become more complicated (like SW or DV), computational demand for hybrid calculations increase over 30 times, which makes DFT-1/2 a more preferable choice. Additionally, memory insufficiency for such calculations should be considered where DFT-1/2 does not use more memory than DFT.

To sum up, it can be concluded that computational overhead of HSE for small systems or spinless calculations, can be disregarded. Yet, DFT-1/2 is a good alternative for computationally expensive spinful calculations and relatively large systems, as it is precise and computationally affordable. Requirement for computational time and memory for studying 3D or pristine systems is extravagant. It is 1000 times larger for GW when compared to LDA-1/2 [18]. Besides, strong

anisotropic dielectric screening becomes problematic for 2D materials while quasi-particle approximation is used [25]. When these two points are taken into account, using another method/approximation becomes necessary for 2D systems with defects [38].

Chapter 3

Pristine and Janus Transition Metal Dichalcogenides with $\mathbf{k} \cdot \mathbf{p}$ Method

3.1 Theory

The $\mathbf{k} \cdot \mathbf{p}$ method is an empirical band structure method which can be used to calculate the characteristics at the band edge by using the discrete set of Bloch States [118]. With including spin-orbit coupling or strain perturbations, essentially, a low energy Hamiltonian is formed which brings its simplicity. In spin-space, the wavevector independence is assumed for incorporating SOC [119, 120]. $\mathcal{H}^s$ notation is used for two-band decoupled $\mathbf{k} \cdot \mathbf{p}$ Hamiltonians where s is the spin label. For spinless calculations, this superscript is excluded. Our calculations are done for $+K$ valley. For $-K$ valley, a flip in the spin labels and orbital part conjugation is needed.

We set up the $\mathbf{k}\cdot\mathbf{p}$ Hamiltonian by first considering the electron-hole symmetric part. For $+K$ valley where k_x, k_y are chosen as the axes, symmetric part of the

Hamiltonian becomes

$$\mathcal{H}^s_{\text{symm}} = \frac{f^s_1}{2}\sigma_z + f^s_2 a(k_x\sigma_x + k_y\sigma_y)\,, \tag{3.1}$$

Here, σ_i's are Pauli spin matrix elements in Cartesian coordinates, a is the lattice constant. Two $\mathbf{k}\cdot\mathbf{p}$ parameters f^s_1 and f^s_2 represent the energy gap and Dirac velocity, respectively [123]. As a result of this part, conduction and valence bands are placed correctly by the band gap and the dispersion of the bands at the given valley is inherently symmetric. $(1\ \ 0)^T$ and $(0\ \ 1)^T$ base vectors are chosen for the conduction and valence bands [123]. Later on, other Hamiltonian terms are added in order to correctly describe the CB and VB of TMDs [119, 120]. These are, the asymmetry term that is needed for symmetry-breaking between the two bands

$$\mathcal{H}^s_{\text{asym}} = k^2 \begin{pmatrix} \beta^s & 0 \\ 0 & \alpha^s \end{pmatrix}, \tag{3.2}$$

triagonal warping term that helps to avoid isotropic energy dispersion for these 2D materials

$$\mathcal{H}^s_{\text{TW}} = \kappa^s \begin{pmatrix} 0 & k_+^2 \\ k_-^2 & 0 \end{pmatrix}, \tag{3.3}$$

and lastly, the cubic term that is a useful ingredient to achieve the DFT dispersion for the regions away from the K point

$$\mathcal{H}^s_{\text{cub}} = \frac{\eta^s}{2}k^2 \begin{pmatrix} 0 & k_- \\ k_+ & 0 \end{pmatrix}, \tag{3.4}$$

with $k_\pm \equiv k_x \pm ik_y$.

Another term for strain is added further as a linear mechanical perturbation [123]

$$\mathcal{H}_\varepsilon = f_4(\varepsilon_{xx} + \varepsilon_{yy})\sigma_z + f_5\left[(\varepsilon_{xx} - \varepsilon_{yy})\sigma_x - 2\varepsilon_{xy}\sigma_y\right]. \tag{3.5}$$

Spinless calculations are used for f_4 and f_5 deformation potentials. All together, the $\mathbf{k}\cdot\mathbf{p}$ Hamiltonian is written as

$$\mathcal{H}^s = \mathcal{H}^s_{\text{symm}} + \mathcal{H}^s_{\text{asym}} + \mathcal{H}^s_{\text{TW}} + \mathcal{H}^s_{\text{cub}} + \mathcal{H}_\varepsilon. \tag{3.6}$$

Due to the distinct role played by each term in the Hamiltonian, the order of parameter fittings is crucial. Step by step, this fitting procedure is going to be explained.

3.1.1 Parameter Fitting Expressions

To begin with, the symmetric part of the Hamiltonian needs to be formed. Using the DFT results that are computed previously, f_1^s, f_2^s, α^s, and β^s parameters can be obtained by the analytical equations

$$f_1^s = E_{\mathrm{CB}}^s - E_{\mathrm{VB}}^s, \tag{3.7}$$

$$f_2^s = \frac{\hbar}{a}\sqrt{\frac{f_1^s}{m_c^{*s} - m_v^{*s}}}\,, \tag{3.8}$$

$$\alpha^s = \frac{\hbar^2}{2m_v^{*s}} + \frac{(f_2^s a)^2}{f_1^s}\,, \tag{3.9}$$

$$\beta^s = \frac{\hbar^2}{2m_c^{*s}} - \frac{(f_2^s a)^2}{f_1^s}\,. \tag{3.10}$$

As mentioned before, s stands for the spin label. For each spin resolved band, the energy values E_{CB}^s (E_{VB}^s) and effective mass values $m_c^{*s} > 0$ ($m_v^{*s} < 0$) are listed in Table 3.1 and Appendix Table B.1, respectively. Spin splittings are interpreted individually for CB and VB as $\Delta_{\mathrm{CB}} = E_{\mathrm{CB}}^{\downarrow} - E_{\mathrm{CB}}^{\uparrow}$ and $\Delta_{\mathrm{VB}} = E_{\mathrm{VB}}^{\downarrow} - E_{\mathrm{VB}}^{\uparrow}$. The equation $f_1^{\uparrow} = f_1^{\downarrow} - \Delta_{\mathrm{CB}}^{\mathrm{SO}} + \Delta_{\mathrm{VB}}^{\mathrm{SO}}$ validates these splitting values. κ^s parameter is determined by comparing $\mathbf{k}\cdot\mathbf{p}$ and DFT isoenergy contours to fit with each other where also trigonal warping is observed. Lastly, η^s parameter is considered for better fitting of the bands away from the bandedge [119, 120, 113].
Using strained band gap values of DFT calculations, f_4 parameter is obtained by

$$E_g = f_1 + 2f_4(\varepsilon_{xx} + \varepsilon_{yy})\,. \tag{3.11}$$

Furthermore, another strain parameter f_5 is derived from

$$\Delta k_{x0} = \frac{f_5}{f_2 a}(\varepsilon_{xx} - \varepsilon_{yy}). \tag{3.12}$$

Here, Δk_{x0} shows the CBM shift along k-axis with uniaxial strain, found by DFT calculations.

3.1.2 Dichroism within $\mathbf{k}\cdot\mathbf{p}$ Hamiltonian

For a polarized light along the direction of unit vector $\hat{\epsilon}$, the momentum matrix element of the light for direct interband transition is

$$P_{\epsilon}^{cv}(\mathbf{k}) \equiv \langle u_c^s(\mathbf{k})|\, \hat{\epsilon}\cdot\mathbf{p}\, |u_v^s(\mathbf{k})\rangle\,, \tag{3.13}$$

and in terms of $\mathbf{k}\cdot\mathbf{p}$ Hamiltonian [134] can be written as

$$P_{\epsilon}^{cv}(\mathbf{k}) = \frac{m_0}{\hbar}\left\langle u_c^s\middle|\frac{\partial\mathcal{H}(\mathbf{k})}{\partial k_\epsilon}\middle|u_v^s\right\rangle. \tag{3.14}$$

CB and VB Bloch states are represented with $|u_{c,v}^s\rangle$ and free electron mass is denoted with m_0 [134]. Here, s label is removed for brevity in equations.
The momentum matrix element $\mathbf{p}_\pm = \hat{\epsilon}_\pm\cdot\mathbf{p}$ can be written as

$$\mathbf{p}_\pm = \mp\frac{1}{\sqrt{2}}\left(\frac{\partial\mathcal{H}}{\partial k_x} \pm i\frac{\partial\mathcal{H}}{\partial k_y}\right), \tag{3.15}$$

where $\hat{\epsilon}_\pm = \mp(\hat{x}\pm i\hat{y})/\sqrt{2}$ is left/right circular polarization. In the case of linear polarization, simply switching to $\hat{\epsilon}=\hat{x}$ and $\hat{\epsilon}=\hat{y}$ is sufficient.
If the two-band $\mathbf{k}\cdot\mathbf{p}$ Hamiltonian is expressed using the superposition Pauli matrices $\sigma_i = 0\ -\ 3$ and $\sigma_0 = 1$ where $\mathcal{H} = h_i\sigma_i$, assuming summation over the index i we have [135]

$$\mathcal{H} = \begin{pmatrix} h_0+h_3 & h_1-ih_2 \\ h_1+ih_2 & h_0-h_3 \end{pmatrix}. \tag{3.16}$$

In terms of $\overline{h} \equiv \sqrt{h_1^2+h_2^2+h_3^2}$, and $r \equiv (h_1+ih_2)/(\overline{h}+h_3)$, the eigenvectors become

$$|u_c\rangle = \frac{1}{\sqrt{1+|r|^2}}\begin{pmatrix}1\\ r\end{pmatrix}, \tag{3.17}$$

$$|u_v\rangle = \frac{1}{\sqrt{1+|r|^2}}\begin{pmatrix}-r^*\\ 1\end{pmatrix}. \tag{3.18}$$

Similarly, the derivatives of the $\mathbf{k}\cdot\mathbf{p}$ Hamiltonian along the direction of $\hat{\epsilon}$ can be written as $\partial_\epsilon\mathcal{H} = d_i^\epsilon\sigma_i$ and the momentum matrix element turns into

$$P_{\epsilon}^{cv} = \frac{m_0}{\hbar(1+|r|^2)}\left[-2d_3^\epsilon r^* + d_1^\epsilon\left(1-r^{*2}\right) - id_2^\epsilon\left(1+r^{*2}\right)\right]. \tag{3.19}$$

Using this expression and considering the interband absorption from valence to conduction bands, under a circularly-polarized electromagnetic field, the circular k-resolved optical polarization is [109]

$$\eta_C^{cv}(\mathbf{k}) = \frac{\left|P_+^{cv}(\mathbf{k})\right|^2 - \left|P_-^{cv}(\mathbf{k})\right|^2}{\left|P_+^{cv}(\mathbf{k})\right|^2 + \left|P_-^{cv}(\mathbf{k})\right|^2}\,, \tag{3.20}$$

while for the linear polarization

$$\eta_L^{cv}(\mathbf{k}) = \frac{\left|P_x^{cv}(\mathbf{k})\right|^2 - \left|P_y^{cv}(\mathbf{k})\right|^2}{\left|P_x^{cv}(\mathbf{k})\right|^2 + \left|P_y^{cv}(\mathbf{k})\right|^2}\,. \tag{3.21}$$

With the knowledge of d_i^ϵ, these equations can be calculated numerically through Equation 3.19.

3.1.3 $\partial\mathcal{H}/\partial k_\epsilon$ Expressions

In this part, we are going to work out the detailed forms of d_i^ϵ in Equation 3.19 for circular and linear polarization cases. Using $\epsilon = x, y$, we get the linear polarization components as

$$\frac{\partial\mathcal{H}_{\text{symm}}}{\partial k_\epsilon} = f_2 a\,\sigma_\epsilon, \tag{3.22}$$

$$\frac{\partial\mathcal{H}_{\text{asym}}}{\partial k_\epsilon} = 2k_\epsilon \begin{pmatrix} \beta & 0 \\ 0 & \alpha \end{pmatrix}, \tag{3.23}$$

while for $\epsilon = +, -$, circular polarization components are

$$\partial_\pm\mathcal{H}_{\text{symm}} = \mp\sqrt{2} f_2 a \sigma_\pm, \tag{3.24}$$

$$\partial_\pm\mathcal{H}_{\text{asym}} = -\sqrt{2}k_\mp \begin{pmatrix} \beta & 0 \\ 0 & \alpha \end{pmatrix}. \tag{3.25}$$

Here, $\sigma_\pm = (\sigma_x \pm i\sigma_y)/2$. Following the same procedure, the rest of the derivative equations for linear and circular polarization are

$$\partial_x \mathcal{H}_{\mathrm{TW}} = 2\kappa \begin{pmatrix} 0 & k_+ \\ k_- & 0 \end{pmatrix}, \tag{3.26}$$

$$\partial_y \mathcal{H}_{\mathrm{TW}} = 2i\kappa \begin{pmatrix} 0 & k_+ \\ -k_- & 0 \end{pmatrix}, \tag{3.27}$$

$$\partial_+ \mathcal{H}_{\mathrm{TW}} = -2\sqrt{2}\kappa \begin{pmatrix} 0 & 0 \\ k_- & 0 \end{pmatrix}, \tag{3.28}$$

$$\partial_- \mathcal{H}_{\mathrm{TW}} = 2\sqrt{2}\kappa \begin{pmatrix} 0 & k_+ \\ 0 & 0 \end{pmatrix}, \tag{3.29}$$

$$\partial_x \mathcal{H}_{\mathrm{cub}} = \frac{\eta}{2} \begin{pmatrix} 0 & 4k_x^2 - k_+^2 \\ 4k_x^2 - k_-^2 & 0 \end{pmatrix}, \tag{3.30}$$

$$\partial_y \mathcal{H}_{\mathrm{cub}} = i\frac{\eta}{2} \begin{pmatrix} 0 & -4k_y^2 - k_+^2 \\ 4k_y^2 + k_-^2 & 0 \end{pmatrix}, \tag{3.31}$$

$$\partial_+ \mathcal{H}_{\mathrm{cub}} = -\frac{\eta}{\sqrt{2}} \begin{pmatrix} 0 & 2k_+k_- \\ k_+^2 & 0 \end{pmatrix}, \tag{3.32}$$

$$\partial_- \mathcal{H}_{\mathrm{cub}} = \frac{\eta}{2} \begin{pmatrix} 0 & k_-^2 \\ 2k_+k_- & 0 \end{pmatrix}. \tag{3.33}$$

3.1.4 Approximate Analytical Expressions

Baring in mind the $\mathcal{H}_{symm}$ and $\mathcal{H}_{asymm}$ terms of the $\mathbf{k}\cdot\mathbf{p}$ Hamiltonian given in the Equations 3.1 and 3.2, the linear polarization matrix elements turn into

$$P_x^{cv} = \tfrac{m_0}{\hbar(1+|r|^2)} \left[-2k_x(\beta-\alpha)r^* + f_2 a\left(1-r^{*2}\right)\right], \tag{3.34}$$

$$P_y^{cv} = \tfrac{m_0}{\hbar(1+|r|^2)} \left[-2k_y(\beta-\alpha)r^* - if_2 a\left(1+r^{*2}\right)\right]. \tag{3.35}$$

In the circular polarization case, they become

$$P_+^{cv} = \tfrac{\sqrt{2}m_0}{\hbar(1+|r*|^2)} \left[k_-(\beta-\alpha)r^* - f_2 a\right], \tag{3.36}$$

$$P_-^{cv} = \tfrac{\sqrt{2}m_0}{\hbar(1+|r*|^2)} \left[k_+(\beta-\alpha)r^* - f_2 a r^{*2}\right]. \tag{3.37}$$

If we only consider the influence of $\mathcal{H}_{symm}$ term in order to simplify the calculations, we get the linear polarization as

$$\eta_L^{cv} = \frac{\left|1 - r^{*2}\right|^2 - \left|1 + r^{*2}\right|^2}{|1 - r^{*2}|^2 + |1 + r^{*2}|^2} = \frac{2(h_2^2 - h_1^2)(h_3 + \overline{h})^2}{(h_1^2 + h_2^2)^2 + (h_3 + \overline{h})^4}. \tag{3.38}$$

As will be shown later, this helps to understand the effects of certain parameters while calculating linear polarization dichroism under uniaxial strain. Using the same approximation, the circular polarization can be stated as

$$\eta_C^{cv} = \frac{1 - |r|^4}{1 + |r|^4} = \frac{(h_3 + \overline{h})^4 - (h_1^2 + h_2^2)^2}{(h_1^2 + h_2^2)^2 + (h_3 + \overline{h})^4}. \tag{3.39}$$

3.2 Results

3.2.1 DFT Results

To begin with pristine TMDs, the band structures and the band gaps which are provided in Appendix Figure B.1 are in agreement with previous studies [120]. Meanwhile, results for JTMDs in Figure 3.1 marginally differ available publications [136, 83, 137, 138]. In both figures, the electronic band structure for TMDs and JTMDs are plotted with PBE and PBE+SOC with valence band maximum aligned to zero. It is observed that at the K high symmetry point of VBM and CBM, with the exception of MoSTe and WSTe, the materials have direct band gap. Even though PBE (1.55 eV) and PBE+SOC (1.57 eV) give very close results by 20 meV for MoSSe, the direct band gap nature becomes more visible when PBE+SOC is considered. As a matter of fact, this small change is responsible for a variety of indirect [136, 83, 137, 138] vs direct [92, 139, 86, 140] gap results in literature. Besides MoSSe, for other JTMD materials such as WSSe, MoSeTe and WSeTe results, discrepancy is reported [137, 136, 86, 140, 92]. Keeping in mind these disagreement, we have gone through over our DFT and DFT+SOC calculations again.

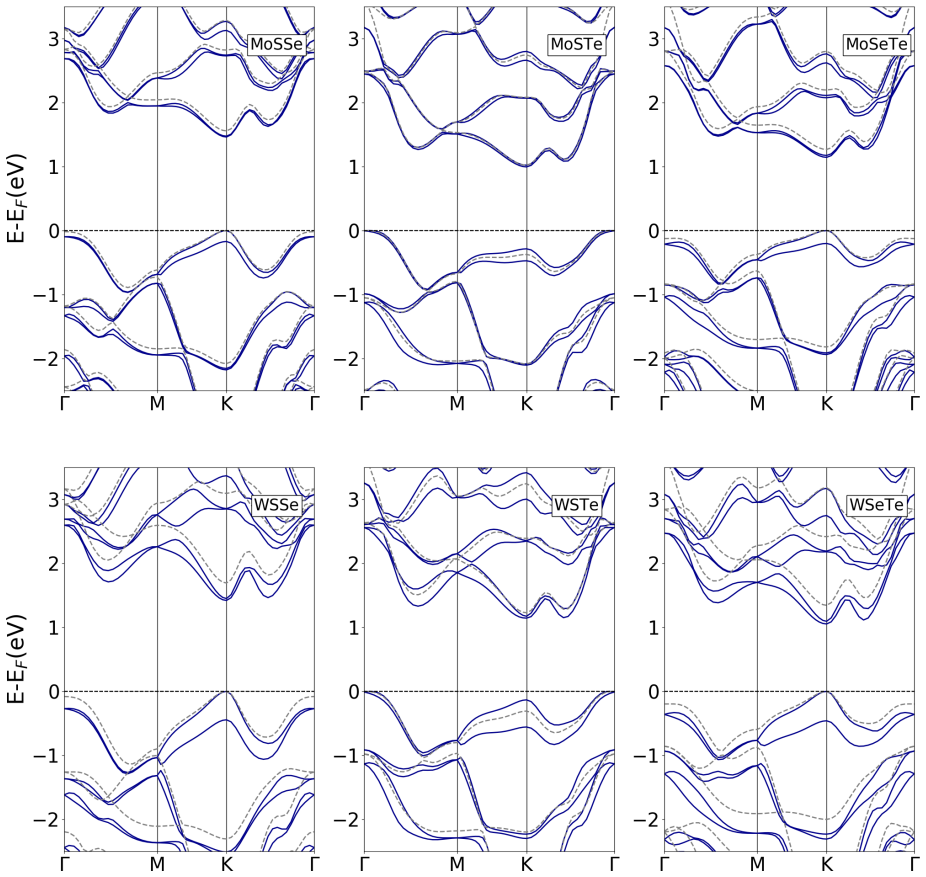


Figure 3.1: The electronic band structures of MoXX' and WXX' with PBE (gray/dashed) and PBE+SOC (blue/solid).

	E_{gap}^{PBE} (eV)	E_{gap}^{HSE} (eV)	$E_{gap}^{PBE+SOC}$ (eV)	$E_{gap}^{HSE+SOC}$ (eV)
MoS_2	1.66	2.13	1.58	2.02
$MoSe_2$	1.43	1.89	1.32	1.72
$MoTe_2$	1.08	1.46	0.94	1.27
WS_2	1.80	2.29	1.54	1.99
WSe_2	1.53	2	1.24	1.64
WTe_2	1.06	1.47	0.74	1.07
MoSSe	1.55	2.01	1.45	1.87
MoSTe	1.01 (I)	1.49 (I)	0.99 (I)	1.45 (I)
MoSeTe	1.28	1.69	1.12	1.50
WSSe	1.68	2.16	1.41	1.84
WSTe	1.24 (I)	1.71 (I)	1.16 (I)	1.62 (I)
WSeTe	1.34	1.78	1.05	1.41

Table 3.1: Band Gaps Calculated with PBE and HSE compared with and without SOC where the band gaps refer to KK points for direct materials and ΓK points for indirect materials designated with I (MoSTe and WSTe).

Corresponding band gap values for TMDs and JTMDs are given in Table 3.1. Appendix Figure B.1 and Table 3.1 show that as the chalcogen atom varies through S→Se→Te, the band gap decreases along with this change. In Figure 3.1, the electronic band structures of JTMDs also exhibit this distinctive change. Additionally, by taking the average of band gap values of two TMDs, it is possible to estimate the band gap of corresponding JTMD. As an example, MoS_2 (1.66 eV) and $MoSe_2$ (1.43 eV) gives the average of MoSSe (1.56 eV) gap value. HSE results over PBE and PBE+SOC increase the band gap values by 0.4-0.5 eV while maintaining the band structure characteristics.

Effect of the SOC addition over the band structure of JTMDs is distinguishable compared to TMDs [120]. When SOC addition is considered, the band gap values decrease by 0.1-0.3 eV for PBE and 0.1-0.4 eV for HSE. Direct and indirect behaviour of JTMDs in Figure 3.1 are preserved for HSE. Considering that Mo compounds are lighter than W ones, MoX_2 and $MoXX'$ have smaller splitting values with SOC as presented in Table 3.2. HSE increases the splitting values further, especially for W compounds. The band gap and splitting values are in accordance with the previous studies [120] for TMD and JTMD materials.

	Δ_{VB}^{PBE} (meV)	Δ_{CB}^{PBE} (meV)	Δ_{VB}^{HSE} (meV)	Δ_{CB}^{HSE} (meV)
MoS_2	150	-30	210	-20
$MoSe_2$	180	-20	280	-40
$MoTe_2$	220	-40	350	-70
WS_2	430	30	550	1
WSe_2	470	30	620	3
WTe_2	490	50	740	2
MoSSe	220	-20	240	-30
MoSTe	200	-30	280	-50
MoSeTe	200	-40	310	-60
WSSe	440	30	580	2
WSTe	420	30	580	1
WSeTe	470	40	630	10

Table 3.2: Splittings in CB and VB calculated with PBE and HSE[a] where the splittings are calculated at K point for CB and VB, except for MoSTe and WSTe at Γ point for VB. For all splitting calculations $E_{CB/VB}^{\downarrow} - E_{CB/VB}^{\uparrow}$ formula is used.

3.2.1.1 Strain with DFT Results

Strained DFT calculations are essential for exploring linear and circular dichroism response to under take the $\mathbf{k} \cdot \mathbf{p}$ parametrization. For this purpose, the electronic band structures with strain are plotted in Appendix Figures B.2-B.9 for the range -2% to 2%, under uniaxial ($\varepsilon_{xx} \neq 0,\ \varepsilon_{yy} = 0$) and biaxial ($\varepsilon_{xx} = \varepsilon_{yy} \neq 0$) compressive and tensile strain of MXX$'$ (M=Mo,W and X,X'=S,Se,Te). In Figure 3.2(a), it is observed that with biaxial strain at K point, the band gap is modified. Taking into account this difference in the band gaps and using Equation 3.11, f_4 parameter is extracted. Additionally, Appendix Figures B.2-B.5 exhibit indirect and direct band gap transformations. So, changes in the gap around this region is sufficient for further calculations.

While hexagonal crystal is used for biaxial strain, tetragonal crystal structure is preferred in order to simplify the uniaxial strain calculations. The latter has $a = b \neq c$ for unstrained material. With uniaxial strain, the lattice parameters become $a \neq b \neq c$ as one of the sides of the crystal is distorted and transformed into orthorombic structure. Figure 3.3 shows the hexagonal and orthorombic structures which are used in unstrained/strained calculations as well as their crystal paths.

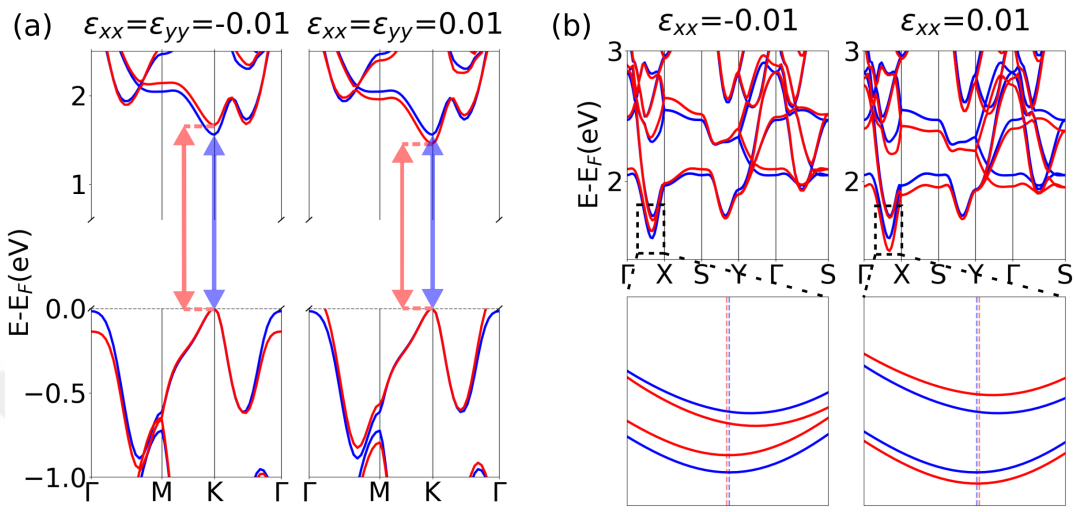


Figure 3.2: The band structure change of MXX' under (a) biaxial strain (b) uniaxial strain.

In Figure 3.2(b), a shift appears at k axis of CBM, when the system is under uniaxial strain along x axis of the crystal. Employing Equation 3.12, f_5 parameter of $\mathbf{k}\cdot\mathbf{p}$ parameter set is evaluated where inset graph with Cartesian coordinates of Figure 3.2(b) reveals this shift more clearly. Appendix Figure 3.1 shows that, for unstrained cases, MoSTe and WSTe have indirect band gap at ΓK. The aim of $\mathbf{k}\cdot\mathbf{p}$ calculations here is to discover the modification in the K valley, so that only direct band gap materials are studied. 1% tensile strain calculation is utilized for these materials, in order to get $\mathbf{k}\cdot\mathbf{p}$ parameters.

3.2.2 $\mathbf{k}\cdot\mathbf{p}$ Results

The performance of $\mathbf{k}\cdot\mathbf{p}$ method with respect to the DFT results around VBM and CBM needs to be demonstrated [119, 120, 123, 113]. This straightforward method gives immensely sufficient results for JTMDs with direct band gaps. Spin up and down bands of $\mathbf{k}\cdot\mathbf{p}$ methods vs DFT with SOC are presented in Figures 3.4 and 3.5, and the spinless version is available in Appendix Figure B.11. Additionally, remaining $\mathbf{k}\cdot\mathbf{p}$ vs DFT band structures can be found in Appendix Figure B.10. Executing the fitting expressions in given order in Section 3.1.1, we have obtained the related $\mathbf{k}\cdot\mathbf{p}$ parameters step by step. Earlier DFT band gap

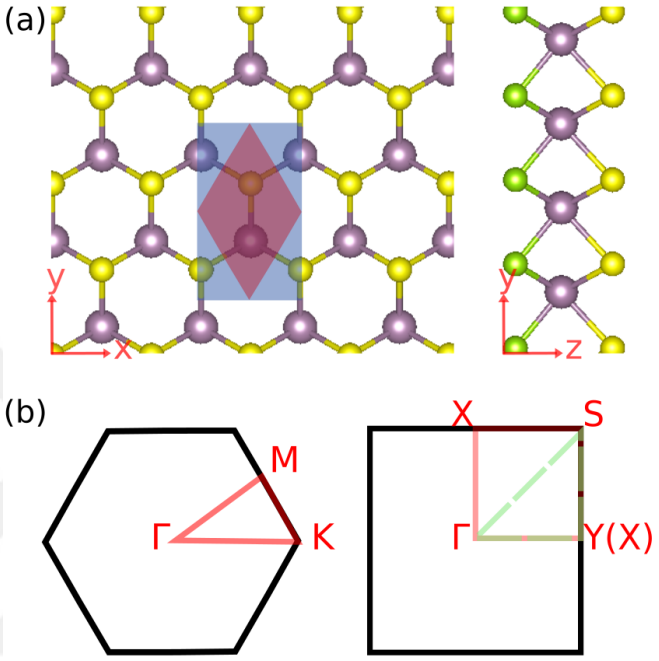


Figure 3.3: (a) Top and side view of JTMDs. (b) High symmetry points corresponding for hexagonal and orthorhombic (tetragonal) lattice, respectively.

	a	f_1	f_2	f_4	f_5	α	β	κ	η
MoS_2	3.18	2.14	1.24	-3.29	2.57	0.69	0.85	-2.0	3.5
$MoSe_2$	3.32	1.89	1.04	-2.94	2.17	0.49	0.58	-1.7	3.0
$MoTe_2$	3.55	1.5	0.85	-2.43	1.77	0.56	0.68	-1.8	3.0
WS_2	3.18	2.31	1.55	-3.82	3.22	1.29	1.71	-2.0	3.5
WSe_2	3.32	2.01	1.34	-3.53	2.77	1.13	1.47	-1.9	3.5
WTe_2	3.55	1.47	1.1	-2.99	2.29	1.32	1.75	-1.8	2.5
MoSSe	3.25	2.02	1.1	-3.10	2.29	0.64	0.80	-1.9	3.5
MoSeTe	3.43	1.7	0.87	-2.69	1.82	0.65	0.86	-1.8	2.5
WSSe	3.25	2.18	1.4	-3.68	2.90	1.24	1.68	-2.0	3.5
WSeTe	3.43	1.79	1.13	-3.32	2.35	1.25	1.78	-2.0	3.0

Table 3.3: Spinless $\mathbf{k}\cdot\mathbf{p}$ parameters a (Å) f_1 (eV), f_2 (eV), f_4 (eV), f_5 (eV), α (eV Å^2), β (eV Å^2), κ (eV Å^2) and η (eV Å^3).

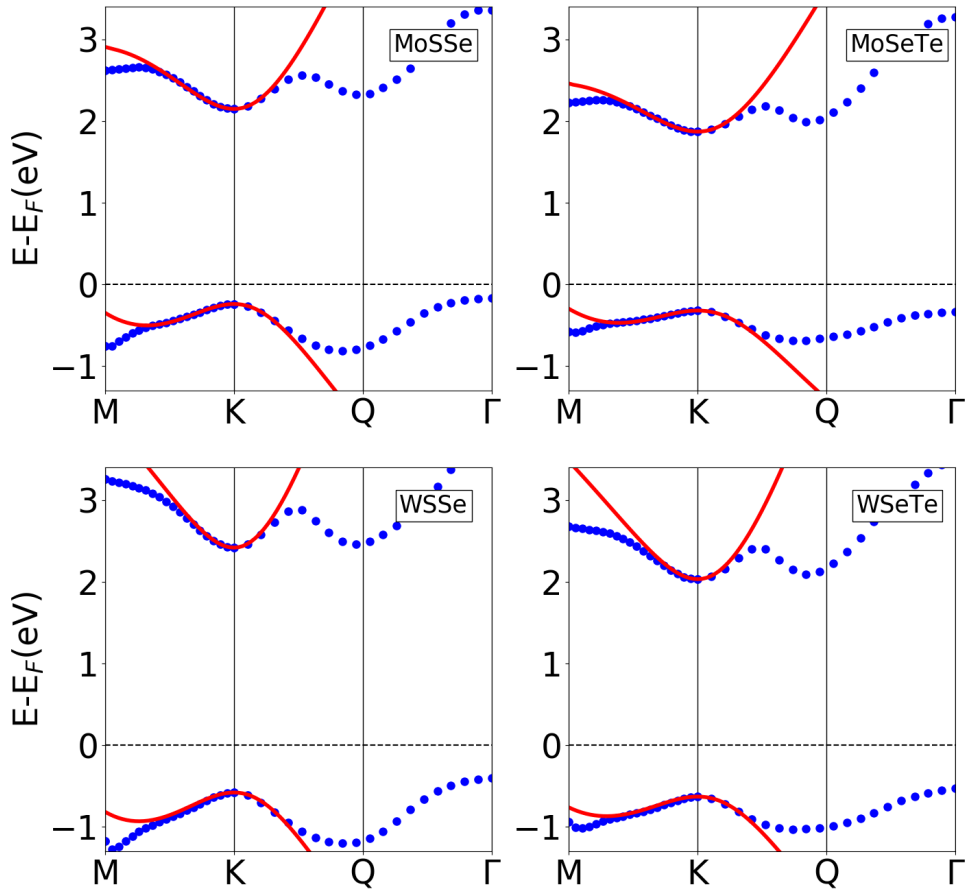


Figure 3.4: Spin up bands with SOC for $\mathbf{k} \cdot \mathbf{p}$ (solid lines) vs DFT(•).

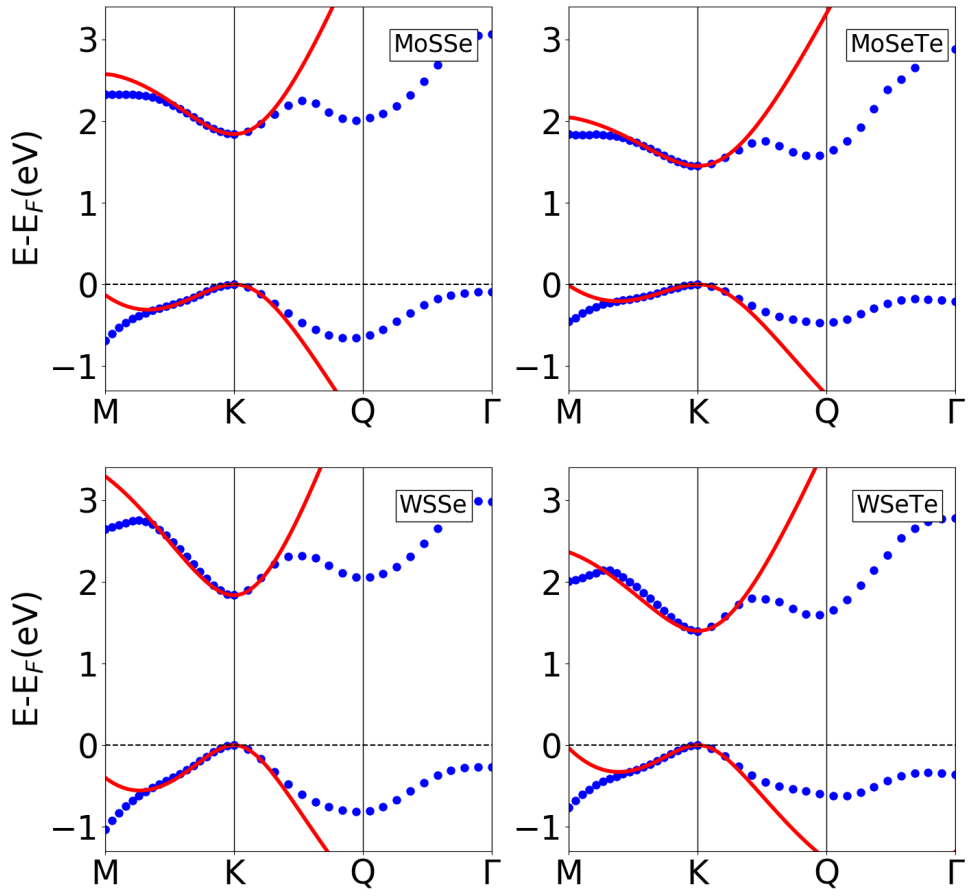


Figure 3.5: Spin down bands with SOC for $\mathbf{k} \cdot \mathbf{p}$ (solid lines) vs DFT(•).

	$f_1\uparrow$	$f_1\downarrow$	$f_2\uparrow$	$f_2\downarrow$	$\alpha\uparrow$	$\alpha\downarrow$	$\beta\uparrow$	$\beta\downarrow$	$\kappa\uparrow$	$\kappa\downarrow$	$\eta\uparrow$	$\eta\downarrow$
MoS_2	2.25	2.02	1.23	1.25	0.66	0.72	0.82	0.88	-2.2	-2.4	3.1	3.2
$MoSe_2$	2.04	1.72	1.04	1.03	0.5	0.51	0.6	0.61	-2.1	-2.5	3.0	3.3
$MoTe_2$	1.69	1.27	0.86	0.83	0.61	0.56	0.79	0.67	-2.0	-2.3	3.2	3.2
WS_2	2.54	1.99	1.5	1.57	1.19	1.4	1.62	1.82	-2.0	-2.0	3.0	3.0
WSe_2	2.26	1.64	1.29	1.34	1.05	1.21	1.42	1.51	-1.9	-1.9	3.0	3.2
WTe_2	1.8	1.07	1.1	1.09	1.28	1.41	1.83	1.76	-1.5	-1.6	3.3	3.3
MoSSe	2.15	1.87	1.1	1.1	0.71	0.62	0.93	0.76	-2.0	-2.3	3.0	3.0
MoSeTe	1.87	1.5	0.88	0.86	0.73	0.62	1.04	0.8	-1.9	-2.1	3.0	3.1
WSSe	2.42	1.84	1.33	1.42	0.97	1.52	1.3	2.06	-2.0	-1.9	3.0	3.0
WSeTe	2.03	1.41	1.06	1.14	0.68	1.81	0.87	2.72	-2.1	-2.0	3.0	2.8

Table 3.4: Spinful $\mathbf{k}\cdot\mathbf{p}$ parameters f_1 (eV), f_2 (eV), α (eV Å^2), β (eV Å^2), κ (eV Å^2) and η (eV Å^3).

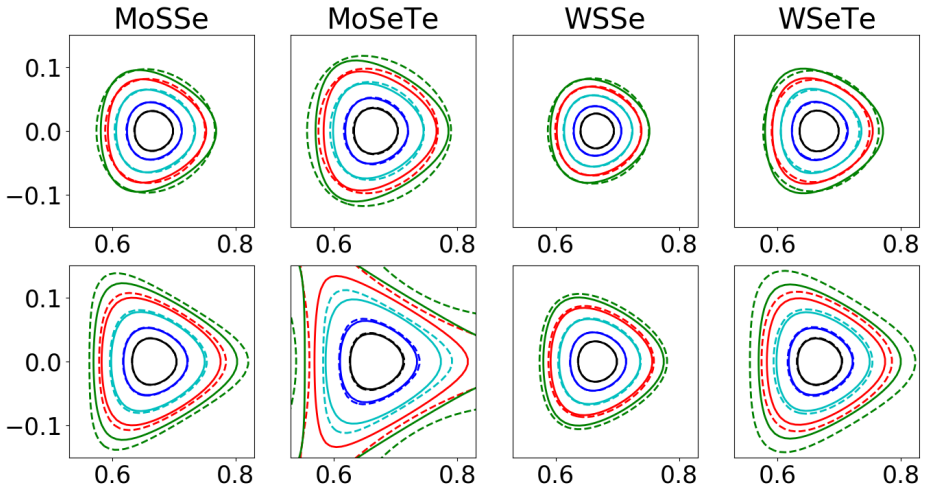


Figure 3.6: Isoenergy contours with SOC for $\mathbf{k}\cdot\mathbf{p}$ (solid lines) vs DFT (dashed lines) for spin up case at K valley. The energies (0.025, 0.05, 0.1, 0.15, 0.2 eV) are represented with (black, blue, turquoise, red and green lines).

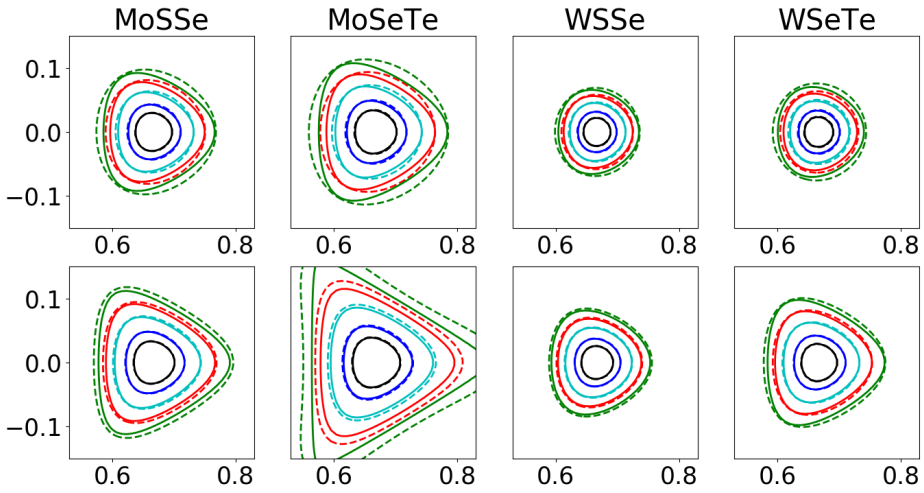


Figure 3.7: Isoenergy contours with SOC for $\mathbf{k}\cdot\mathbf{p}$ (solid lines) vs DFT (dashed lines) for spin down case at K valley. The energies (0.025, 0.05, 0.1, 0.15, 0.2 eV) are represented with (black, blue, turquoise, red and green lines).

results presented in Table 3.1 are used for the band gaps without strain. The effective mass (m^*) values needed in the calculations of f_2, α, and β parameters are given in Appendix Table B.1.

Spinless and spinful $\mathbf{k}\cdot\mathbf{p}$ parameters are tabulated in Table 3.3 and 3.4, respectively. A few observations can be mentioned for these results. In Figure 3.6 and 3.7, the isoenergy plots for spin up and down bands for $\mathbf{k}\cdot\mathbf{p}$ vs DFT are in satisfactory agreement for JTMD materials when triagonal warping parameter κ is considered in the calculations. Even, 200 meV offset away from K point band-edge is well reproduced in these results. Keeping in mind that, for $\widehat{H}_{\text{cub}}$ term, the diagonal terms are negligible in Equation 3.4, only off diagonal terms are employed. η parameter addition is helpful for further $\mathbf{k}\cdot\mathbf{p}$ fitting and this worked well for KM panel as seen in Figure 3.4 and 3.5. However, at $K\Gamma$ panel after Q point, this fit becomes less accurate. A better fit over $Q\Gamma$ panel is refrained, since the materials become semimetallic. With this parameter set, remaining panels fit well so this is not a setback for the overall performance.

In accordance with spinless biaxial and uniaxial DFT calculations, f_4 and f_5 parameters are obtained and added to the rest of the $\mathbf{k}\cdot\mathbf{p}$ parameter set in Table 3.3. Comparing with the previous PBE results [123], our f_4 parameters which

are presented also in Appendix Table B.6 are larger, since the band gaps are calculated with HSE over PBE. The shift that is observed in Figure 3.2(b) along k-axis, does not depend much on whether the calculations are done by PBE or HSE, so that our f_5 and previous results are in agreement as in Appendix Table B.6.

3.2.2.1 Dichroism Results

3.2.2.1.1 Linear Dichroism Response (K point)

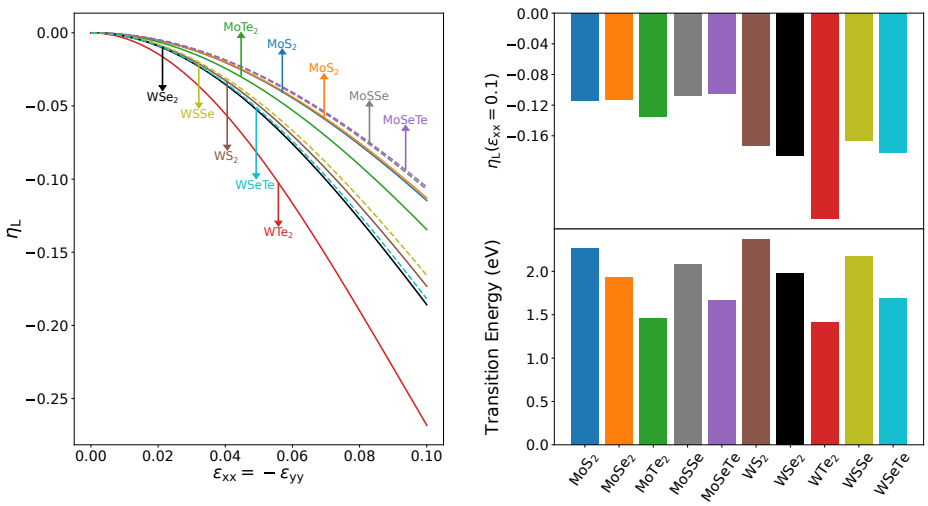


Figure 3.8: The linear dichroism variation under uniaxial-only strain at the K point for the spin-down transition (left). $\eta_L(\epsilon_{xx} = 0.1)$ and transition energy values for the ten (J)TMDs (right).

TMDs and JTMDs posses symmetry at the K point [115] for unstrained and biaxial strain cases, that causes LD to vanish. Under uniaxial strain, the symmetry of the system is altered and LD (η_L) becomes non zero at this high symmetry point, which is seen in Figure 3.8 for spin-down/bandedge transition. η_L changes quadratically up to $\epsilon_{xx} = 0.1$ at the K point under uniaxial-only strain ($\epsilon_{xx} = -\epsilon_{yy}, \epsilon_{xy} = 0$). When the transition energies are considered in Figure 3.8, WTe_2 and MoSeTe have the highest and lowest uniaxial responsitivity for LD,

respectively. In Appendix Figure B.18, this behaviour is maintained for spinless situation. It may be suspected that f_5 amount might effect this result. However, as given in Table 3.3, eventhough WS_2 has a larger f_5 value, this does not give rise to a higher LD responsitivity than WTe_2. Further inspecting, studying Equation 3.38 shows that the small energy gap has importance for η_L, $\mathcal{H}_{symm}$ term of the $\mathbf{k} \cdot \mathbf{p}$ Hamiltonian.

3.2.2.1.2 Circular and Linear Dichrosim Under Strain (K valley)

In order to understand how strain effects η_L and η_C, three variations of strain, namely biaxial, uniaxial and shear strain, are taken into account for spin-down bandedge transition energy. Because of the highest η_L value of WTe_2, for this part η_L and η_C values are plotted for WSe_2, WTe_2 and WSeTe in Figure 3.9. Plots for the rest of the materials are displayed in Appendix Figures B.23, B.24, B.25. In Figure 3.9, results of unstrained, biaxial-only, uniaxial-only and shear-only strain are shown for detailed comparison. For these plots, $[-0.25, +0.25]$ square area around the K point in $1/\text{Å}$ units is used. Considering all of the materials presented in Appendix Figures B.23-B.24, TMDs have smaller variation of η_L and η_C. Baring in mind Equation 3.38, η_L and $\Delta\eta_L$ changes sign under biaxial and shear strain along k_x and k_y at ΓK and ΓM regions, respectively. From a practical point of view, suspended (J)TMD membranes can be examined on linear polarization measurements under strain.

Moreover, we have studied which Hamiltonian terms are more effective on dichroism. We have observed that particularly $\mathcal{H}_{3w}$ trigonal warping term has remarkable change in comparison of Figure 3.9 and 3.10 for η_C value. As shown in Equation 3.2, electron-hole asymmetry causes CB and VB Berry Curvature to be separated and this affects CD for TMDs contrary to graphene [109]. Appendix Figures B.21 and B.22 show that, the rest of the Hamiltonian terms are less effective.

We are unable to compare our results with existing studies, since very limited is available. A report [135], acknowledges CD for MoS_2 when it transforms into

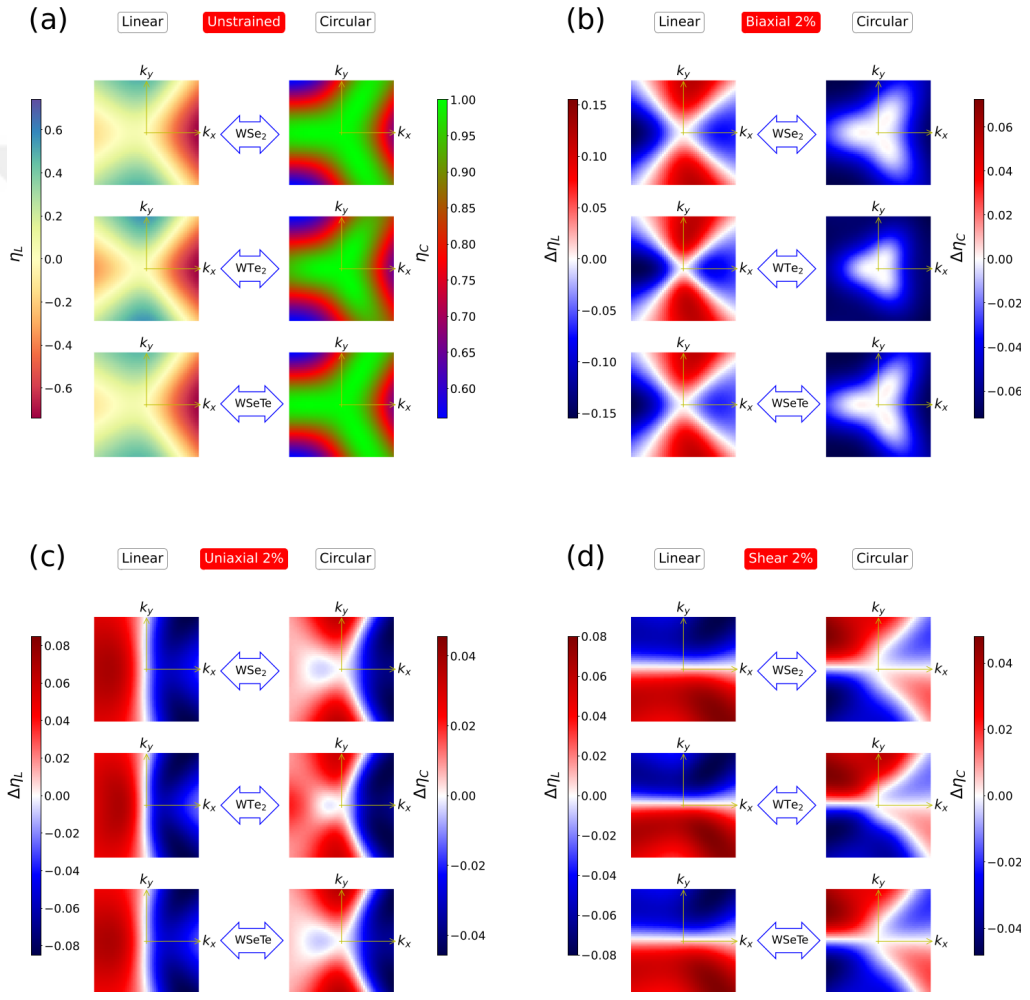


Figure 3.9: For WSe_2, WTe_2, and janus WSeTe spin-down transition, (a) the linear and circular dichroism variation ($\eta_{L,C}$) at K valley without strain and the deviation from unstrained case ($\Delta\eta_{L,C}$) at K point under (b) biaxial-only, (c) uniaxial-only, (d) shear-only strain. $[-0.25, +0.25]$ square area around the K point in $1/\text{Å}$ along each direction is demonstrated.

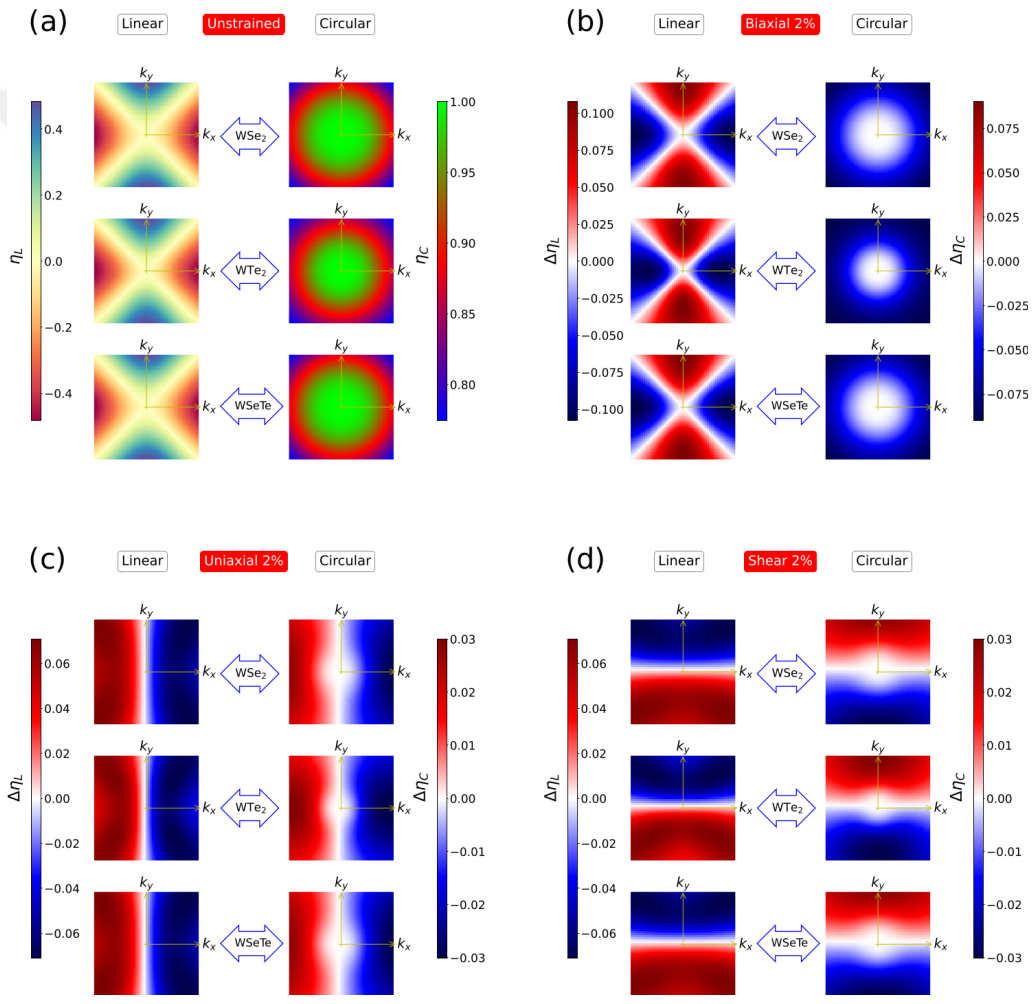


Figure 3.10: Identical calculations are considered with previous figure, except the trigonal warping term of the $\mathbf{k} \cdot \mathbf{p}$ Hamiltonian is not included.

an indirect band gap material under 5% uniaxial strain. In this thesis, we have found that except MS_2 and MSSe (M=Mo,W), up to 2% strain, the covered materials tend to have direct band gaps. Our unstrained MoS_2 result in Appendix Figure B.19 is in accordance with Reference [141]. Appendix Figures B.21 and B.22 provide additional information about the effect of $\mathcal{H}_{symm}$ and $\mathcal{H}_{asymm}$ terms over η_C for WSe_2, WTe_2 and WSeTe.

Chapter 4

Conclusions

4.1 *h*-BN Defects with DFT-1/2

Progress in quantum technologies demand point defects hosted in materials like monolayer h-BN with a large band gap. Computational techniques such as DFT are known to miscalculate the band gap. Detecting defect energy levels that are close to the bands or hidden inside them is a crucial difficulty in such cases. With the DFT-1/2 variant, we have offered a way to mitigate this problem. Calculations over different types of defects in h-BN revealed that LDA-1/2 method is more powerful over spotting the defect states with enhanced band gap, compared to PBE-1/2. Under circumstances such as lacking of experimental data or highly demanding computational alternatives (e.g. HSE or GW), DFT-1/2 is a favorable method for defect centers having a considerably large number of atoms within the supercell.

4.2 (J)TMDs with $\mathbf{k} \cdot \mathbf{p}$ Method

In the second part of our thesis, we have accomplished finding $\mathbf{k} \cdot \mathbf{p}$ parameters for ten different monolayer (J)TMDs possessing a direct band gap. These parameters are calculated by introducing electron-hole asymmetry, trigonal warping and cubic terms one by one, and additionally we have considered the influence of biaxial and uniaxial strain. The $\mathbf{k} \cdot \mathbf{p}$ fitting procedure is built upon our DFT and HSE electronic band structure calculations with and without SOC. Moreover, DFT computations under strain have been helpful to find the strain $\mathbf{k} \cdot \mathbf{p}$ parameters. As opposed to having a better piezoelectricity which was previously documented, JTMDs do not exhibit a significant superiority over the TMD counterparts, according to the different parameter calculations around K valley. When the CD and LD are calculated using $\mathbf{k} \cdot \mathbf{p}$ band structure, distinct responses have been observed for uniaxial, biaxial and shear strain cases. As a promising application of our findings, identifying the deformation type of the monolayer (J)TMDs is possible through the measurement of polarized absorption. According to the electronic structure calculations, CD is found to be affected mostly by the trigonal warping term of the $\mathbf{k} \cdot \mathbf{p}$ Hamiltonian at K valley. In case of LD, WTe_2 exhibits the largest responsitivity, which gives an opportunity for use in optical polarizers under strain.

4.3 Suggestions for further research

In this final section, we would like to list some personal suggestions for further scrutiny, starting with h-BN defects. Previously, NV^- center is characterized using DFT-1/2 [31], here there is an opportunity for analyzing 2D charged h-BN defects. Also, different combinations of vacancies (double nitrogen or double boron vacancies etc.) or impurities with other atoms (Si,Ge, O, S, Se etc.) can be examined using DFT-1/2. Another paper has investigated various h-BN defects from the standpoint of ZPL [59]. A similar work over the mentioned defects in this thesis can be performed using DFT-1/2 method. Other optical properties

such as dielectric function, absorption coefficient etc. are calculated for defects in different materials such as vacancies in h-ZnSe [142], which can be replicated for h-BN. Most importantly, we recommend to use additional data especially experimental values for defect energies to fully assess the accuracy of DFT-1/2 results.

Research opportunities on JTMDs are wide open since their investigation has just begun. The fabrication of the janus materials is a crucial advancement. Unfortunately, when $WTe_{2x}S_{2(1-x)}$ alloys (for $x = 0.4 - 0.6$) are fabricated by using CVD technique, a phase transition of 1H semiconducting to 1T$'$ metallic phase occurs [143]. In this case, for further experimental examination, 1H WTe_2 phase needs to be stabilized under strained conditions. Earlier, experimental and theoretical pressure studies are done for MoSSe and WSSe [78] and similar theoretical studies can be repeated for MSTe and MSeTe (M=Mo, W) in the future. A stable janus material MoSTe is considered for piezoelectronic properties [76], yet this feature of WSTe is unexplored. Even though there are studies on magnetic properties of MoSSe and WSSe materials, it remains to be extended to MSTe or MSeTe. Finally, in this thesis, we have analyzed the direct band gap janus materials, however as proposed for TMDs [120] earlier, other valleys different than K-valley can be characterized using $\mathbf{k} \cdot \mathbf{p}$ method, which gives a chance for indirect band gap material calculations [127].

Bibliography

[1] M. Atatüre, D. Englund, N. Vamivakas, S.-Y. Lee, and J. Wrachtrup, "Material platforms for spin-based photonic quantum technologies," *Nat. Rev. Mater.*, vol. 3, no. 5, p. 38, 2018.

[2] I. Aharonovich, D. Englund, and M. Toth, "Solid-state single-photon emitters," *Nat. Photon.*, vol. 10, no. 10, p. 631, 2016.

[3] V. Ivády, I. A. Abrikosov, and A. Gali, "First principles calculation of spin-related quantities for point defect qubit research," *NPJ Comput. Mater.*, vol. 4, no. 1, p. 76, 2018.

[4] A. Lohrmann, B. Johnson, J. McCallum, and S. Castelletto, "A review on single photon sources in silicon carbide," *Rep. Prog. Phys.*, vol. 80, no. 3, p. 034502, 2017.

[5] W. Gao, A. Imamoglu, H. Bernien, and R. Hanson, "Coherent manipulation, measurement and entanglement of individual solid-state spins using optical fields," *Nat. Photon.*, vol. 9, no. 6, p. 363, 2015.

[6] P. Hohenberg and W. Kohn, "Inhomogeneous electron gas," *Physical review*, vol. 136, no. 3B, p. B864, 1964.

[7] J. P. Perdew, K. Burke, and M. Ernzerhof, "Generalized gradient approximation made simple," *Physical review letters*, vol. 77, no. 18, p. 3865, 1996.

[8] R. W. Godby, M. Schlüter, and L. J. Sham, "Self-energy operators and exchange-correlation potentials in semiconductors," *Phys. Rev. B*, vol. 37, pp. 10159–10175, Jun 1988.

[9] J. P. Perdew, W. Yang, K. Burke, Z. Yang, E. K. U. Gross, M. Scheffler, G. E. Scuseria, T. M. Henderson, I. Y. Zhang, A. Ruzsinszky, H. Peng, J. Sun, E. Trushin, and A. Görling, "Understanding band gaps of solids in generalized kohn–sham theory," *P. Natl. A. Sci.*, vol. 114, no. 11, pp. 2801–2806, 2017.

[10] J. Heyd, G. E. Scuseria, and M. Ernzerhof, "Hybrid functionals based on a screened coulomb potential," *J. Chem. Phys.*, vol. 118, no. 18, pp. 8207–8215, 2003.

[11] L. Hedin, "New method for calculating the one-particle green's function with application to the electron-gas problem," *Phys. Rev.*, vol. 139, pp. A796–A823, Aug 1965.

[12] L. G. Ferreira, M. Marques, and L. K. Teles, "Approximation to density functional theory for the calculation of band gaps of semiconductors," *Physical Review B*, vol. 78, no. 12, p. 125116, 2008.

[13] W. Kohn and L. J. Sham, "Self-consistent equations including exchange and correlation effects," *Physical review*, vol. 140, no. 4A, p. A1133, 1965.

[14] J. C. Slater and K. H. Johnson, "Self-consistent-field x α cluster method for polyatomic molecules and solids," *Physical Review B*, vol. 5, no. 3, p. 844, 1972.

[15] J. F. Janak, "Proof that $\partial e/\partial n_i = \varepsilon$ in density-functional theory," *Physical Review B*, vol. 18, no. 12, p. 7165, 1978.

[16] L. G. Ferreira, M. Marques, and L. K. Teles, "Slater half-occupation technique revisited: the lda-1/2 and gga-1/2 approaches for atomic ionization energies and band gaps in semiconductors," *Aip Advances*, vol. 1, no. 3, p. 032119, 2011.

[17] A. Belabbes, C. Panse, J. Furthmüller, and F. Bechstedt, "Electronic bands of iii-v semiconductor polytypes and their alignment," *Phys. Rev. B*, vol. 86, p. 075208, Aug 2012.

[18] R. R. Pelá, M. Marques, and L. K. Teles, "Comparing lda-1/2, hse03, hse06 and g 0 w 0 approaches for band gap calculations of alloys," *J. Phys.: Condens. Matter*, vol. 27, no. 50, p. 505502, 2015.

[19] S. X. Tao, X. Cao, and P. A. Bobbert, "Accurate and efficient band gap predictions of metal halide perovskites using the dft-1/2 method: Gw accuracy with dft expense," *Sci. Rep.*, vol. 7, no. 1, p. 14386, 2017.

[20] F. Matusalem, M. Marques, L. K. Teles, and F. Bechstedt, "Stability and electronic structure of two-dimensional allotropes of group-iv materials," *Phys. Rev. B*, vol. 92, p. 045436, Jul 2015.

[21] J. Doumont, F. Tran, and P. Blaha, "Limitations of the dft–1/2 method for covalent semiconductors and transition-metal oxides," *Phys. Rev. B.*, vol. 99, no. 11, p. 115101, 2019.

[22] I. Guilhon, D. Koda, L. Ferreira, M. Marques, and L. Teles, "Approximate quasiparticle correction for calculations of the energy gap in two-dimensional materials," *Physical Review B*, vol. 97, no. 4, p. 045426, 2018.

[23] H. Şahin, S. Cahangirov, M. Topsakal, E. Bekaroglu, E. Akturk, R. T. Senger, and S. Ciraci, "Monolayer honeycomb structures of group-iv elements and iii-v binary compounds: First-principles calculations," *Phys. Rev. B*, vol. 80, p. 155453, Oct 2009.

[24] Y. Zhao, X. Wu, J. Yang, and X. C. Zeng, "Oxidation of a two-dimensional hexagonal boron nitride monolayer: a first-principles study," *Phys. Chem. Chem. Phys.*, vol. 14, pp. 5545–5550, 2012.

[25] F. A. Rasmussen, P. S. Schmidt, K. T. Winther, and K. S. Thygesen, "Efficient many-body calculations for two-dimensional materials using exact limits for the screened potential: Band gaps of $\mathbf{mos}_2$, h-bn, and phosphorene," *Phys. Rev. B*, vol. 94, p. 155406, Oct 2016.

[26] V. O. Özçelik, J. G. Azadani, C. Yang, S. J. Koester, and T. Low, "Band alignment of two-dimensional semiconductors for designing heterostructures with momentum space matching," *Phys. Rev. B*, vol. 94, p. 035125, Jul 2016.

[27] R. Sevak Singh, R. Yingjie Tay, W. Leong Chow, S. Hon Tsang, G. Mallick, and E. H. Tong Teo, "Band gap effects of hexagonal boron nitride using oxygen plasma," *Appl. Phys. Lett.*, vol. 104, no. 16, p. 163101, 2014.

[28] K.-H. Xue, J.-H. Yuan, L. R. Fonseca, and X.-S. Miao, "Improved lda-1/2 method for band structure calculations in covalent semiconductors," *Computational Materials Science*, vol. 153, pp. 493–505, 2018.

[29] F. Matusalem, M. Ribeiro, Jr., M. Marques, R. R. Pelá, L. G. Ferreira, and L. K. Teles, "Combined lda and lda-1/2 method to obtain defect formation energies in large silicon supercells," *Phys. Rev. B*, vol. 88, p. 224102, Dec 2013.

[30] F. Matusalem, R. R. Pelá, M. Marques, and L. K. Teles, "Charge transition levels of mn-doped si calculated with the gga-1/2 method," *Phys. Rev. B*, vol. 90, p. 224102, Dec 2014.

[31] B. Lucatto, L. V. C. Assali, R. R. Pelá, M. Marques, and L. K. Teles, "General procedure for the calculation of accurate defect excitation energies from dft-1/2 band structures: The case of the nv^- center in diamond," *Phys. Rev. B*, vol. 96, p. 075145, Aug 2017.

[32] T. T. Tran, K. Bray, M. J. Ford, M. Toth, and I. Aharonovich, "Quantum emission from hexagonal boron nitride monolayers," *Nat. Nanotech.*, vol. 11, no. 1, p. 37, 2016.

[33] T. T. Tran, D. Wang, Z.-Q. Xu, A. Yang, M. Toth, T. W. Odom, and I. Aharonovich, "Deterministic coupling of quantum emitters in 2d materials to plasmonic nanocavity arrays," *Nano Lett.*, vol. 17, no. 4, pp. 2634–2639, 2017.

[34] L. J. Martínez, T. Pelini, V. Waselowski, J. R. Maze, B. Gil, G. Cassabois, and V. Jacques, "Efficient single photon emission from a high-purity hexagonal boron nitride crystal," *Phys. Rev. B*, vol. 94, p. 121405, Sep 2016.

[35] N. R. Jungwirth, B. Calderon, Y. Ji, M. G. Spencer, M. E. Flatté, and G. D. Fuchs, "Temperature dependence of wavelength selectable zero-phonon emission from single defects in hexagonal boron nitride," *Nano Lett.*, vol. 16, no. 10, pp. 6052–6057, 2016.

[36] R. Bourrellier, S. Meuret, A. Tararan, O. Stéphan, M. Kociak, L. H. G. Tizei, and A. Zobelli, "Bright uv single photon emission at point defects in h-bn," *Nano Lett.*, vol. 16, no. 7, pp. 4317–4321, 2016.

[37] C. Attaccalite, M. Bockstedte, A. Marini, A. Rubio, and L. Wirtz, "Coupling of excitons and defect states in boron-nitride nanostructures," *Phys. Rev. B*, vol. 83, p. 144115, Apr 2011.

[38] F. Wu, A. Galatas, R. Sundararaman, D. Rocca, and Y. Ping, "First-principles engineering of charged defects for two-dimensional quantum technologies," *Phys. Rev. Mater.*, vol. 1, no. 7, p. 071001, 2017.

[39] D. S. Fartab and A. A. Kordbacheh, "Lithium doping and vacancy effects on the structural, electronic and magnetic properties of hexagonal boron nitride sheet: A first-principles calculation," *Supperlattice. Microst.*, vol. 118, pp. 185 – 195, 2018.

[40] J. R. Reimers, A. Sajid, R. Kobayashi, and M. J. Ford, "Understanding and calibrating density-functional-theory calculations describing the energy and spectroscopy of defect sites in hexagonal boron nitride," *J. Chem. Theory Comput.*, vol. 14, no. 3, pp. 1602–1613, 2018.

[41] S. Azevedo, J. R. Kaschny, C. M. de Castilho, and F. de Brito Mota, "Electronic structure of defects in a boron nitride monolayer," *Eur Phys. J. B*, vol. 67, pp. 507–512, Feb 2009.

[42] S. K. Gupta, H. He, D. Banyai, M. Si, R. Pandey, and S. P. Karna, "Effect of si doping on the electronic properties of bn monolayer," *Nanoscale*, vol. 6, pp. 5526–5531, 2014.

[43] R. Wang, J. Yang, X. Wu, and S. Wang, "Local charge states in hexagonal boron nitride with stone–wales defects," *Nanoscale*, vol. 8, pp. 8210–8219, 2016.

[44] S. K. Gupta, H. He, I. Lukačević, and R. Pandey, "Spin-dependent electron transport in c and ge doped bn monolayers," *Phys. Chem. Chem. Phys.*, vol. 19, pp. 30370–30380, 2017.

[45] M. Dantas, B. de Lima Bernardo, and S. Azevedo, "First-principle calculations on the effect of impurities on different stacking of h-bn bilayers," *Appl. Phys. A*, vol. 119, pp. 697–705, May 2015.

[46] H. Kökten and Ş. Erkoç, "A study on si and p doped h-bn sheets: Dft calculations," *Turk. J. Phys.*, vol. 38, no. 3, pp. 369–374, 2014.

[47] D. Xu, Y.-j. Liu, J.-x. Zhao, Q.-h. Cai, and X.-z. Wang, "Theoretical study of the deposition of pt clusters on defective hexagonal boron nitride (h-bn) sheets: Morphologies, electronic structures, and interactions with o," *J. Phys. Chem. C*, vol. 118, no. 17, pp. 8868–8876, 2014.

[48] Y.-D. Guo, H.-F. Liu, H.-L. Zeng, X.-H. Yan, and X.-C. Song, "Edge defect switched dual spin filter in zigzag hexagonal boron nitride nanoribbons," *Phys. Chem. Chem. Phys.*, vol. 20, pp. 9241–9247, 2018.

[49] R. E. Mapasha, M. P. Molepo, R. C. Andrew, and N. Chetty, "Defect charge states in si doped hexagonal boron-nitride monolayer," *J. Phys.: Condens. Matter*, vol. 28, no. 5, p. 055501, 2016.

[50] J. H. Los, J. M. H. Kroes, K. Albe, R. M. Gordillo, M. I. Katsnelson, and A. Fasolino, "Extended tersoff potential for boron nitride: Energetics and elastic properties of pristine and defective *h*-bn," *Phys. Rev. B*, vol. 96, p. 184108, Nov 2017.

[51] S. Ma, "Bandgap modulation and hydrogen storage with cr-doped bn sheets," *Int. J. Mod. Phys. B*, vol. 29, no. 22, p. 1550160, 2015.

[52] M. Abdi, J.-P. Chou, A. Gali, and M. B. Plenio, "Color centers in hexagonal boron nitride monolayers: A group theory and ab initio analysis," *ACS Photonics*, vol. 5, no. 5, pp. 1967–1976, 2018.

[53] H.-P. Komsa, N. Berseneva, A. V. Krasheninnikov, and R. M. Nieminen, "Charged point defects in the flatland: Accurate formation energy calculations in two-dimensional materials," *Phys. Rev. X*, vol. 4, no. 3, p. 031044, 2014.

[54] A. M. Ukpong and N. Chetty, "First principles molecular dynamics study of nitrogen vacancy complexes in boronitrene," *J. Phys.: Condens. Matter*, vol. 24, no. 26, p. 265002, 2012.

[55] L.-S. Zhao, C.-P. Chen, L.-L. Liu, H.-X. Yu, Y. Chen, and X.-C. Wang, "Magnetism and piezoelectricity of hexagonal boron nitride with triangular vacancy," *Chin. Phys. B*, vol. 27, no. 1, p. 016301, 2018.

[56] D.-H. Kim, H.-S. Kim, M. W. Song, S. Lee, and S. Y. Lee, "Geometric and electronic structures of monolayer hexagonal boron nitride with multivacancy," *Nano Converg.*, vol. 4, no. 1, p. 13, 2017.

[57] H. Zhang, G. Yu, W. Chen, J. Guan, and X. Huang, "A first-principles investigation on the effect of the divacancy defect on the band structures of boron nitride (bn) nanoribbons," *Physica E*, vol. 69, pp. 65–74, 2015.

[58] W. Amalia, P. Nurwantoro, *et al.*, "Density-functional-theory calculations of structural and electronic properties of vacancies in monolayer hexagonal boron nitride (h-bn)," *Comput. Condens. Matter*, vol. 18, p. e00354, 2019.

[59] S. A. Tawfik, S. Ali, M. Fronzi, M. Kianinia, T. T. Tran, C. Stampfl, I. Aharonovich, M. Toth, and M. J. Ford, "First-principles investigation of quantum emission from hbn defects," *Nanoscale*, vol. 9, no. 36, pp. 13575–13582, 2017.

[60] X. Li, G. D. Shepard, A. Cupo, N. Camporeale, K. Shayan, Y. Luo, V. Meunier, and S. Strauf, "Nonmagnetic quantum emitters in boron nitride with ultranarrow and sideband-free emission spectra," *ACS nano*, vol. 11, no. 7, pp. 6652–6660, 2017.

[61] L. Weston, D. Wickramaratne, M. Mackoit, A. Alkauskas, and C. G. Van de Walle, "Native point defects and impurities in hexagonal boron nitride," *Phys. Rev. B*, vol. 97, p. 214104, Jun 2018.

[62] T. J. Smart, F. Wu, M. Govoni, and Y. Ping, "Fundamental principles for calculating charged defect ionization energies in ultrathin two-dimensional materials," *Phys. Rev. Materials*, vol. 2, p. 124002, Dec 2018.

[63] A. Sajid, J. R. Reimers, and M. J. Ford, "Defect states in hexagonal boron nitride: Assignments of observed properties and prediction of properties relevant to quantum computation," *Phys. Rev. B*, vol. 97, p. 064101, Feb 2018.

[64] S. Manzeli, D. Ovchinnikov, D. Pasquier, O. V. Yazyev, and A. Kis, "2d transition metal dichalcogenides," *Nature Reviews Materials*, vol. 2, no. 8, p. 17033, 2017.

[65] A. Splendiani, L. Sun, Y. Zhang, T. Li, J. Kim, C.-Y. Chim, G. Galli, and F. Wang, "Emerging photoluminescence in monolayer mos_2," *Nano letters*, vol. 10, no. 4, pp. 1271–1275, 2010.

[66] B. Radisavljevic, A. Radenovic, J. Brivio, V. Giacometti, and A. Kis, "Single-layer mos_2 transistors," *Nature nanotechnology*, vol. 6, no. 3, pp. 147–150, 2011.

[67] C. Lee, H. Yan, L. E. Brus, T. F. Heinz, J. Hone, and S. Ryu, "Anomalous lattice vibrations of single-and few-layer mos_2," *ACS nano*, vol. 4, no. 5, pp. 2695–2700, 2010.

[68] O. Lopez-Sanchez, D. Lembke, M. Kayci, A. Radenovic, and A. Kis, "Ultrasensitive photodetectors based on monolayer mos_2," *Nature nanotechnology*, vol. 8, no. 7, pp. 497–501, 2013.

[69] W. Wu, L. Wang, Y. Li, F. Zhang, L. Lin, S. Niu, D. Chenet, X. Zhang, Y. Hao, T. F. Heinz, *et al.*, "Piezoelectricity of single-atomic-layer mos_2 for energy conversion and piezotronics," *Nature*, vol. 514, no. 7523, pp. 470–474, 2014.

[70] K. F. Mak, K. L. McGill, J. Park, and P. L. McEuen, "The valley hall effect in mos_2 transistors," *Science*, vol. 344, no. 6191, pp. 1489–1492, 2014.

[71] X. Xu, W. Yao, D. Xiao, and T. F. Heinz, "Spin and pseudospins in layered transition metal dichalcogenides," *Nature Physics*, vol. 10, no. 5, pp. 343–350, 2014.

[72] L. Zhang, Z. Yang, T. Gong, R. Pan, H. Wang, Z. Guo, H. Zhang, and X. Fu, "Recent advances in emerging janus two-dimensional materials: from fundamental physics to device applications," *J. Mater. Chem. A*, vol. 8, pp. 8813–8830, 2020.

[73] Y. Wei, X. Tang, J. Shang, L. Ju, and L. Kou, "Two-dimensional functional materials: from properties to potential applications," *International Journal of Smart and Nano Materials*, vol. 11, no. 3, pp. 247–264, 2020.

[74] A.-Y. Lu, H. Zhu, J. Xiao, C.-P. Chuu, Y. Han, M.-H. Chiu, C.-C. Cheng, C.-W. Yang, K.-H. Wei, Y. Yang, Y. Wang, D. Sokaras, D. Nordlund, P. Yang, D. A. Muller, M.-Y. Chou, X. Zhang, and L.-J. Li, "Janus monolayers of transition metal dichalcogenides," *Nature Nanotechnology*, vol. 12, pp. 744–749, Aug 2017.

[75] J. Zhang, S. Jia, I. Kholmanov, L. Dong, D. Er, W. Chen, H. Guo, Z. Jin, V. B. Shenoy, L. Shi, and J. Lou, "Janus monolayer transition-metal dichalcogenides," *ACS Nano*, vol. 11, no. 8, pp. 8192–8198, 2017. PMID: 28771310.

[76] M. Yagmurcukardes, C. Sevik, and F. M. Peeters, "Electronic, vibrational, elastic, and piezoelectric properties of monolayer janus moste phases: A first-principles study," *Phys. Rev. B*, vol. 100, p. 045415, Jul 2019.

[77] D. B. Trivedi, G. Turgut, Y. Qin, M. Y. Sayyad, D. Hajra, M. Howell, L. Liu, S. Yang, N. H. Patoary, H. Li, M. M. Petrić, M. Meyer, M. Kremser, M. Barbone, G. Soavi, A. V. Stier, K. Müller, S. Yang, I. S. Esqueda, H. Zhuang, J. J. Finley, and S. Tongay, "Room-temperature synthesis of 2d janus crystals and their heterostructures," *Advanced Materials*, vol. 32, no. 50, p. 2006320, 2020.

[78] H. Li, Y. Qin, B. Ko, D. B. Trivedi, D. Hajra, M. Y. Sayyad, L. Liu, S.-H. Shim, H. Zhuang, and S. Tongay, "Anomalous behavior of 2d janus excitonic layers under extreme pressures," *Advanced Materials*, vol. 32, no. 33, p. 2002401, 2020.

[79] M. M. Petrić, M. Kremser, M. Barbone, Y. Qin, Y. Sayyad, Y. Shen, S. Tongay, J. J. Finley, A. R. Botello-Méndez, and K. Müller, "Raman spectrum of janus transition metal dichalcogenide monolayers wsse and mosse," *Phys. Rev. B*, vol. 103, p. 035414, Jan 2021.

[80] B. Javvaji, B. He, X. Zhuang, and H. S. Park, "High flexoelectric constants in janus transition-metal dichalcogenides," *Phys. Rev. Materials*, vol. 3, p. 125402, Dec 2019.

[81] H. Cai, Y. Guo, H. Gao, and W. Guo, "Tribo-piezoelectricity in janus transition metal dichalcogenide bilayers: A first-principles study," *Nano Energy*, vol. 56, pp. 33 – 39, 2019.

[82] R. Chaurasiya, S. Tyagi, N. Singh, S. Auluck, and A. Dixit, "Enhancing thermoelectric properties of janus wsse monolayer by inducing strain mediated valley degeneracy," *Journal of Alloys and Compounds*, vol. 855, p. 157304, 2021.

[83] B. Hou, Y. Zhang, H. Zhang, H. Shao, C. Ma, X. Zhang, Y. Chen, K. Xu, G. Ni, and H. Zhu, "Room temperature bound excitons and strain-tunable carrier mobilities in janus monolayer transition-metal dichalcogenides," *The Journal of Physical Chemistry Letters*, vol. 11, no. 8, pp. 3116–3128, 2020. PMID: 32220211.

[84] S.-D. Guo, "Phonon transport in janus monolayer mosse: a first-principles study," *Phys. Chem. Chem. Phys.*, vol. 20, pp. 7236–7242, 2018.

[85] F. Li, W. Wei, B. Huang, and Y. Dai, "Excited-state properties of janus transition-metal dichalcogenides," *The Journal of Physical Chemistry C*, vol. 124, no. 2, pp. 1667–1673, 2020.

[86] M. Idrees, H. U. Din, R. Ali, G. Rehman, T. Hussain, C. V. Nguyen, I. Ahmad, and B. Amin, "Optoelectronic and solar cell applications of janus monolayers and their van der waals heterostructures," *Phys. Chem. Chem. Phys.*, vol. 21, pp. 18612–18621, 2019.

[87] M. K. Mohanta and A. De Sarkar, "Interfacial hybridization of janus mosse and bx (x= p, as) monolayers for ultrathin excitonic solar cells, nanopiezotronics and low-power memory devices," *Nanoscale*, vol. 12, no. 44, pp. 22645–22657, 2020.

[88] S. Kaur, A. Kumar, S. Srivastava, K. Tankeshwar, and R. Pandey, "Monolayer, bilayer, and heterostructures of green phosphorene for water splitting and photovoltaics," *The Journal of Physical Chemistry C*, vol. 122, no. 45, pp. 26032–26038, 2018.

[89] M. K. Mohanta, A. Rawat, N. Jena, Dimple, R. Ahammed, and A. De Sarkar, "Interfacing boron monophosphide with molybdenum disulfide for an ultrahigh performance in thermoelectrics, two-dimensional excitonic solar cells, and nanopiezotronics," *ACS Applied Materials & Interfaces*, vol. 12, no. 2, pp. 3114–3126, 2020. PMID: 31904214.

[90] J. Zhang, X. Lang, Y. Zhu, and Q. Jiang, "Strain tuned inse/mos 2 bilayer van der waals heterostructures for photovoltaics or photocatalysis," *Physical Chemistry Chemical Physics*, vol. 20, no. 26, pp. 17574–17582, 2018.

[91] Y. Ji, M. Yang, H. Lin, T. Hou, L. Wang, Y. Li, and S.-T. Lee, "Janus structures of transition metal dichalcogenides as the heterojunction photocatalysts for water splitting," *The Journal of Physical Chemistry C*, vol. 122, no. 5, pp. 3123–3129, 2018.

[92] J. Wang, H. Shu, T. Zhao, P. Liang, N. Wang, D. Cao, and X. Chen, "Intriguing electronic and optical properties of two-dimensional janus transition metal dichalcogenides," *Phys. Chem. Chem. Phys.*, vol. 20, pp. 18571–18578, 2018.

[93] A. Rawat, M. K. Mohanta, N. Jena, Dimple, R. Ahammed, and A. De Sarkar, "Nanoscale interfaces of janus monolayers of transition metal

dichalcogenides for 2d photovoltaic and piezoelectric applications," *The Journal of Physical Chemistry C*, vol. 124, no. 19, pp. 10385–10397, 2020.

[94] Y. Xu, Y. Yao, W. Yin, J. Cao, M. Chen, and X. Wei, "Intrinsic defect engineered janus mosse sheet as a promising photocatalyst for water splitting," *RSC Adv.*, vol. 10, pp. 10816–10825, 2020.

[95] X. Ma, X. Wu, H. Wang, and Y. Wang, "A janus mosse monolayer: a potential wide solar-spectrum water-splitting photocatalyst with a low carrier recombination rate," *J. Mater. Chem. A*, vol. 6, pp. 2295–2301, 2018.

[96] L. Ju, M. Bie, X. Tang, J. Shang, and L. Kou, "Janus wsse monolayer: An excellent photocatalyst for overall water splitting," *ACS Applied Materials & Interfaces*, vol. 12, no. 26, pp. 29335–29343, 2020. PMID: 32519846.

[97] Y. Sun, Z. Shuai, and D. Wang, "Janus monolayer of wsete, a new structural phase transition material driven by electrostatic gating," *Nanoscale*, vol. 10, pp. 21629–21633, 2018.

[98] C. Long, Y. Dai, Z.-R. Gong, and H. Jin, "Robust type-ii band alignment in janus-mosse bilayer with extremely long carrier lifetime induced by the intrinsic electric field," *Phys. Rev. B*, vol. 99, p. 115316, Mar 2019.

[99] Y. Ding, G. Yang, Y. Gu, Y. Yu, X. Zhang, X. Tang, N. Lu, Y. Wang, Z. Dai, H. Zhao, and Y. Li, "First-principles predictions of janus mosse and wsse for fet applications," *The Journal of Physical Chemistry C*, vol. 124, no. 38, pp. 21197–21206, 2020.

[100] R. Chaurasiya and A. Dixit, "Defect engineered mosse janus monolayer as a promising two dimensional material for no2 and no gas sensing," *Applied Surface Science*, vol. 490, pp. 204 – 219, 2019.

[101] D. Wang, T. Lan, J. Pan, Z. Liu, A. Yang, M. Yang, J. Chu, H. Yuan, X. Wang, Y. Li, and M. Rong, "Janus mosse monolayer: A highly strain-sensitive gas sensing material to detect sf6 decompositions," *Sensors and Actuators A: Physical*, vol. 311, p. 112049, 2020.

[102] X.-Y. Yang, T. Hussain, J. P. A. Wärnå, Z. Xu, and R. Ahuja, "Exploring janus mosse monolayer as a workable media for sof_6 decompositions sensing based on dft calculations," *Computational Materials Science*, vol. 186, p. 109976, 2021.

[103] R. Chaurasiya and A. Dixit, "Ultrahigh sensitivity with excellent recovery time for nh3 and no2 in pristine and defect mediated janus wsse monolayers," *Phys. Chem. Chem. Phys.*, vol. 22, pp. 13903–13922, 2020.

[104] N. Jena, Dimple, R. Ahammed, A. Rawat, M. K. Mohanta, and A. De Sarkar, "Valley drift and valley current modulation in strained monolayer Mos_2," *Phys. Rev. B*, vol. 100, p. 165413, Oct 2019.

[105] Y. Ma, L. Kou, A. Du, B. Huang, Y. Dai, and T. Heine, "Conduction-band valley spin splitting in single-layer h-Tl_2O," *Phys. Rev. B*, vol. 97, p. 035444, Jan 2018.

[106] M. K. Mohanta and A. De Sarkar, "Coupled spin and valley polarization in monolayer Hfn_2 and valley-contrasting physics at the $Hfn_2 - WSe_2$ interface," *Phys. Rev. B*, vol. 102, p. 125414, Sep 2020.

[107] H. Zeng, J. Dai, W. Yao, D. Xiao, and X. Cui, "Valley polarization in mos_2 monolayers by optical pumping," *Nature nanotechnology*, vol. 7, no. 8, pp. 490–493, 2012.

[108] K. F. Mak, K. He, J. Shan, and T. F. Heinz, "Control of valley polarization in monolayer mos_2 by optical helicity," *Nature nanotechnology*, vol. 7, no. 8, pp. 494–498, 2012.

[109] T. Cao, G. Wang, W. Han, H. Ye, C. Zhu, J. Shi, Q. Niu, P. Tan, E. Wang, B. Liu, and J. Feng, "Valley-selective circular dichroism of monolayer molybdenum disulphide," *Nature Communications*, vol. 3, p. 887, Jun 2012.

[110] G. Sallen, L. Bouet, X. Marie, G. Wang, C. Zhu, W. Han, Y. Lu, P. Tan, T. Amand, B. Liu, *et al.*, "Robust optical emission polarization in mos_2 monolayers through selective valley excitation," *Physical Review B*, vol. 86, no. 8, p. 081301, 2012.

[111] A. Srivastava, M. Sidler, A. V. Allain, D. S. Lembke, A. Kis, and A. Imamoğlu, "Valley zeeman effect in elementary optical excitations of monolayer wse_2," *Nature Physics*, vol. 11, pp. 141–147, Feb 2015.

[112] G. Aivazian, Z. Gong, A. M. Jones, R.-L. Chu, J. Yan, D. G. Mandrus, C. Zhang, D. Cobden, W. Yao, and X. Xu, "Magnetic control of valley pseudospin in monolayer wse_2," *Nature Physics*, vol. 11, no. 2, pp. 148–152, 2015.

[113] S. Aas and C. Bulutay, "Geometric band properties in strained monolayer transition metal dichalcogenides using simple band structures," *Journal of Applied Physics*, vol. 126, no. 11, p. 115701, 2019.

[114] P. Sengupta, D. Pavlidis, and J. Shi, "Optically adjustable valley hall current in single-layer transition metal dichalcogenides," *Journal of Applied Physics*, vol. 123, no. 5, p. 054301, 2018.

[115] L. Tong, X. Duan, L. Song, T. Liu, L. Ye, X. Huang, P. Wang, Y. Sun, X. He, L. Zhang, K. Xu, W. Hu, J.-B. Xu, J. Zang, and G. J. Cheng, "Artificial control of in-plane anisotropic photoelectricity in monolayer mos_2," *Applied Materials Today*, vol. 15, pp. 203 – 211, 2019.

[116] G. Kresse and J. Furthmüller, "Efficiency of ab-initio total energy calculations for metals and semiconductors using a plane-wave basis set," *Comput. Mater. Sci.*, vol. 6, no. 1, pp. 15–50, 1996.

[117] G. Kresse and D. Joubert, "From ultrasoft pseudopotentials to the projector augmented-wave method," *Phys. Rev. B*, vol. 59, pp. 1758–1775, Jan 1999.

[118] L. C. L. Y. Voon and M. Willatzen, *The k.p method: electronic properties of semiconductors*. Springer Science & Business Media, 2009.

[119] A. Kormányos, V. Zólyomi, N. D. Drummond, P. Rakyta, G. Burkard, and V. I. Fal'ko, "Monolayer mos_2: Trigonal warping, the Γ valley, and spin-orbit coupling effects," *Phys. Rev. B*, vol. 88, p. 045416, Jul 2013.

[120] A. Kormányos, G. Burkard, M. Gmitra, J. Fabian, V. Zólyomi, N. D. Drummond, and V. Fal'ko, "k· p theory for two-dimensional transition metal

dichalcogenide semiconductors," *2D Materials*, vol. 2, no. 2, p. 022001, 2015.

[121] H. Rostami, R. Roldán, E. Cappelluti, R. Asgari, and F. Guinea, "Theory of strain in single-layer transition metal dichalcogenides," *Phys. Rev. B*, vol. 92, p. 195402, 2015.

[122] D. V. Rybkovskiy, I. C.Gerber, and M. V. Durnev, "Atomically inspired k· p approach and valley zeeman effect in transition metal dichalcogenide monolayers," *Phys. Rev. B*, vol. 95, p. 155406, 2017.

[123] S. Fang, S. Carr, M. A. Cazalilla, and E. Kaxiras, "Electronic structure theory of strained two-dimensional materials with hexagonal symmetry," *Phys. Rev. B*, vol. 98, p. 075106, Aug 2018.

[124] R. Roldán, A. Castellanos-Gomez, E. Cappelluti, and F. Guinea, "Strain engineering in semiconducting two-dimensional crystals," *Journal of Physics: Condensed Matter*, vol. 27, p. 313201, jul 2015.

[125] Y. Peter and M. Cardona, *Fundamentals of semiconductors: physics and materials properties*. Berlin and Heidelberg: Springer, 2010.

[126] M. Cardona and F. H. Pollak, "Energy-band structure of germanium and silicon: The k· p method," *Physical Review*, vol. 142, no. 2, p. 530, 1966.

[127] C. Bulutay, "Pseudopotential-based full zone k.p technique for indirect bandgap semiconductors: Si, ge, diamond and sic," *Turkish Journal of Physics*, vol. 30, no. 4, pp. 287–294, 2006.

[128] J. P. Perdew and Y. Wang, "Accurate and simple analytic representation of the electron-gas correlation energy," *Physical review B*, vol. 45, no. 23, p. 13244, 1992.

[129] V. O. Özçelik, J. G. Azadani, C. Yang, S. J. Koester, and T. Low, "Band alignment of two-dimensional semiconductors for designing heterostructures with momentum space matching," *Phys. Rev. B*, vol. 94, p. 035125, Jul 2016.

[130] H. Şahin, S. Cahangirov, M. Topsakal, E. Bekaroglu, E. Akturk, R. T. Senger, and S. Ciraci, "Monolayer honeycomb structures of group-iv elements and iii-v binary compounds: First-principles calculations," *Phys. Rev. B*, vol. 80, p. 155453, Oct 2009.

[131] M. S. Prete, A. Mosca Conte, P. Gori, F. Bechstedt, and O. Pulci, "Tunable electronic properties of two-dimensional nitrides for light harvesting heterostructures," *Applied Physics Letters*, vol. 110, no. 1, p. 012103, 2017.

[132] B. Huang and H. Lee, "Defect and impurity properties of hexagonal boron nitride: A first-principles calculation," *Phys. Rev. B*, vol. 86, p. 245406, Dec 2012.

[133] P. Scherpelz and G. Galli, "Optimizing surface defects for atomic-scale electronics: Si dangling bonds," *Phys. Rev. Materials*, vol. 1, p. 021602, Jul 2017.

[134] D. Xiao, G.-B. Liu, W. Feng, X. Xu, and W. Yao, "Coupled spin and valley physics in monolayers of mos_2 and other group-vi dichalcogenides," *Phys. Rev. Lett.*, vol. 108, p. 196802, May 2012.

[135] S. Wang, M. S. Ukhtary, and R. Saito, "Strain effect on circularly polarized electroluminescence in transition metal dichalcogenides," *Phys. Rev. Research*, vol. 2, p. 033340, Aug 2020.

[136] V. V. Thanh, N. D. Van, D. V. Truong, R. Saito, and N. T. Hung, "First-principles study of mechanical, electronic and optical properties of janus structure in transition metal dichalcogenides," *Applied Surface Science*, vol. 526, p. 146730, 2020.

[137] S.-D. Guo and J. Dong, "Biaxial strain tuned electronic structures and power factor in janus transition metal dichalchogenide monolayers," *Semiconductor Science and Technology*, vol. 33, p. 085003, jul 2018.

[138] W. Shi and Z. Wang, "Mechanical and electronic properties of janus monolayer transition metal dichalcogenides," *Journal of Physics: Condensed Matter*, vol. 30, p. 215301, may 2018.

[139] Z. Wang, "2h $\rightarrow$ 1' phase transformation in janus monolayer mosse and moste: an efficient hole injection contact for 2h-mos_2," *J. Mater. Chem. C*, vol. 6, pp. 13000–13005, 2018.

[140] C. Xia, W. Xiong, J. Du, T. Wang, Y. Peng, and J. Li, "Universality of electronic characteristics and photocatalyst applications in the two-dimensional janus transition metal dichalcogenides," *Phys. Rev. B*, vol. 98, p. 165424, Oct 2018.

[141] H. Rostami, K. Volckaert, N. Lanata, S. K. Mahatha, C. E. Sanders, M. Bianchi, D. Lizzit, L. Bignardi, S. Lizzit, J. A. Miwa, A. V. Balatsky, P. Hofmann, and S. Ulstrup, "Layer and orbital interference effects in photoemission from transition metal dichalcogenides," *Phys. Rev. B*, vol. 100, p. 235423, Dec 2019.

[142] D. Rai, A. Laref, M. Khuili, S. Al-Qaisi, T. V. Vu, and D. D. Vo, "Electronic, magnetic and optical properties of monolayer (ml) hexagonal znse on vacancy defects at zn sites from dft-1/2 approach," *Vacuum*, vol. 182, p. 109597, 2020.

[143] B. Tang, J. Zhou, P. Sun, X. Wang, L. Bai, J. Dan, J. Yang, K. Zhou, X. Zhao, S. J. Pennycook, *et al.*, "Phase-controlled synthesis of monolayer ternary telluride with a random local displacement of tellurium atoms," *Advanced Materials*, vol. 31, no. 23, p. 1900862, 2019.

Appendix A

h-BN Defects with DFT and DFT-1/2

A.1 Computational Details

The VASP code [116] is used to perform all DFT calculations where LDA and PBE functionals are already implemented. After relaxing the pristine and defective structures with PBE and LDA, PBE-1/2 and LDA-1/2 calculations are done over these. The conceptual basis of DFT-1/2 can be explained as modifying the self-energy potential with a trim function while 1/2 electron is stripped. Here, the self-energy potential is defined with the difference of neutral atom and half-ionized KS eigenstates and the trim function is introduced with a value called CUT that disables the Coulomb like potential to diverge or penetrate with nearby atom potentials [12, 22]. CUT parameter is determined by maximizing the band gap and it depends on the type of the atom. In Figure 2.1, we have found $2.5\,a_0$ is the suitable CUT value of h-BN where a_0 is the Bohr radius and 1/2 electron is removed from p orbital of the nitrogen atom.

CUT value is recommended to be applied only for the self-energy potential of anion. This is efficient enough to maximize the gap and it is proven for various materials [12, 16]. For C atom, strong hole localization is observed for 2D and

bulk [28] systems. In order to achieve a better correction, additional to N, 1/4 electrons are removed from s and p orbitals of C atoms with a CUT value of $2.10\,a_0$.[28]

The energy cutoff for these systems assigned as 500 eV. The valence and core states are computed by using the projector augemented wave (PAW) method [117]. $8 \times 8 \times 1$ **k**-point sampling of Brillouin zone for Monkhorst-Pack scheme is used. To enable monolayer structure of h-BN, vacuum spacing of 15 Å is chosen between layers. For the main calculations, $6 \times 6 \times 1$ supercell is chosen for h-BN monolayer. $10 \times 10 \times 1$ supercell calculations are added in order to accomplish a comparison over small and large supercell results for defective systems.

A.2 Tables For Defect Energies For Small and Large Supercells

Tables A.1-A.4 show spin polarized defect energy states for 6×6×1 and 10×10×1 supercells. High symmetry points of CBM and VBM have changed as the supercell is extended but considering the folding of the crystal structure, both symmetry points in different supercells are equivalent. For large supercells, Γ-point high symmetry point is chosen to measure the defect energies while it is K-point for the small ones. Small supercells create a dispersion in defect states which are close to VBM or CBM and this situation is fixed when the supercell size is expanded. Since the dispersion of defect states is flat, it should not depend on which symmetry point the energy is measured.

Defect	*LDA (6×6×1)*	*LDA (10×10×1)*
C_B	0↑, 0.51↓	0↑, 0.52↓
C_N	0↑, 0.52↓	0↑, 0.54↓
V_B	-0.01↑↑, 0.79↓↓	0.08↑↑, 0.80↓↓
V_N	0↑, 0.23↑↑, 0.34↓, 0.26↓↓	0↑, 1.82↑, 1.95↑, 0.35↓, 1.82↓, 2.04↓
DV	-1.08↑↓, 0↑↓, 3.17↑↓, 4.01↑↓	-0.92↑↓, 0↑↓, 3.65↑↓, 4.24↑↓, 4.77↑↓
SW	-0.76↑↓, 0↑↓, 3.43↑↓	-

Table A.1: Spin polarized defect states calculated with LDA for small and large supercells where energies are aligned from HOMO level.

Defect	*LDA-1/2 (6×6×1)*	*LDA-1/2 (10×10×1)*
C_B	0↑, 0.77↓	0↑, 0.78↓
C_N	0↑, 0.83↓	0↑, 0.84↓
V_B	-0.24↑↑, 1.16↓↓	-0.19↑↑, 1.21↓↓
V_N	0↑, 1.90↑↑, 0.44↓, 1.95↓↓	0↑, 1.87↑↑, 0.44↓, 2.16↓↓
DV	-0.03↑↓, 0↑↓, 3.96↑↓, 4.71↑↓	-0.11↑↓, 0↑↓, 3.79↑↓, 4.80↑↓, 5.97↑↓
SW	-0.04↑↓, 0↑↓, 4.78↑↓	-

Table A.2: Spin polarized defect states calculated with LDA-1/2 for small and large supercells where energies are aligned from HOMO level.

A.3 Electronic Band Structures with PBE and PBE-1/2

Electronic band structures along with density of states (DOS) are presented for C_B, C_N, V_B, V_N, DV and SW in Figures A.1-A.6. For carbon impurities, it can be noted that while VB and CB consist of p orbitals of B and N atoms, respectively. This causes the C_B defect state to appear near VB in Figure A.1 and for C_N it is shifted to CB in Figure A.2. Considering this situation, a similar observation can be made for V_N in Figure A.3 and V_B in Figure A.4. It is no

Defect	***PBE (6×6×1)***	***PBE (10×10×1)***
C_B	0↑, 0.87↓	0↑, 0.89↓
C_N	0↑, 0.90↓	0↑, 0.95↓
V_B	-0.21↑↑, 1.51↓↓	-0.23↑↑, 1.51↓↓
V_N	0↑, 1.93↑↑, 0.65↓, 1.84↓↓	0↑, 1.89↑↑, 0.65↓, 2.13↓, 2.18↓
DV	-1.08↑↓, 0↑↓, 3.25↑↓, 3.41↑↓	-0.95↑↓, 0↑↓, 3.25↑↓, 3.40↑↓, 3.55↑↓
SW	-0.83↑↓, 0↑↓, 3.49↑↓	-

Table A.3: Spin polarized defect states calculated with PBE for small and large supercells where energies are aligned from HOMO level.

Defect	***PBE-1/2 (6×6×1)***	***PBE-1/2 (10×10×1)***
C_B	0↑, 1.35↓	0↑, 1.36↓
C_N	0↑, 1.40↓	0↑, 1.41↓
V_B	-0.56↑↑, 1.25↓↓	-0.71↑↑, 1.25↓↓
V_N	0↑, 1.79↑↑, 2.49↑↑ 0.83↓, 2.17↓↓	0↑, 1.76↑↑, 2.36↑↑ 0.83↓, 2.14↓↓
DV	-0.03↑↓, 0↑↓, 3.40↑↓, 4.88↑↓	-0.06↑↓, 0↑↓, 3.14↑↓, 4.95↑↓, 6.20↑↓
SW	-0.15↑↓, 0↑↓, 4.97↑↓	-

Table A.4: Spin polarized defect states calculated with PBE-1/2 for small and large supercells where energies are aligned from HOMO level.

surprise that DV and SW in Figures A.5,A.6 have their defects states spread where some of them are close to VB and others to CB.

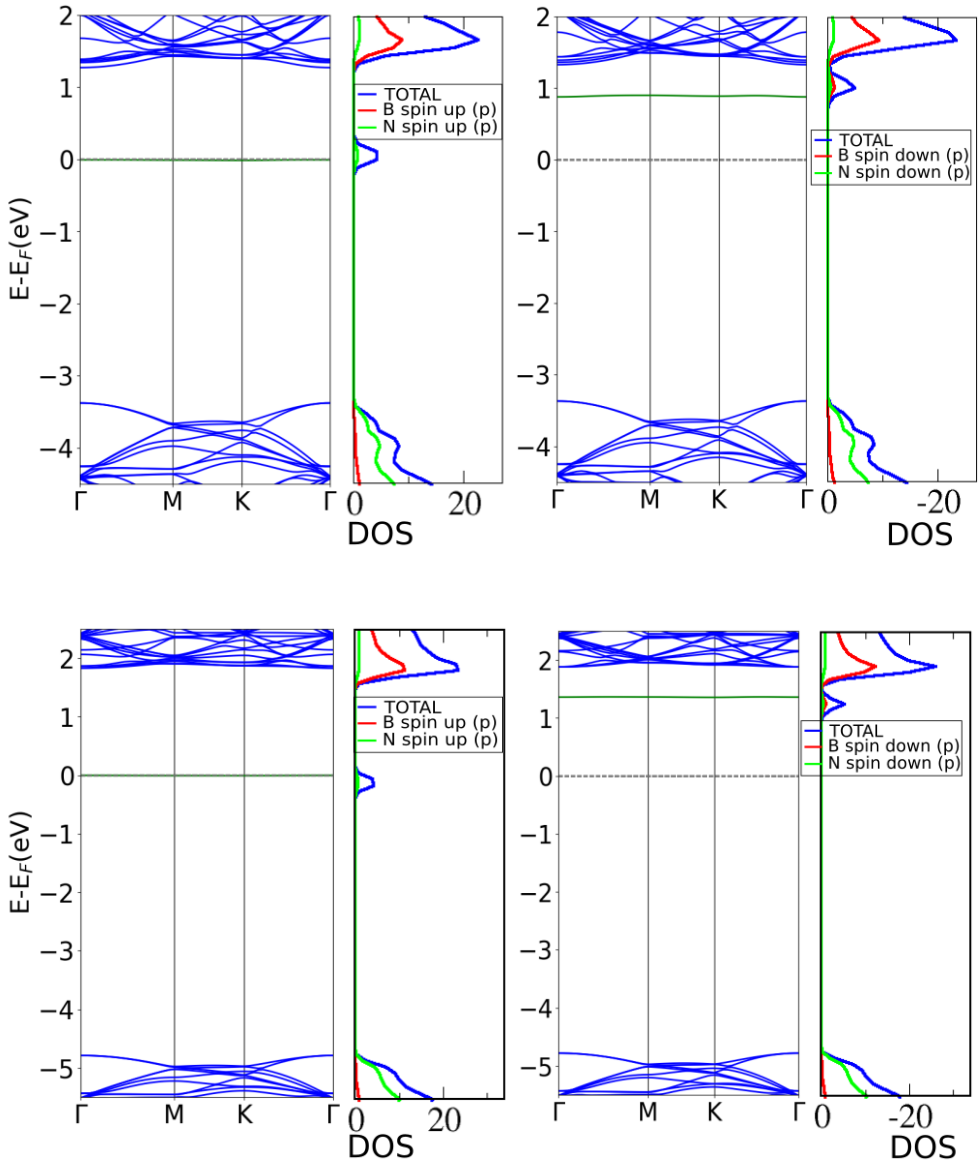


Figure A.1: Band structure and DOS for C_B defect spin up (left) and spin down (right) calculated with (a) PBE and (b) PBE-1/2.

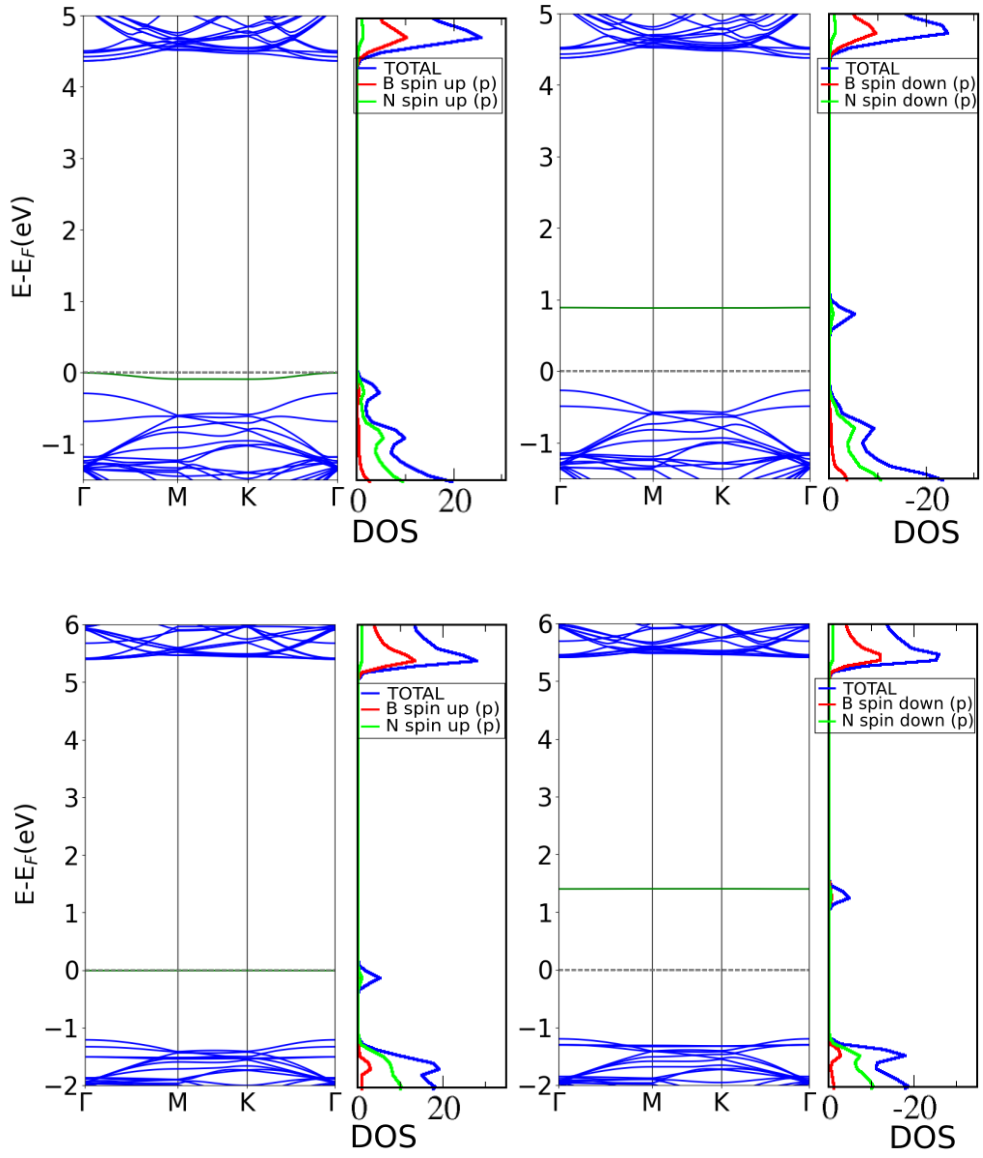


Figure A.2: Band structure and DOS for C_N defect spin up (left) and spin down (right) calculated with (a) PBE and (b) PBE-1/2.

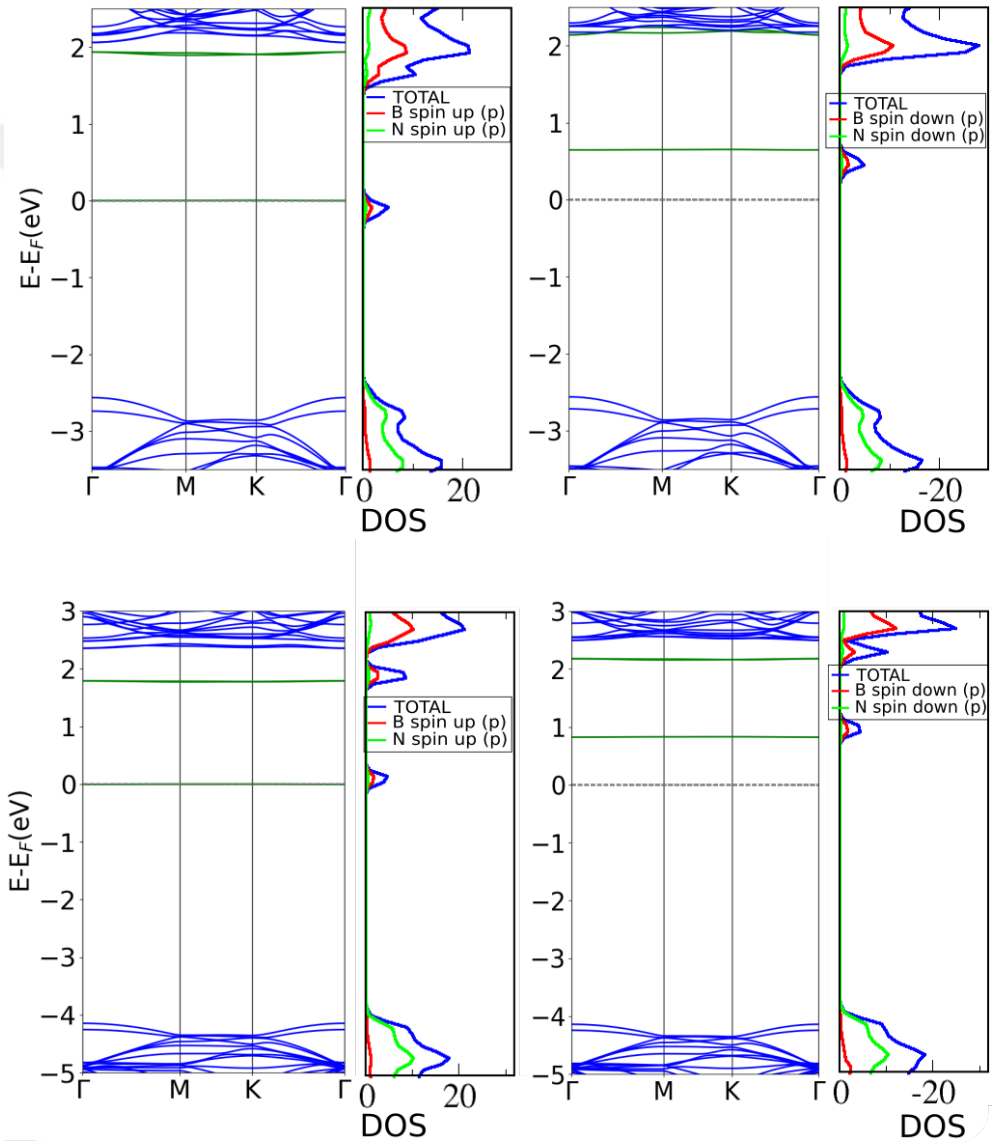


Figure A.3: Band structure and DOS for V_N defect spin up (left) and spin down (right) calculated with (a) PBE and (b) PBE-1/2.

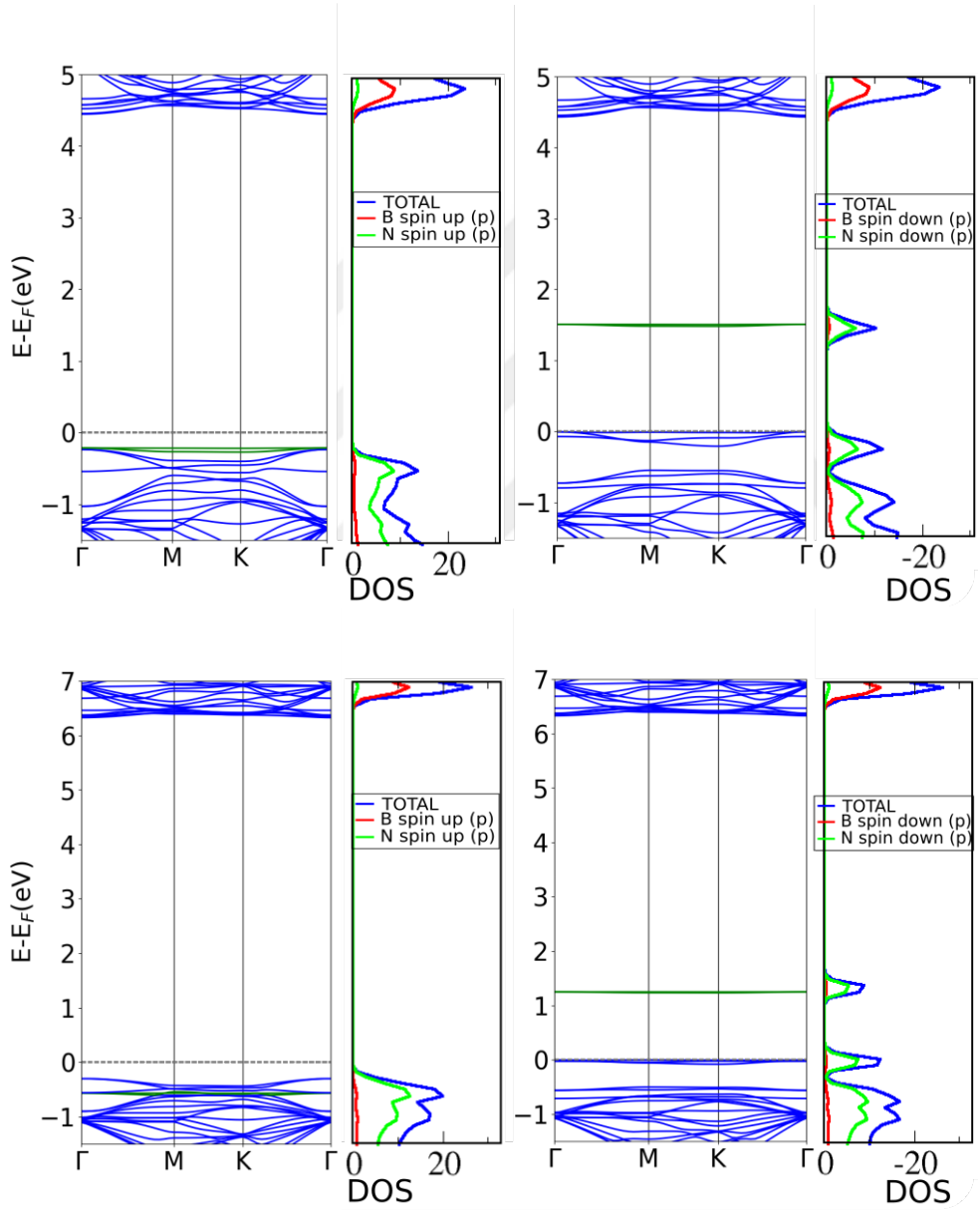


Figure A.4: Band structure and DOS for V_B defect spin up (left) and spin down (right) calculated with (a) PBE and (b) PBE-1/2.

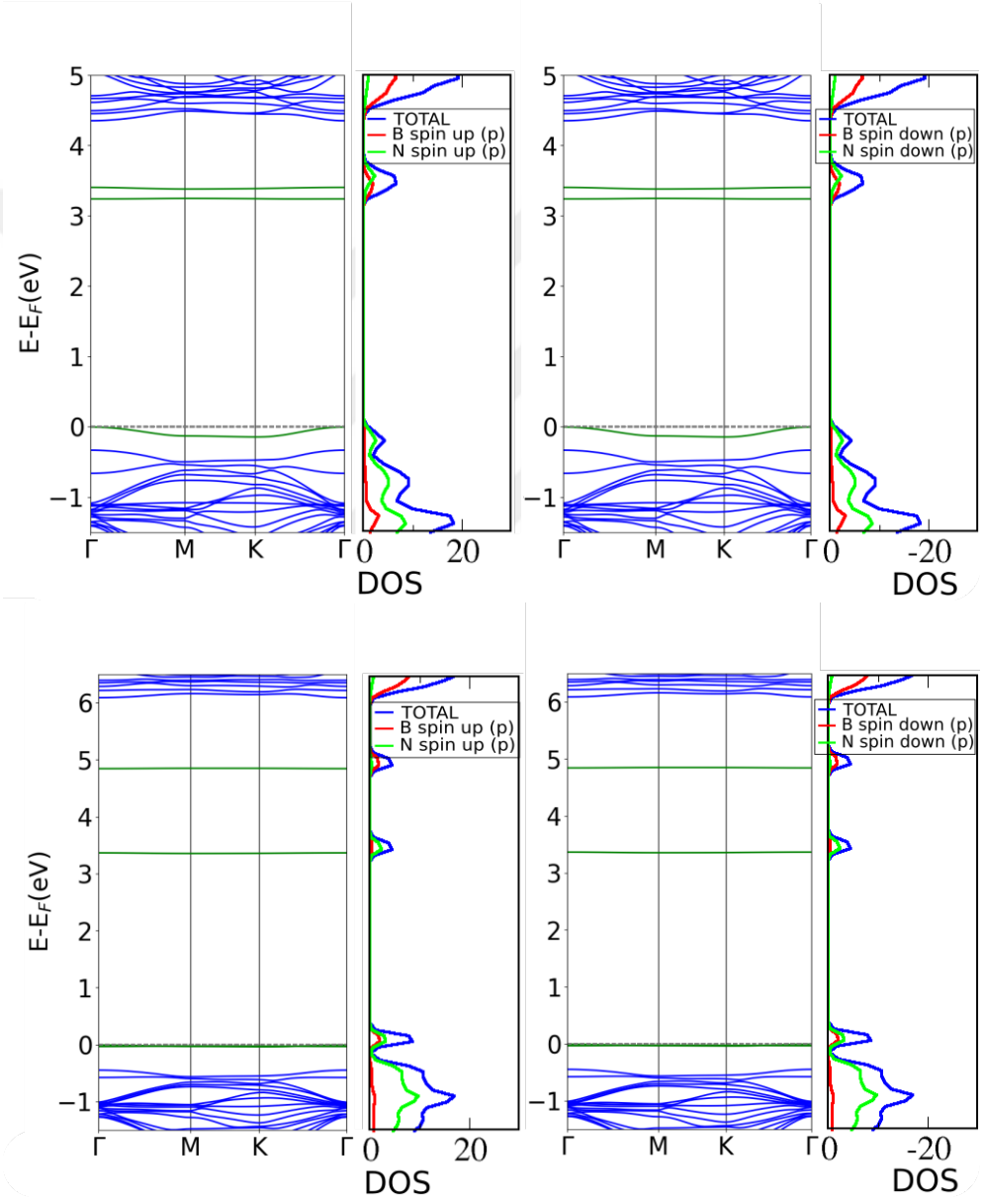


Figure A.5: Band structure and DOS for DV defect spin up (left) and spin down (right) calculated with (a) PBE and (b) PBE-1/2.

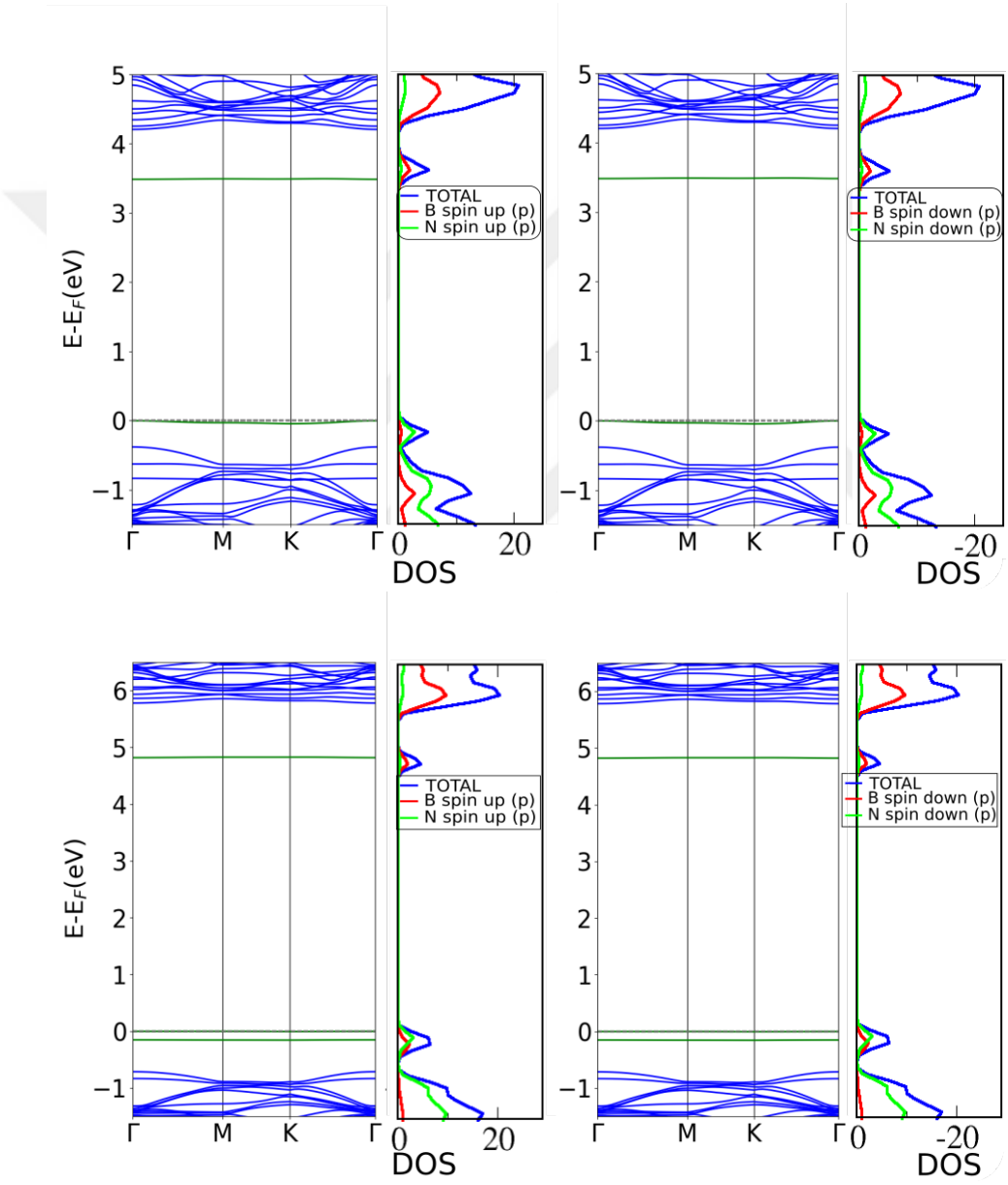


Figure A.6: Band structure and DOS for SW defect spin up (left) and spin down (right) calculated with (a) PBE and (b) PBE-1/2.

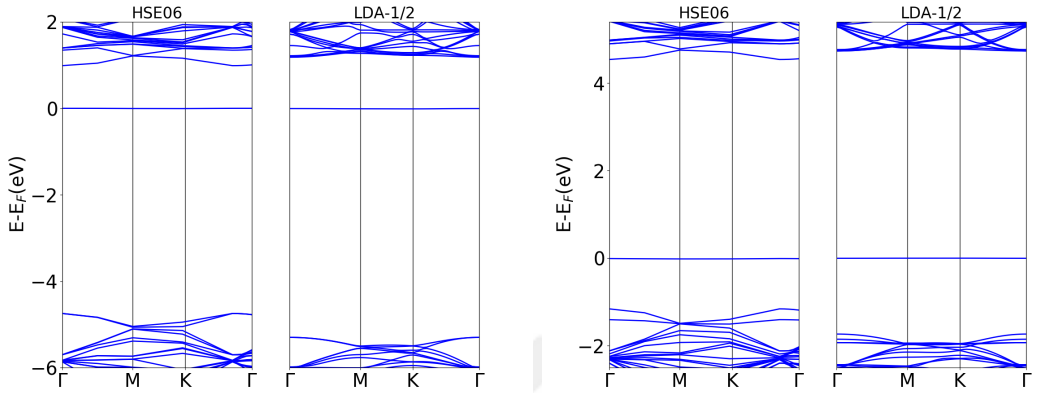


Figure A.7: HSE06 and LDA-1/2 electronic band structure for C_B (left) and C_N (right) defects.

A.4 Electronic Band Structures with HSE and LDA-1/2

Here, we have calculated the electronic band structure of C_B, C_N, V_B, V_N, DV and SW defects using LDA-1/2 and improved these results with HSE06 later. However, considering the computational budget this supercell size, we were only able to calculate spinless systems. In Figures A.7-A.9, 0 eV is considered for the Fermi level. According to these results, without any additional cost to DFT, LDA-1/2 is more successful over increasing the band gap compared to HSE. Figure A.7 shows that HSE and LDA-1/2 band structures are very close to each other with 0.5 eV difference in the band gap. While for V_N defect LDA-1/2 is outstanding with revealing two degenerate defect states around CB, for V_B both methods are good enough to identify similar states around VB in Figure A.8. Additionally, for DV and SW defects, LDA-1/2 is more powerful to bring the hidden defect states in VB out while keeping their double degenerate nature, compared to HSE.

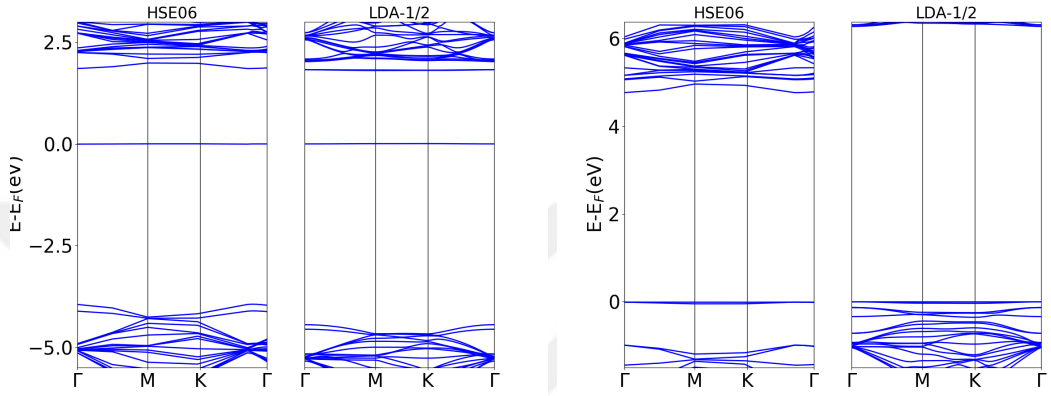


Figure A.8: HSE06 and LDA-1/2 electronic band structure for V_N (left) and V_B (right) defects.

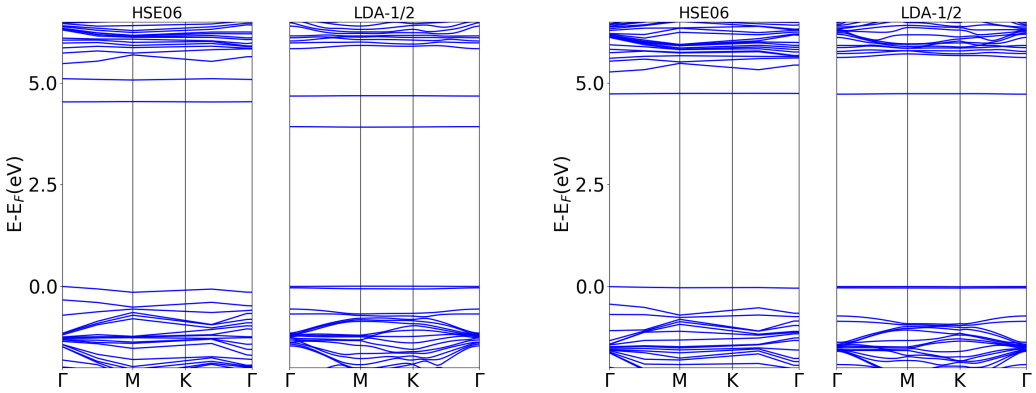


Figure A.9: HSE06 and LDA-1/2 electronic band structure for DV (left) and SW (right) defects.

A.5 Additional Electronic Band Structures of C_N defect

For situations like the calculation of pristine h-BN or single/double vacancies, only applying CUT parameter to anion is adequate for DFT-1/2 technique. However, as exemplified for bulk C [28], strong localization of C requires a special treatment for C_N defect. For this matter, the band structures are plotted for C_N using PBE-1/2 and LDA-1/2 in Figure A.10 where both C and N atoms are subjected to CUT parameter application. When compared with only N correction is presented in Figure A.11, we get the same results with only some small displacements in defect energy levels are seen.

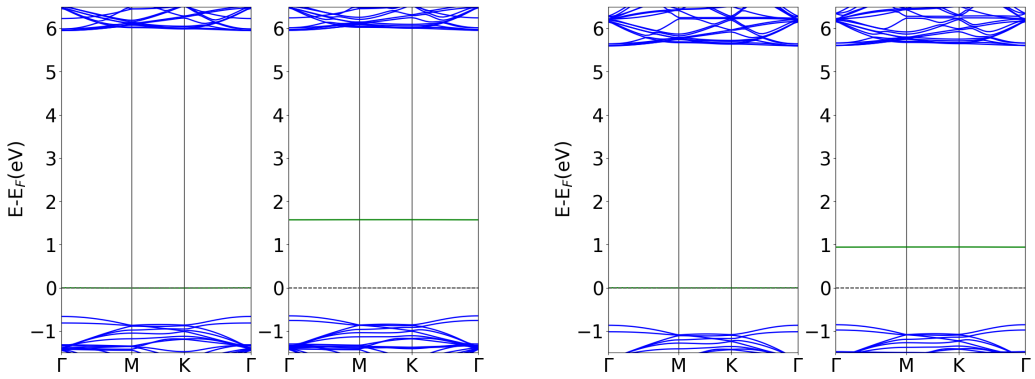


Figure A.10: PBE-1/2 (left) and LDA-1/2 (right) C_N spin polarized band structures of with C and N correction.

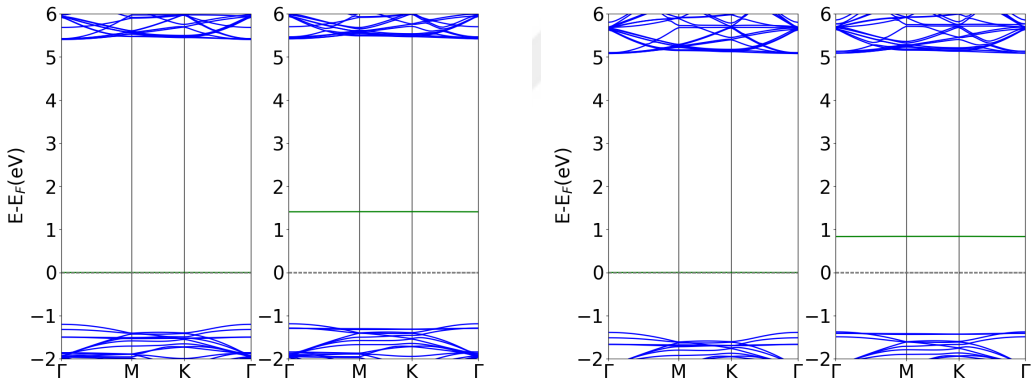


Figure A.11: PBE-1/2 (left) and LDA-1/2 (right) C_N spin polarized band structures of with only N correction.

Appendix B

(Janus) Transition Metal Dichalcogenides with $\mathbf{k} \cdot \mathbf{p}$ Method

B.1 Computational Details

VASP [116] simulation package is used for DFT part of the calculations. As the exchange correlation functional PBE [7] is chosen as a form of GGA. PAW [117] potentials are used. HSE [10] calculations over PBE are performed in order to compare the band gap of semiconductor with the experimental results since using only PBE calculations gives underestimated band gap values. Spin-orbit coupling (SOC) is added to PBE and HSE calculations by considering reported [108] strong spin-orbit interaction in TMDs. 500 eV cutoff energy is preferred which gives results sufficient enough to compare with the band structures obtained by $\mathbf{k} \cdot \mathbf{p}$ parameters. Using Monkhorst-Pack scheme k-point sampling of the Brillouin zone is chosen 36×36×1 and 15×15×1 for PBE and HSE. $\times 10^{-7}$ and 0.0001 eVÅ^{-1} convergence values are ensured for total energy and ionic forces. In Figure 3.3, high symmetry points in reciprocal space for hexagonal and tetragonal crystals and atomic structure of (J)TMDs are illustrated.

B.2 DFT Results w/o SOC for TMDs

Figure B.1 demonstrates the electronic band structure of six TMDs MoS_2, $MoSe_2$, $MoTe_2$, WS_2, WSe_2 and WTe_2 using PBE and PBE with spin-orbit coupling addition. According to these graphs, all the presented TMDs have direct band gap for both PBE and PBE+SOC cases. The band gap values are given at Table 3.1.

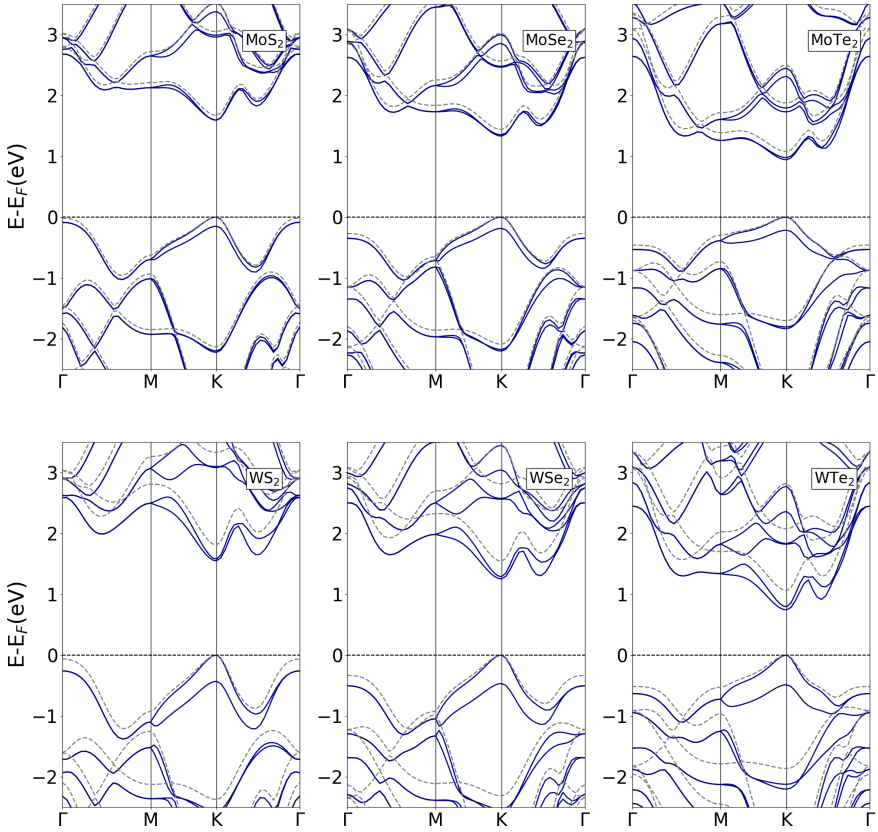


Figure B.1: The electronic band structures calculated with PBE(gray dashed lines) and PBE+SOC (dark blue solid lines) for MX_2 and WX_2.

B.3 DFT Results Under Strain

The electronic band structure of (J)TMDs calculated by PBE under biaxial and uniaxial strain (along x axis) shown in Figures B.2-B.9.

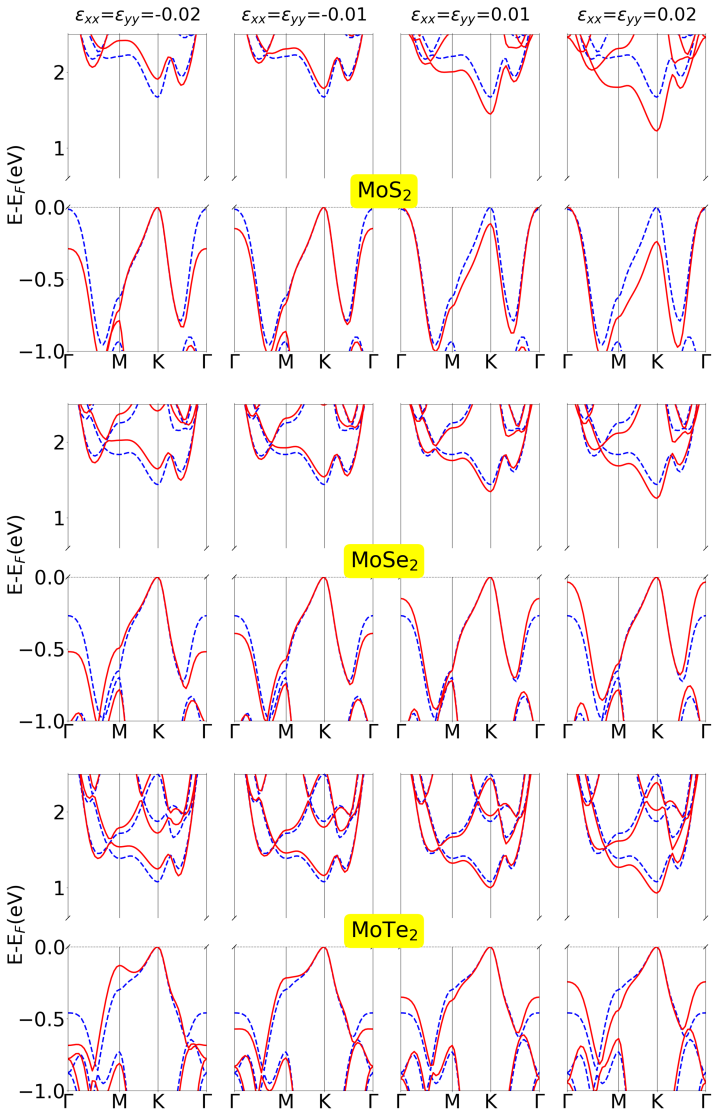


Figure B.2: MoS_2, $MoSe_2$, $MoTe_2$ band structures under -2%,-1%,1%,2% biaxial strain vs without strain.

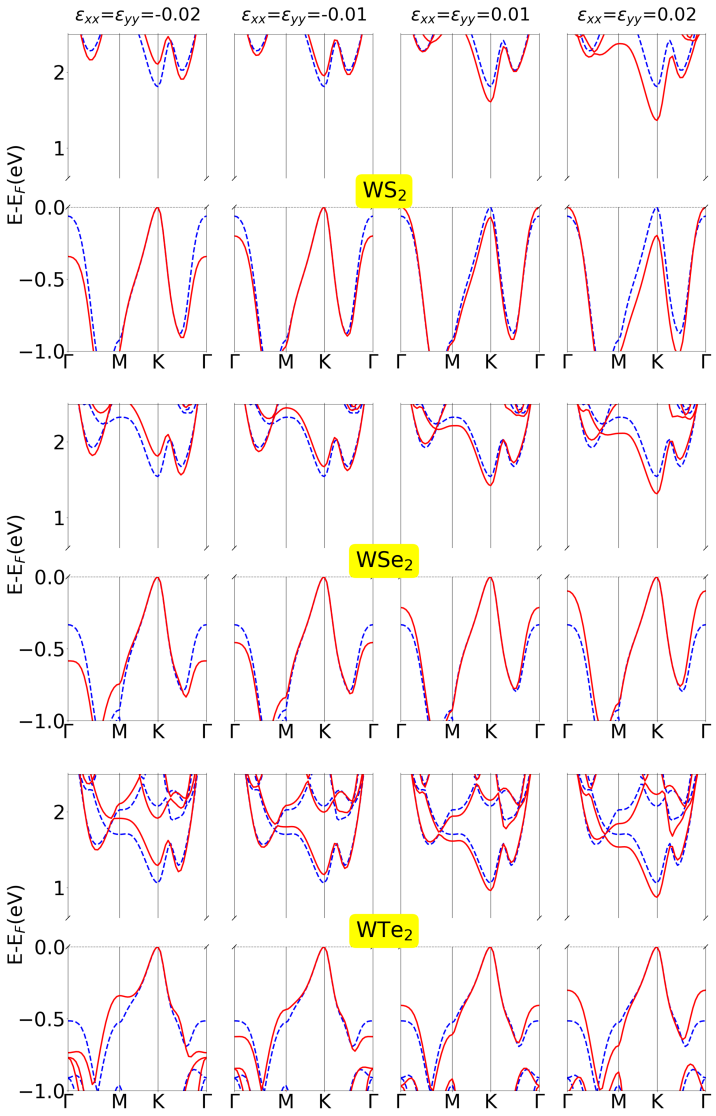


Figure B.3: WS_2, WSe_2, WTe_2 with -2%,-1%,1%,2% band structures under -2%,-1%,1%,2% biaxial strain vs without strain.

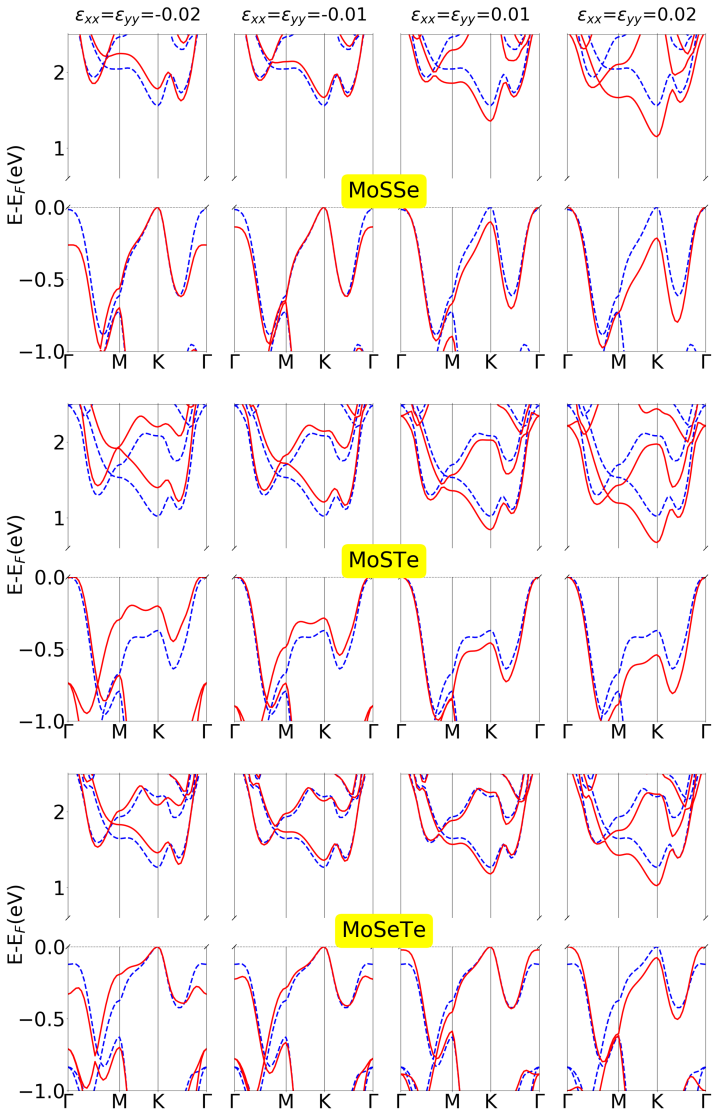


Figure B.4: MoSSe, MoSTe, MoSeTe band structures under -2%,-1%,1%,2% biaxial strain vs without strain.

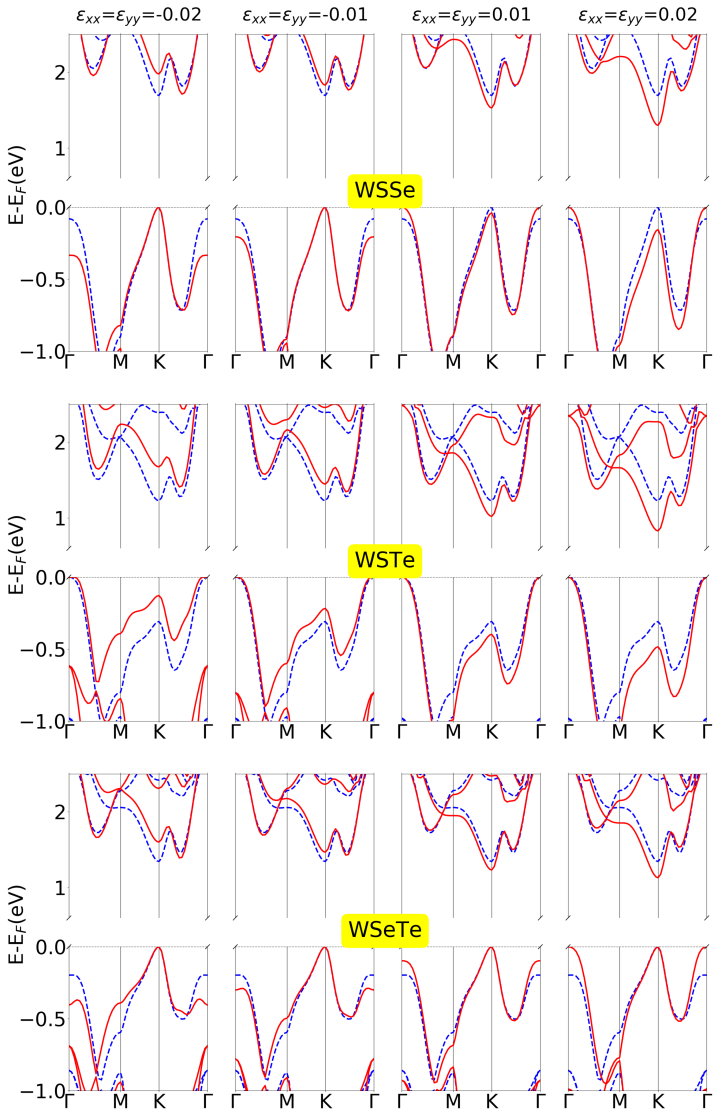


Figure B.5: WSSe, WSTe, WSeTe band structures under -2%,-1%,1%,2% biaxial strain vs without strain.

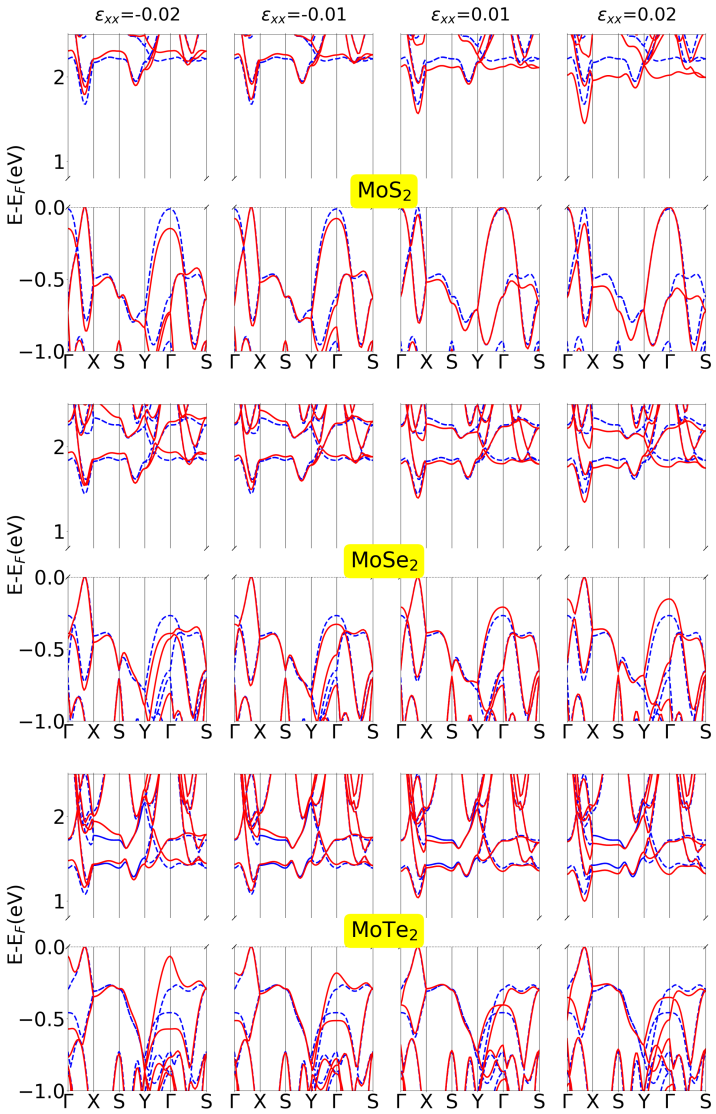


Figure B.6: MoS_2, $MoSe_2$, $MoTe_2$ band structures under -2%,-1%,1%,2% uniaxial strain vs without strain.

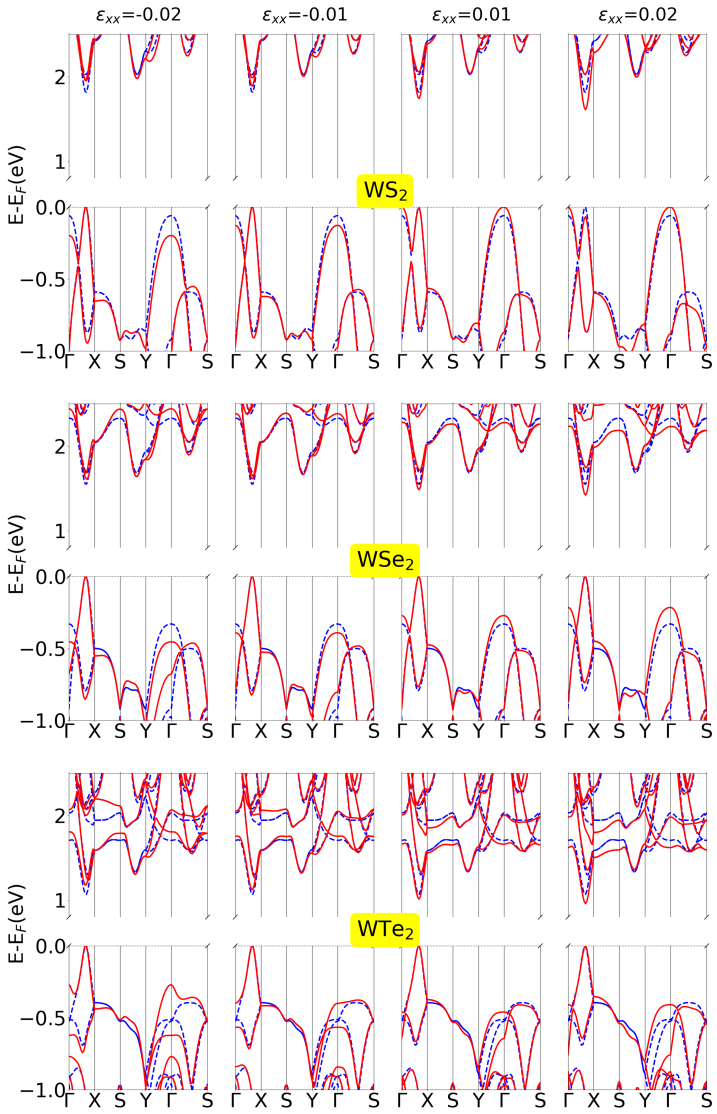


Figure B.7: Band graphs of WS_2, WSe_2, WTe_2 band structures under -2%,-1%,1%,2% uniaxial strain vs without strain.

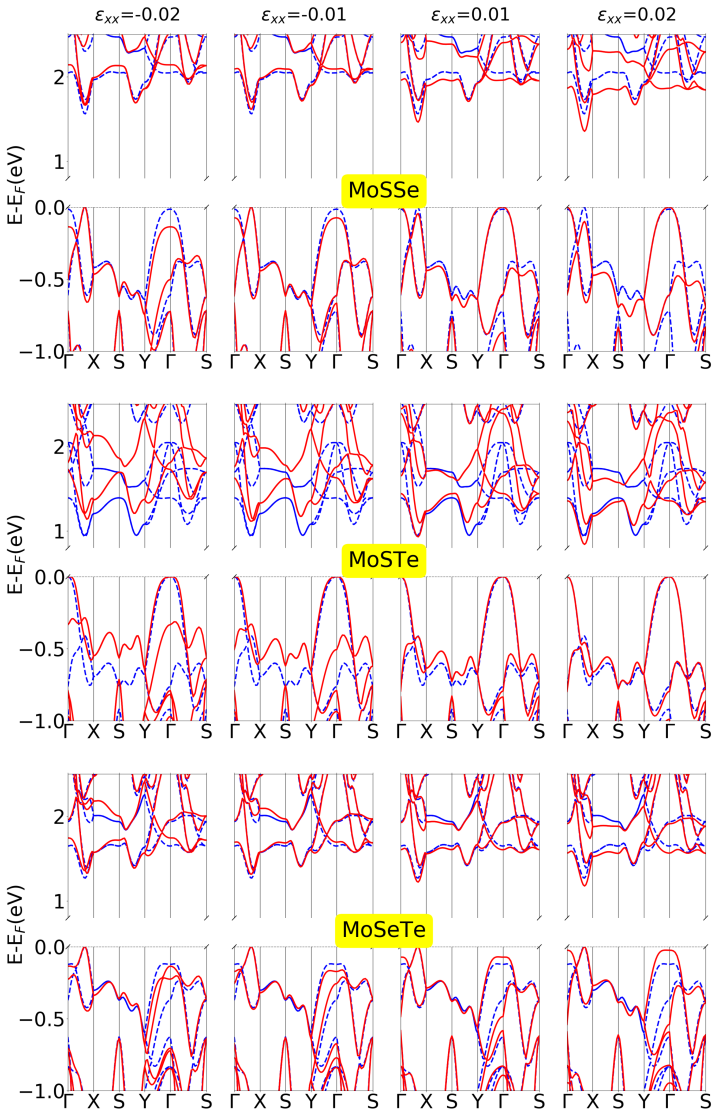


Figure B.8: Band graphs of MoSSe, MoSTe, MoSeTe band structures under -2%,-1%,1%,2% uniaxial strain vs without strain.

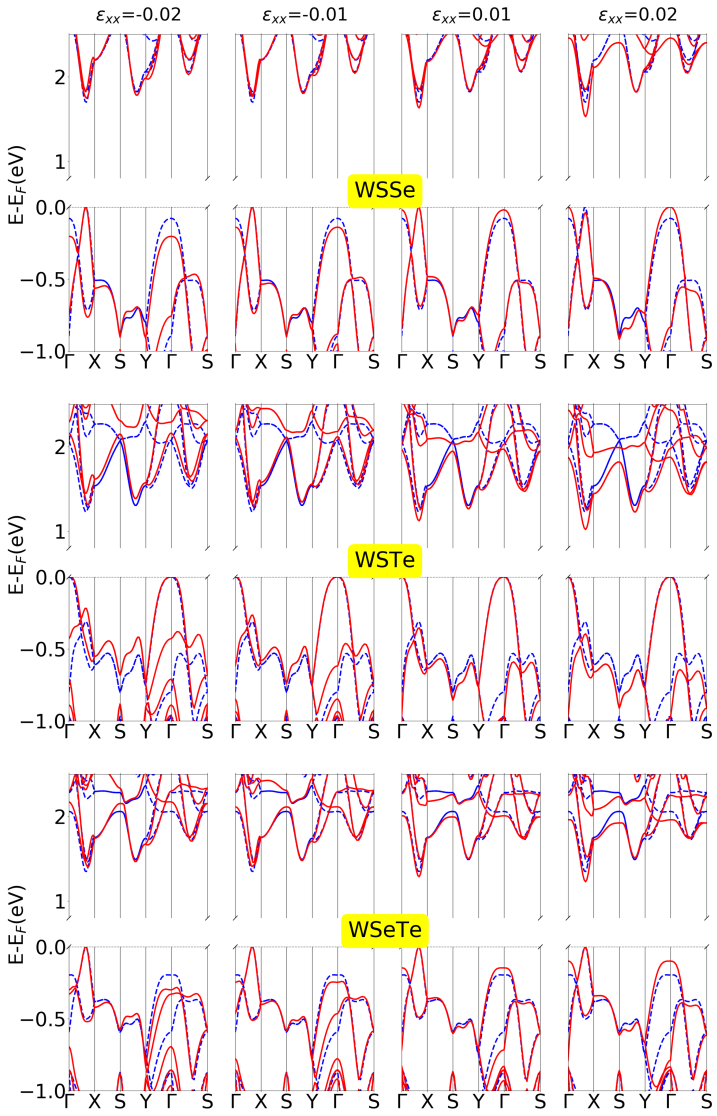


Figure B.9: Band graphs of WSSe, WSTe, WSeTe band structures under -2%,-1%,1%,2% uniaxial strain vs without strain.

B.4 $\mathbf{k}\cdot\mathbf{p}$ vs DFT Spinless Results for MX_2 and MXX'

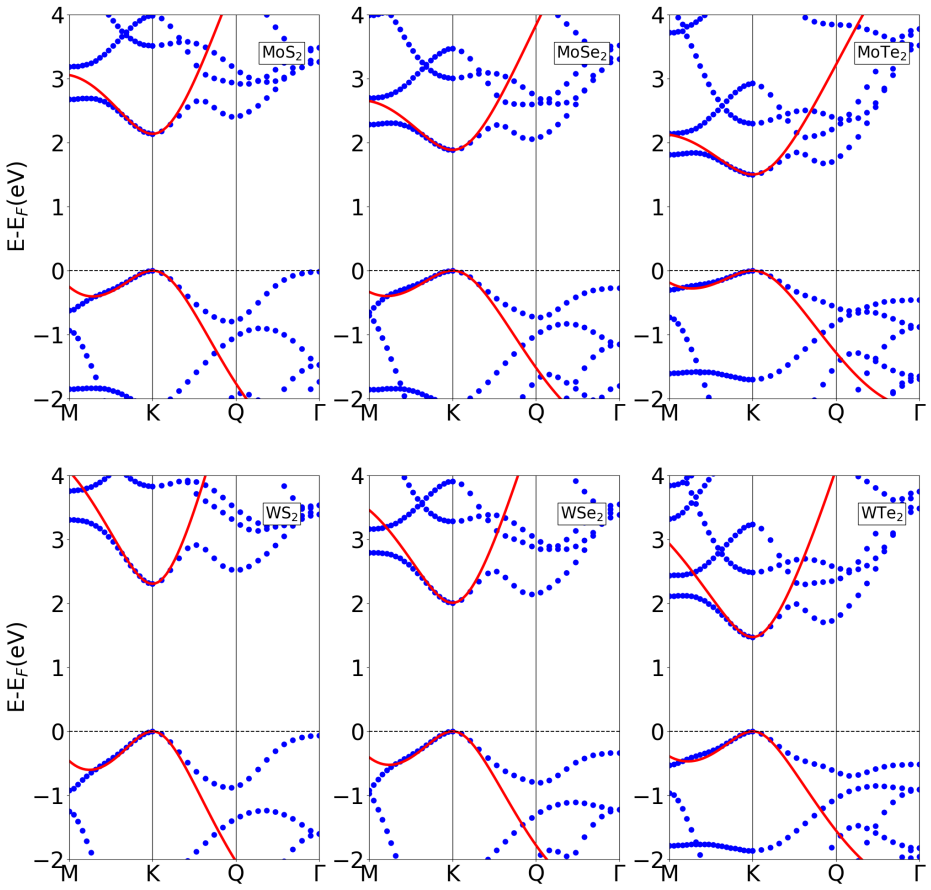


Figure B.10: MoX_2 and WX_2 spinless band structures with $\mathbf{k}\cdot\mathbf{p}$ (solid lines) vs DFT(•).

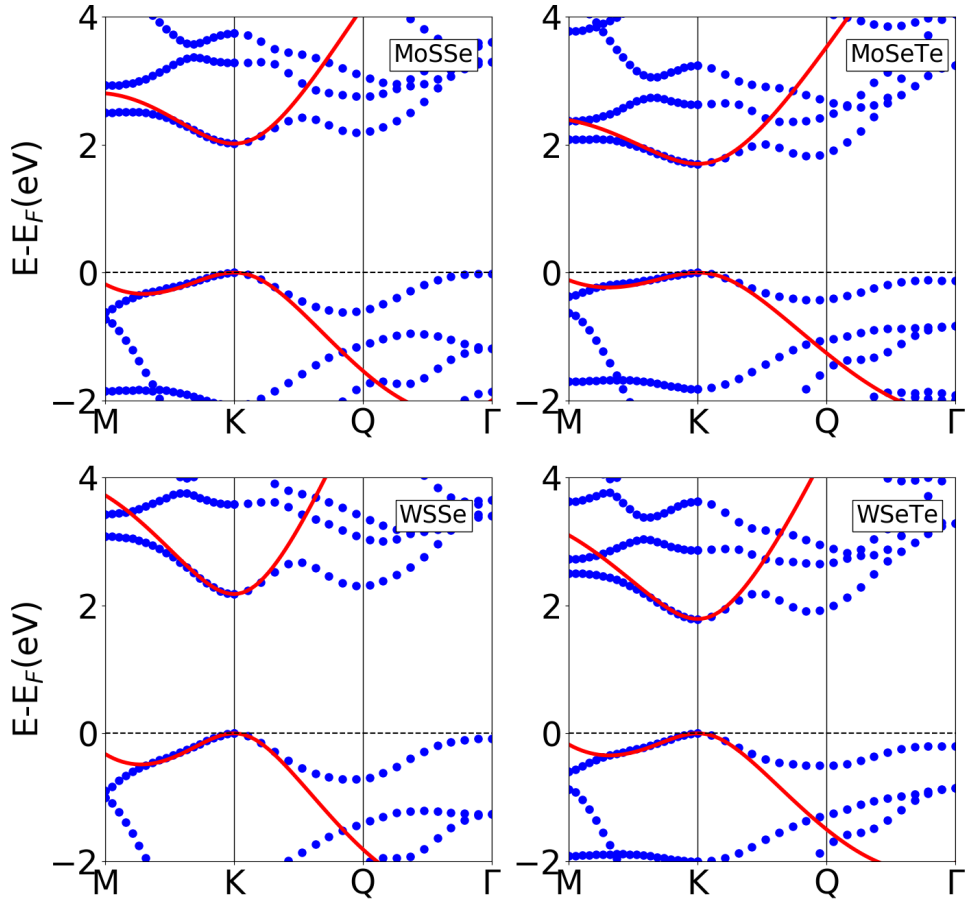


Figure B.11: MoXX′ and WXX′ spinless band structures with $\mathbf{k} \cdot \mathbf{p}$ (solid lines) vs DFT(•).

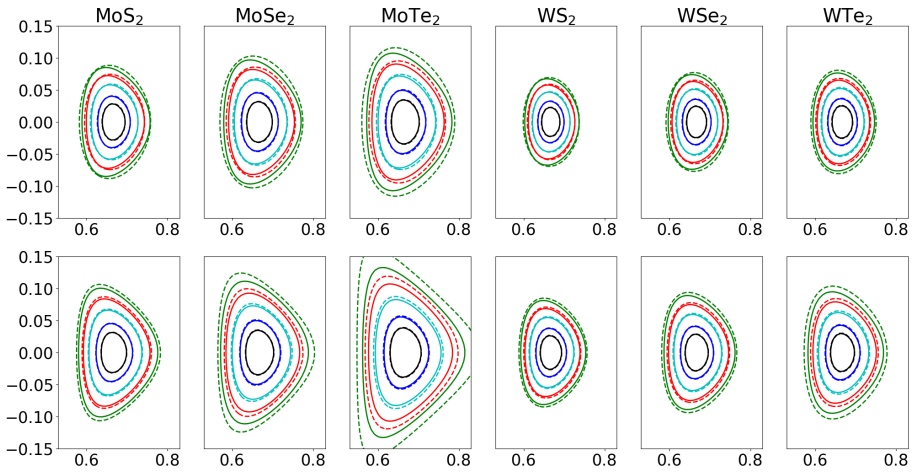


Figure B.12: MoX_2 and WX_2 isoenergy contours with $\mathbf{k} \cdot \mathbf{p}$ (solid lines) vs DFT (dashed lines) for spinless case at K valley. The energies (0.025, 0.05, 0.1, 0.15, 0.2 eV) are represented with (black, blue, turquoise, red and green lines).

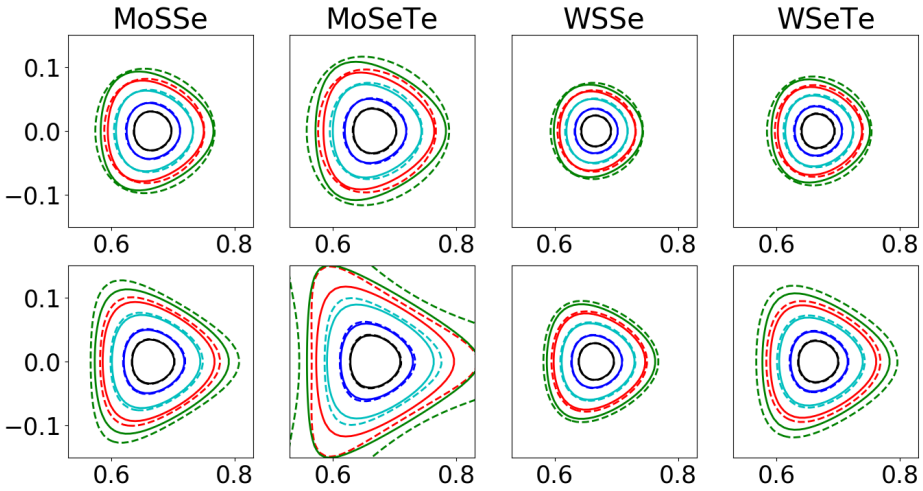


Figure B.13: MoXX′ and WXX′ isoenergy contours with $\mathbf{k} \cdot \mathbf{p}$ (solid lines) vs DFT (dashed lines) for spinless case at K valley. The energies (0.025, 0.05, 0.1, 0.15, 0.2 eV) are represented with (black, blue, turquoise, red and green lines).

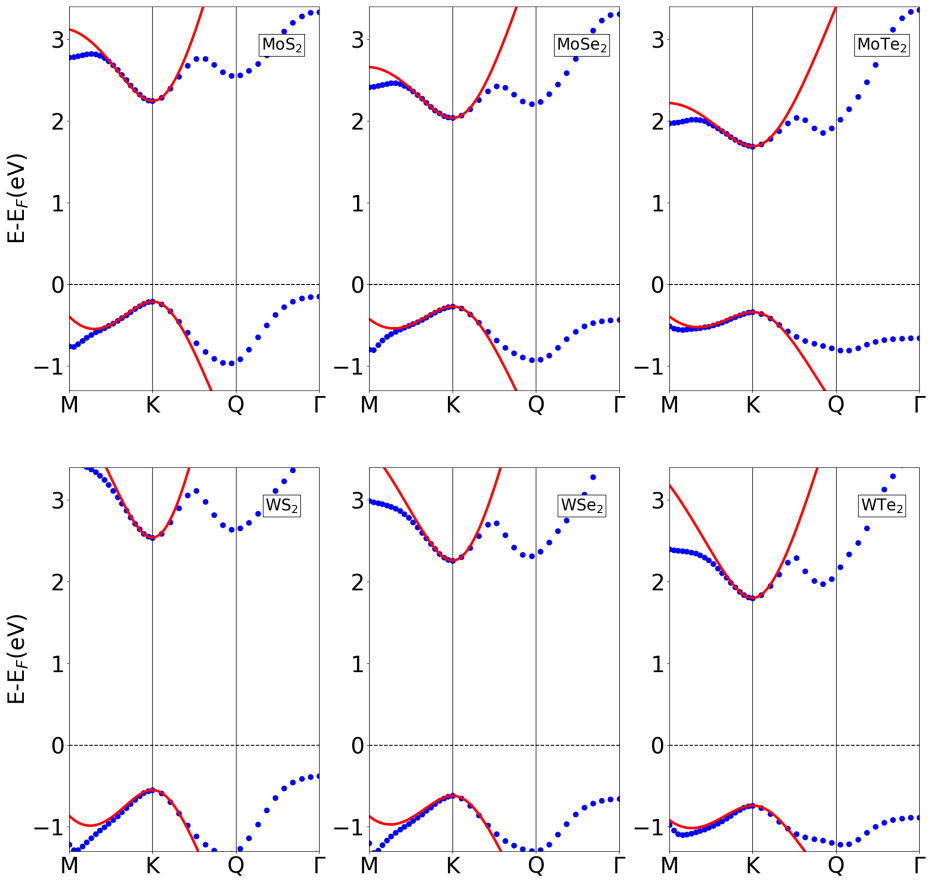


Figure B.14: MoX_2 and WX_2 spin up band structures with $\mathbf{k} \cdot \mathbf{p}$ (solid lines) vs DFT(•).

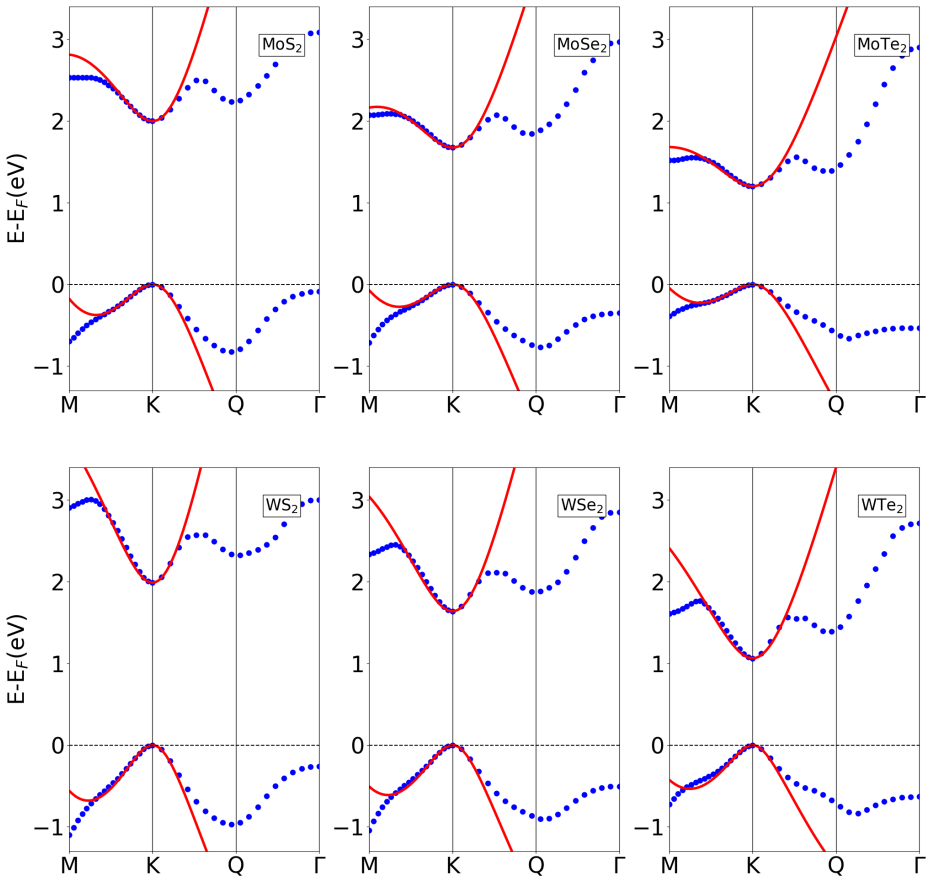


Figure B.15: MoX_2 and WX_2 spin down band structures with $\mathbf{k} \cdot \mathbf{p}$ (solid lines) vs DFT(•).

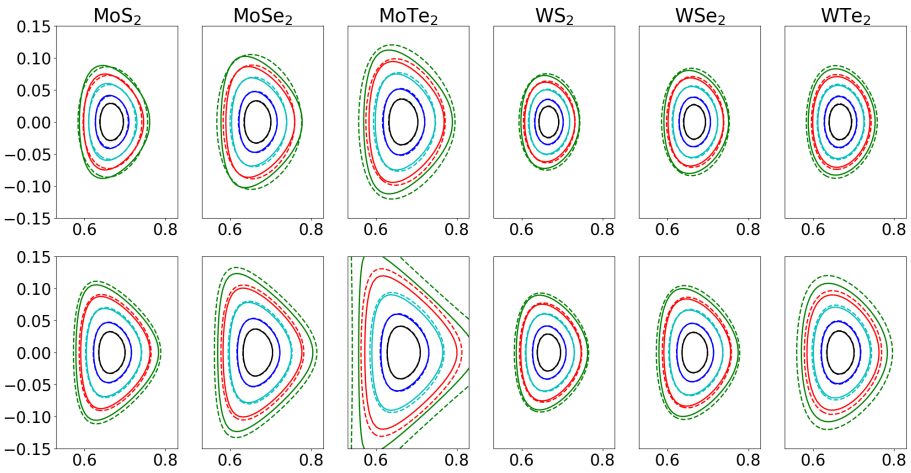


Figure B.16: MoX_2 and WX_2 isoenergy contours with $\mathbf{k} \cdot \mathbf{p}$ (solid lines) vs DFT (dashed lines) for spin up case at K valley. The energies (0.025, 0.05, 0.1, 0.15, 0.2 eV) are represented with (black, blue, turquoise, red and green lines).

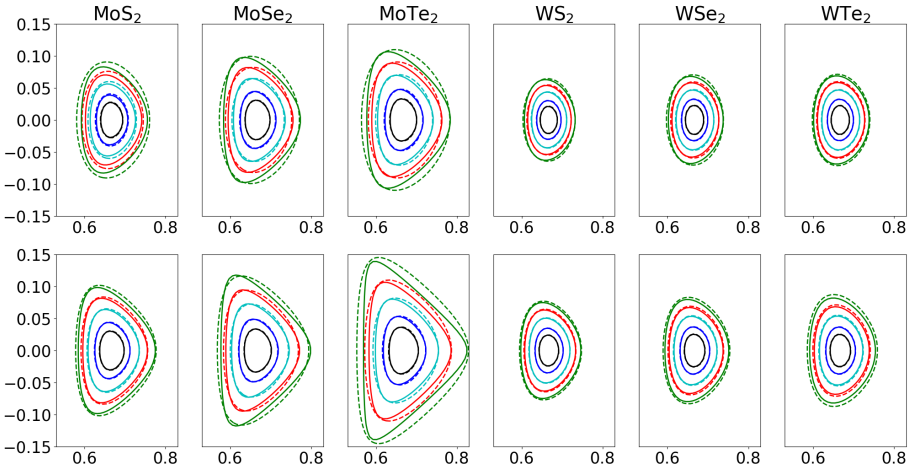


Figure B.17: MoX_2 and WX_2 isoenergy contours with $\mathbf{k} \cdot \mathbf{p}$ (solid lines) vs DFT (dashed lines) for spin down case at K valley. The energies (0.025, 0.05, 0.1, 0.15, 0.2 eV) are represented with (black, blue, turquoise, red and green lines).

B.5 Dichroism Results

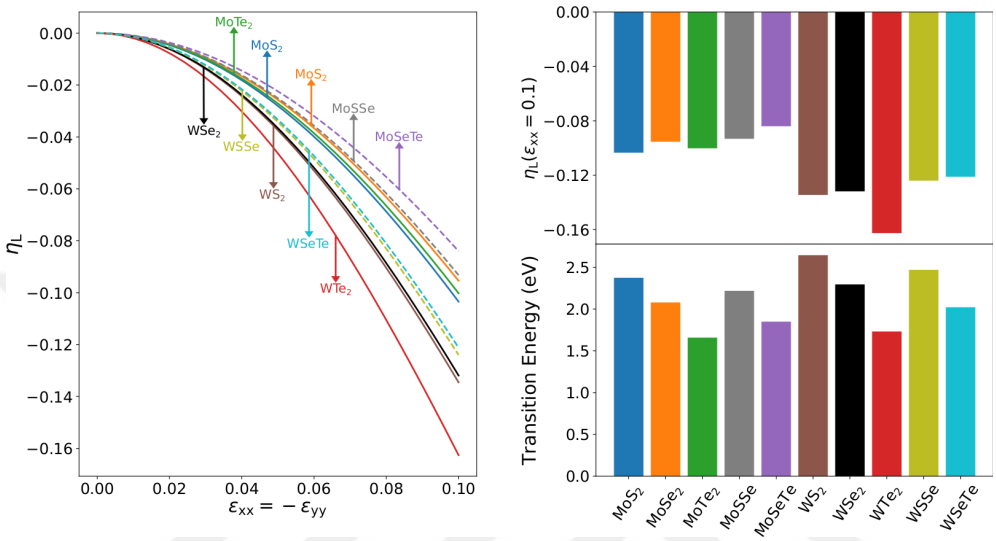


Figure B.18: The linear dichroism (with spinless Hamiltonian) variation under uniaxial-only strain at the K point (left). $\eta_L(\epsilon_{xx} = 0.1)$ and transition energy values for the ten (J)TMDs (right).

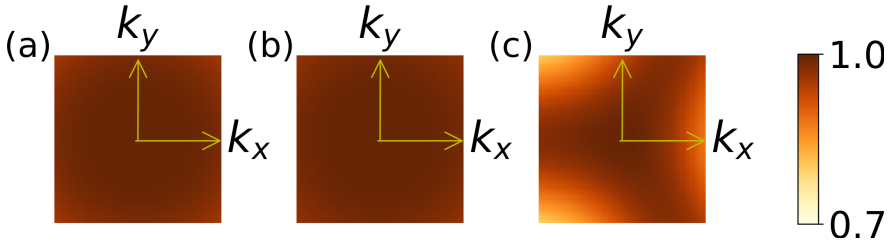


Figure B.19: In order to compare our results in Fig. 3.9(b) with Ref. [141], for monolayer MoS_2 without strain, circular dichroism (η_C) is calculated with including (a) only the symmetric and asymmetric terms (b) the trigonal warping term (c) all terms. $[-0.3, +0.3]$ square area around the K point in $\sqrt{3}/a$ units with a is the lattice constant along each direction is demonstrated.

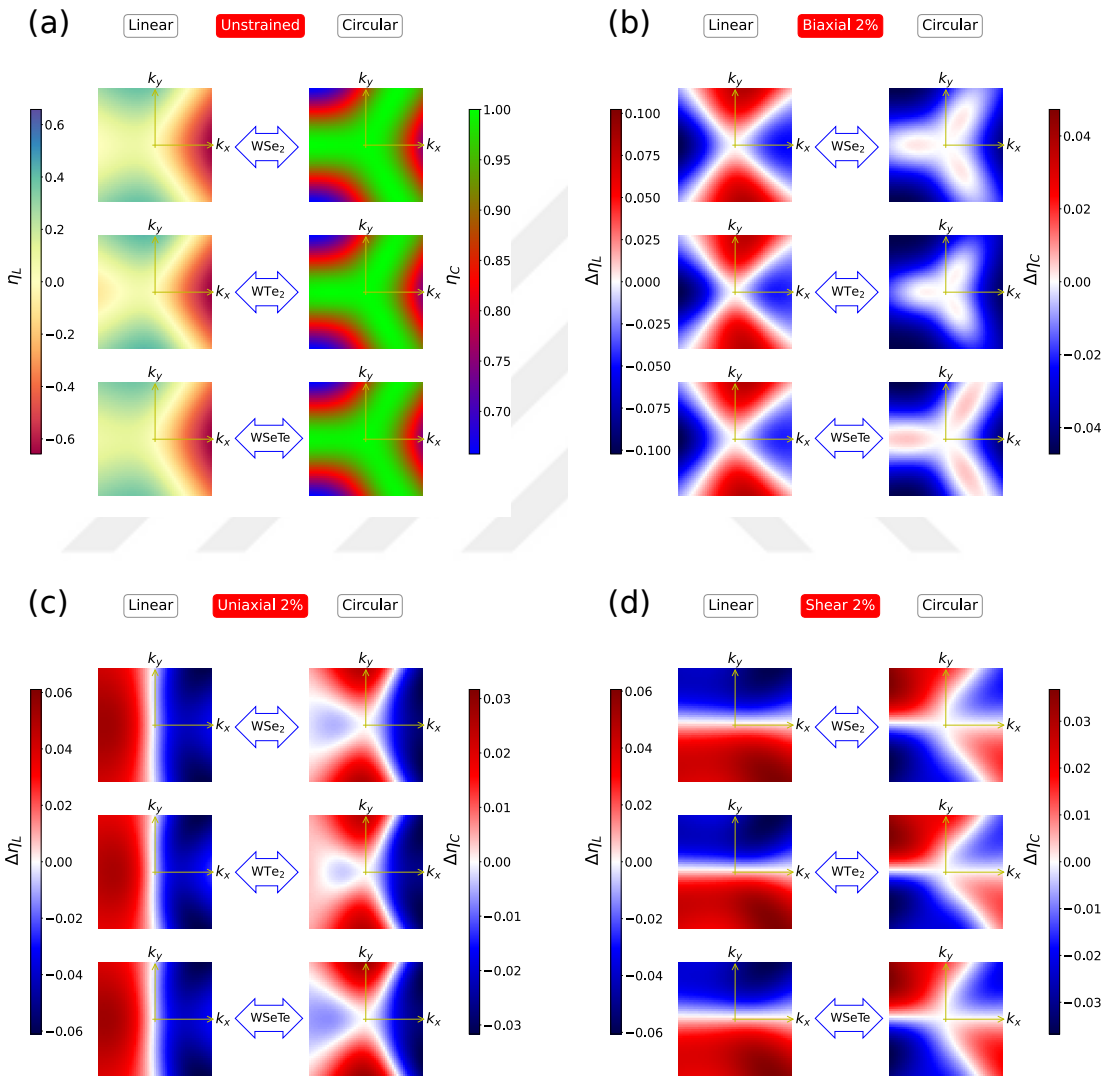


Figure B.20: For WSe_2, WTe_2, and janus WSeTe with spinless Hamiltonian, (a) the linear and circular dichroism variation ($\eta_{L,C}$) at K valley without strain and the deviation from unstrained case ($\Delta\eta_{L,C}$) at K point under (b) biaxial-only, (c) uniaxial-only, (d) shear-only strain.

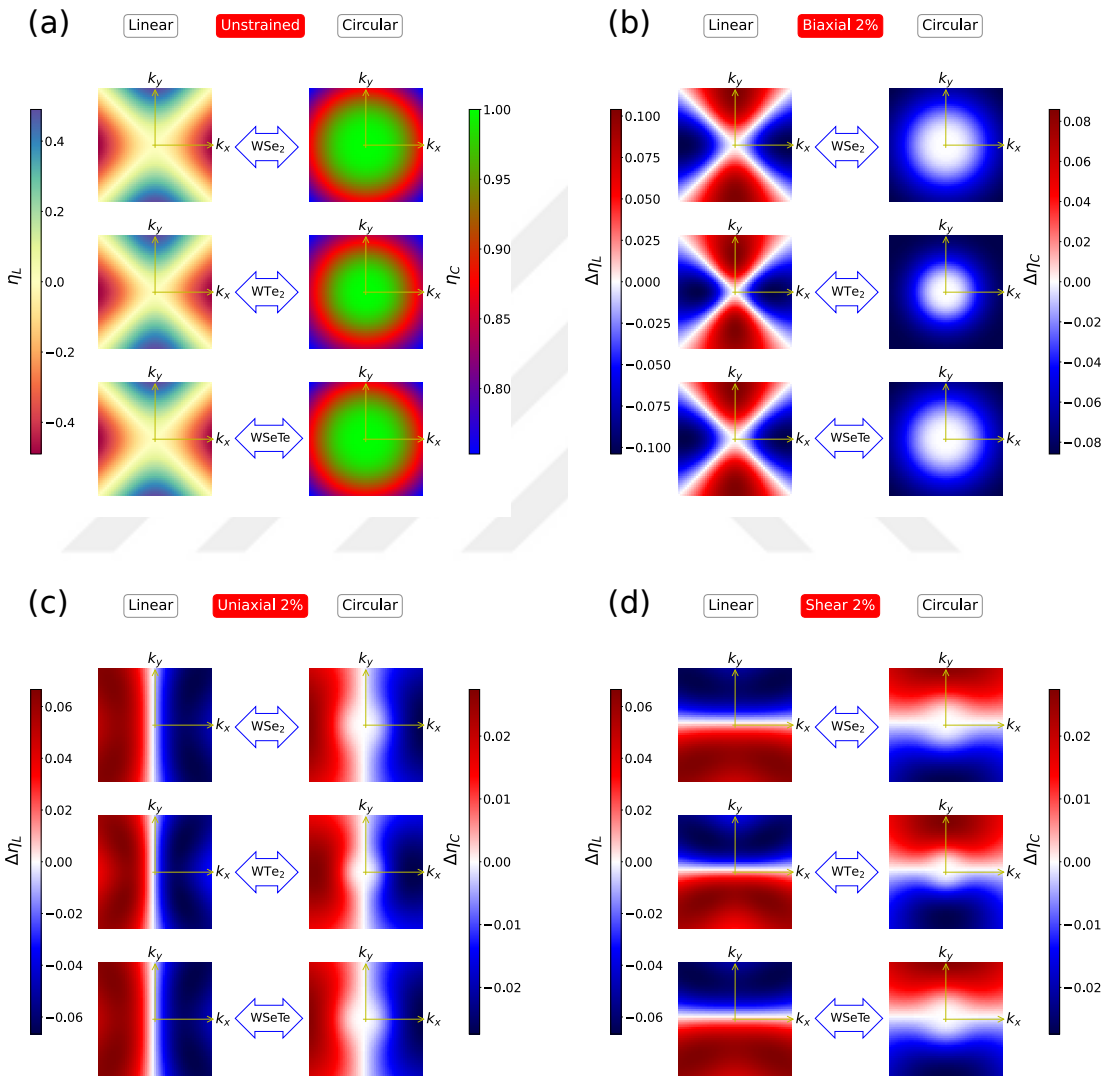


Figure B.21: For WSe_2, WTe_2, and janus WSeTe with only the symmetric term included for spin down transition, (a) the linear and circular dichroism variation ($\eta_{L,C}$) at K valley without strain and the deviation from unstrained case ($\Delta\eta_{L,C}$) at K point under (b) biaxial-only, (c) uniaxial-only, (d) shear-only strain.

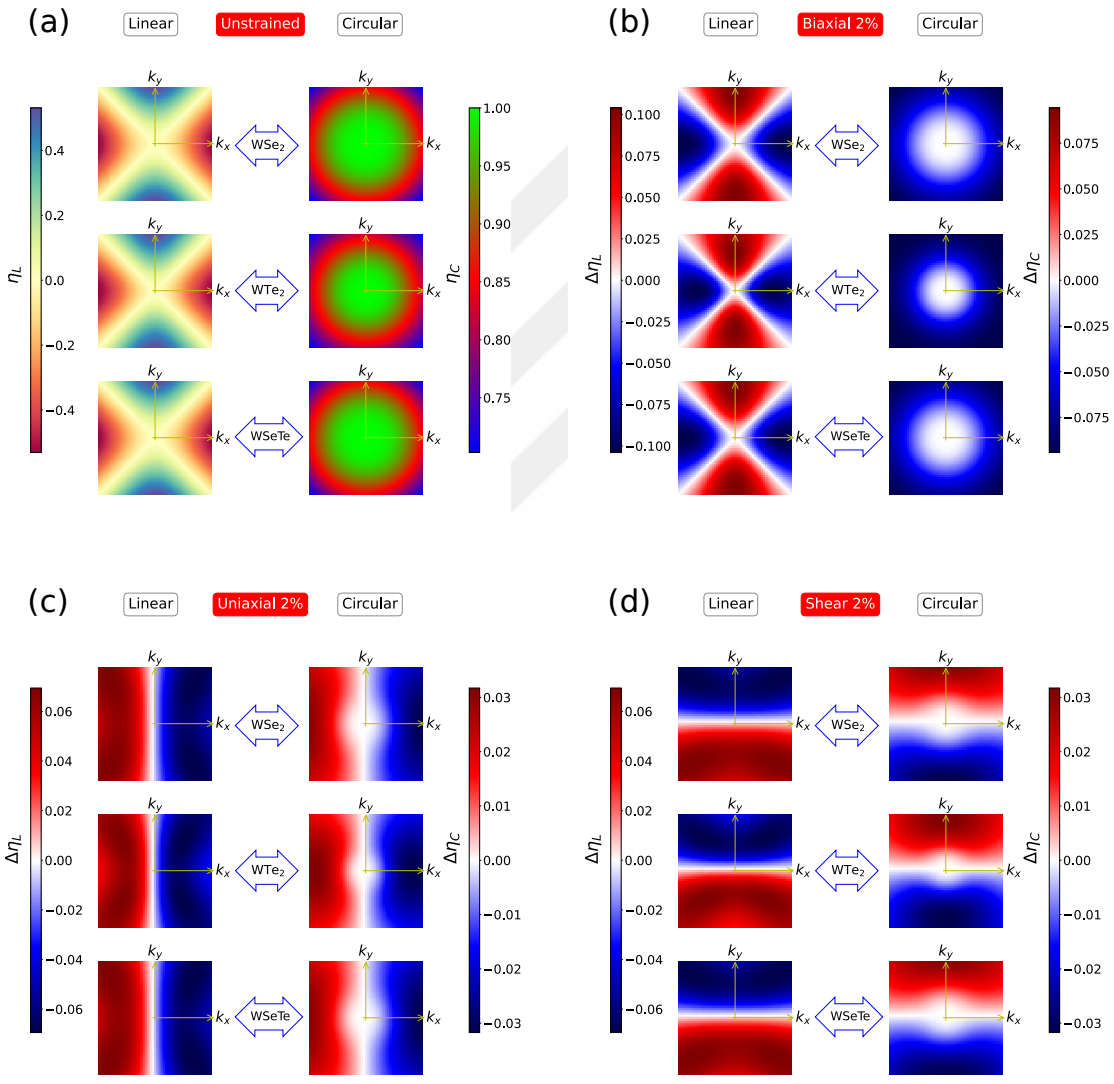


Figure B.22: Identical calculations are considered with previous figure, with symmetric and asymmetric terms of the $\mathbf{k} \cdot \mathbf{p}$ Hamiltonian are included together.

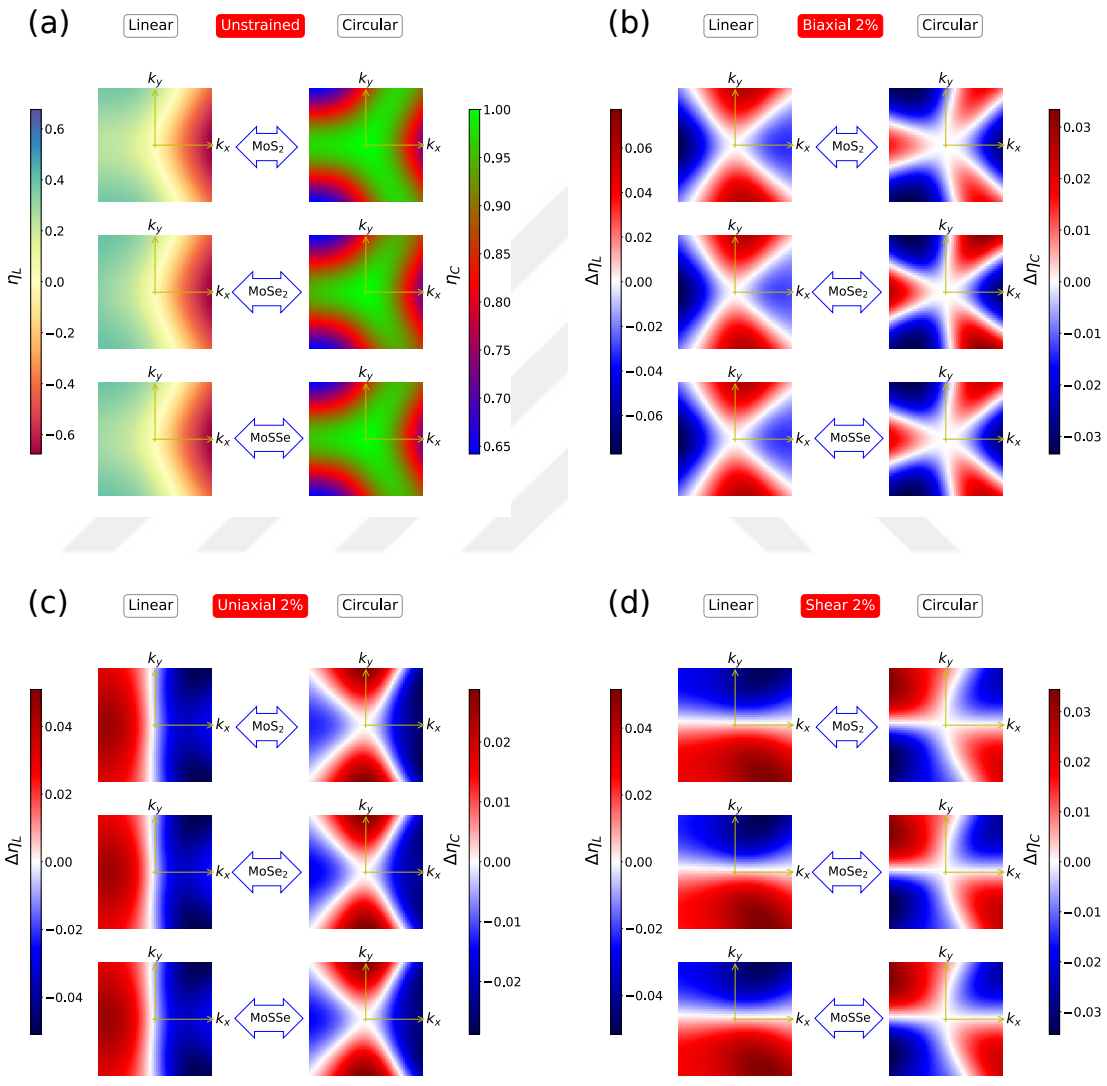


Figure B.23: For MoS_2, $MoSe_2$ and their janus MoSSe spin-down transition, (a) the linear and circular dichroism variation ($\eta_{L,C}$) at K valley without strain and the deviation from unstrained case ($\Delta\eta_{L,C}$) at K point under (b) biaxial-only, (c) uniaxial-only, (d) shear-only strain.

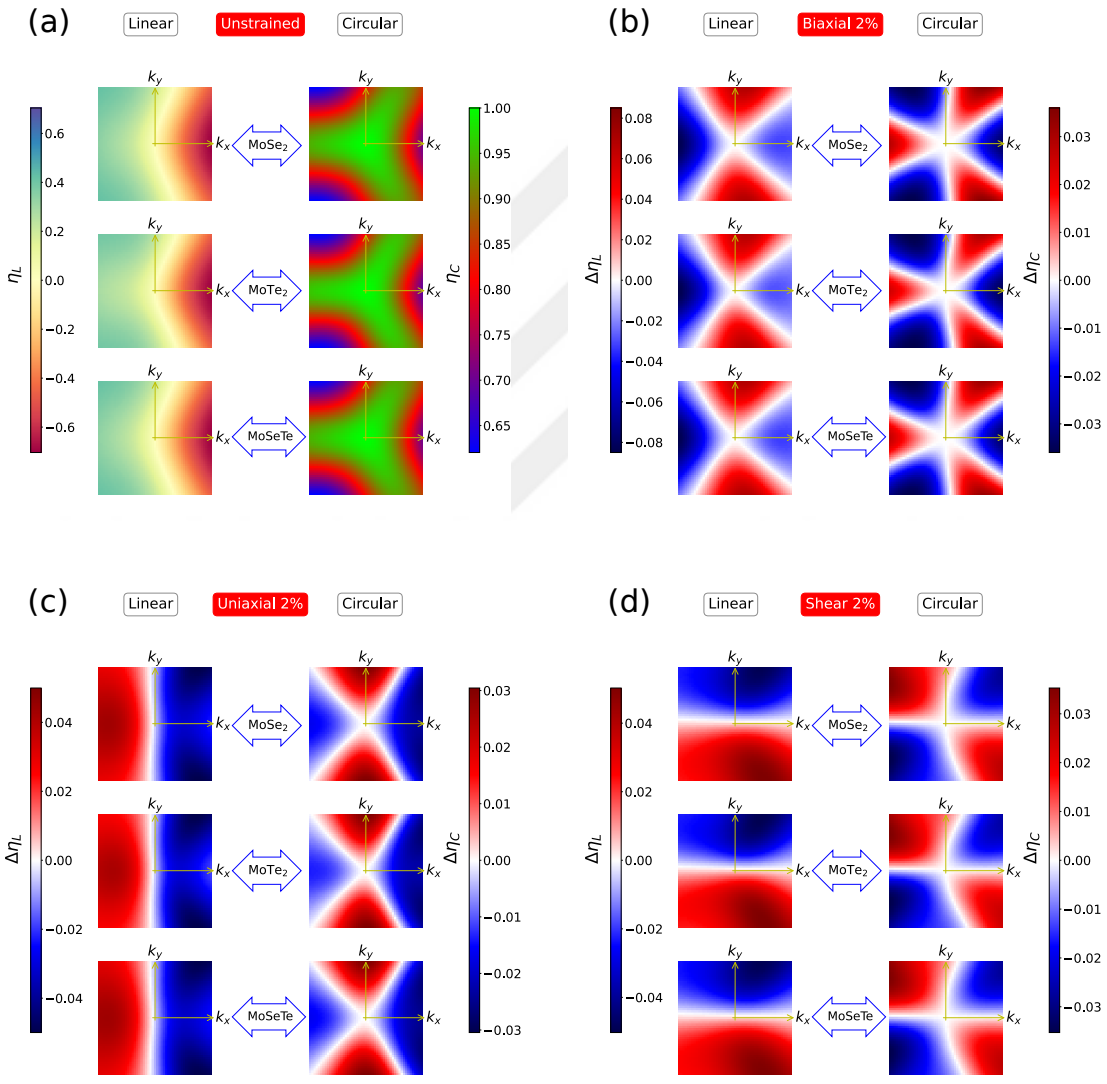


Figure B.24: Identical calculations are considered with previous figure, but for $MoSe_2$, $MoTe_2$ and their Janus MoSeTe.

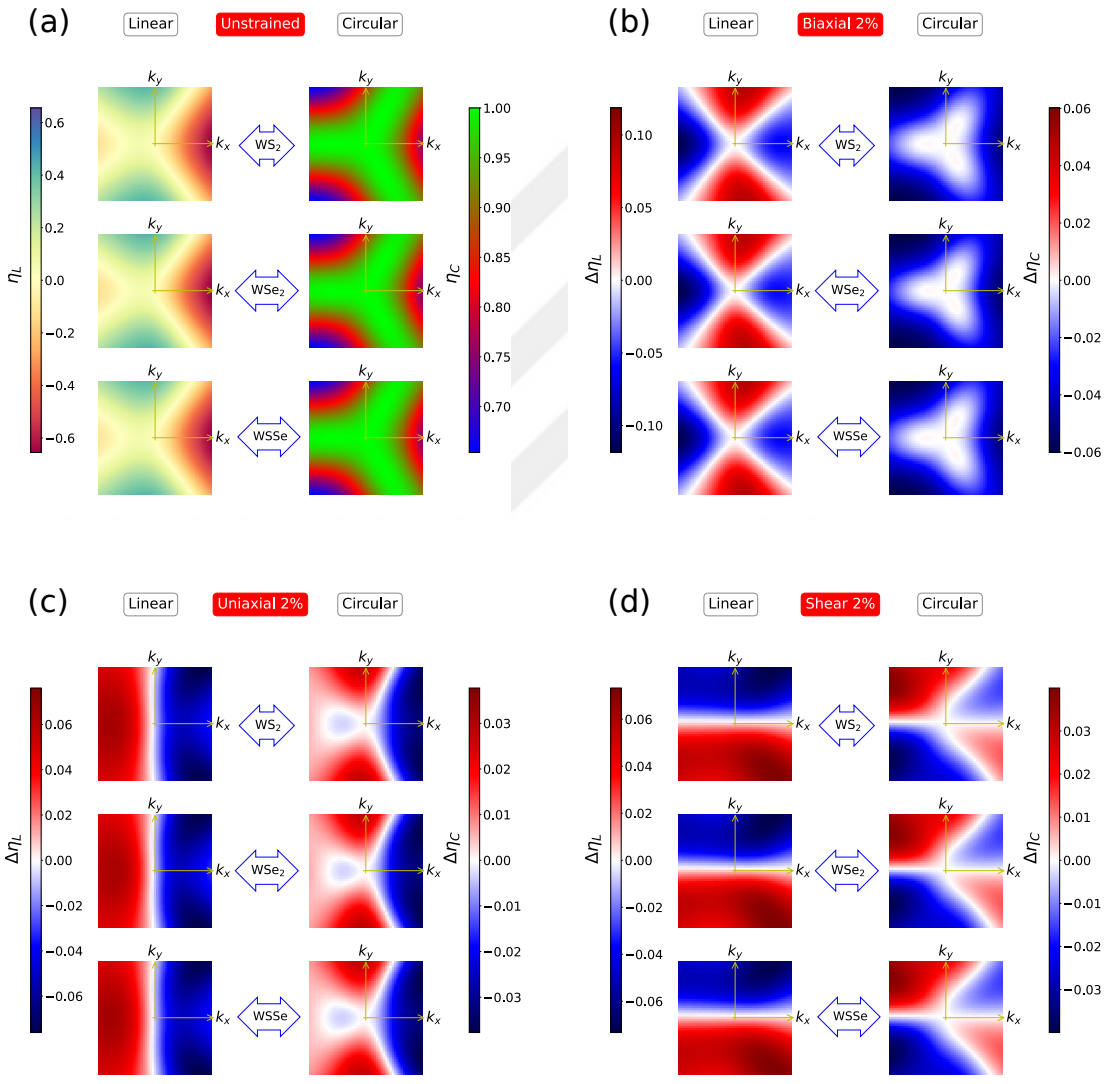


Figure B.25: Identical calculations are considered with previous figure, but for WS_2, WSe_2 and their Janus WSSe.

B.6 Effective Mass, DFT and k · p and Tables

Using the PBE results, electron and hole effective masses (m_v^*, m_c^*) have been calculated by fitting the curve around K (and Γ points for indirect band gap materials).

$$E(k) = \frac{\hbar^2 k^2}{2m^*} \tag{B.1}$$

is used for these calculations with a step size $\Delta = 0.01$ and presented in the Table B.1. It should be mentioned that, band switch is taken into consideration for WX_2 and WXY materials for spin dependent calculations.

Material	m*$_c$	m*$_v$	m*$_c$ (↑)	m*$_c$ (↓)	m*$_v$ (↓)	m*$_v$ (↑)
MoS_2	0.47	-0.58	0.50	0.44	-0.54	-0.62
$MoSe_2$	0.55	-0.65	0.59	0.51	-0.60	-0.71
$MoTe_2$	0.56	-0.69	0.60	0.51	-0.61	-0.77
WS_2	0.31	-0.41	0.36	0.27	-0.34	-0.49
WSe_2	0.34	-0.44	0.40	0.28	-0.35	-0.54
WTe_2	0.31	-0.42	0.37	0.24	-0.30	-0.53
MoSSe	0.53	-0.67	0.55	0.50	-0.61	-0.72
MoSTe	0.69	-4.34	0.68	0.67	-2.55	-1.66
MoSeTe	0.62	-0.83	0.65	0.58	-0.74	-0.93
WSSe	0.34	-0.46	0.42	0.28	-0.38	-0.56
WSTe	0.45	-2.72	1.05	0.28	-1.23	-1.42
WSeTe	0.37	-0.53	0.53	0.28	-0.42	-0.66

Table B.1: (J)TMD effective masses with and without SOC in units of m_0.

The band gaps are calculated (J)TMDs using PBE and HSE over PBE results for biaxial strain and uniaxial strain along x axis. Biaxial and uniaxial strain band gaps are given in Tables B.2-B.3 and B.4-B.5 for PBE and HSE, respectively. The smallest band gaps are chosen by the comparison between points KK. It should be noted that MoSTe and WSTe have indirect band gaps between ΓK.

Material	-2%	-1%	0%	1%	2%
MoS_2	1.91	1.79	1.67	1.56	1.46
$MoSe_2$	1.65	1.54	1.44	1.35	1.26
$MoTe_2$	1.25	1.16	1.08	1.00	0.93
WS_2	2.11	1.95	1.81	1.68	1.56
WSe_2	1.81	1.67	1.54	1.42	1.32
WTe_2	1.29	1.17	1.06	0.96	0.87
MoSSe	1.78	1.67	1.56	1.46	1.36
MoSTe	1.40	1.21	1.02	0.84	0.68
MoSeTe	1.46	1.36	1.27	1.18	1.10
WSSe	1.98	1.83	1.69	1.57	1.45
WSTe	1.68	1.45	1.23	1.02	0.83
WSeTe	1.60	1.47	1.34	1.23	1.13

Table B.2: Band gaps with -2%,-1%-0%,1%,2% biaxial strain (in eV units).

Material	-1%	0%	1%
MoS_2	2.28	2.14	2.01
$MoSe_2$	2.01	1.89	1.77
$MoTe_2$	1.61	1.50	1.40
WS_2	2.47	2.31	2.15
WSe_2	2.16	2.01	1.87
WTe_2	1.61	1.47	1.35
MoSSe	2.15	2.02	1.89
MoSTe	1.71	1.50	1.29
MoSeTe	1.82	1.70	1.59
WSSe	2.34	2.18	2.03
WSTe	1.96	1.71	1.48
WSeTe	1.93	1.79	1.65

Table B.3: Band gaps with biaxial strain and 0% strain with HSE over PBE (in eV units).

Material	-2%	-1%	0%	1%	2%
MoS_2	1.80	1.73	1.68	1.62	1.57
$MoSe_2$	1.55	1.49	1.44	1.39	1.35
$MoTe_2$	1.17	1.12	1.08	1.04	1.01
WS_2	1.95	1.89	1.82	1.75	1.69
WSe_2	1.61	1.62	1.55	1.48	1.44
WTe_2	1.18	1.12	1.07	1.01	0.98
MoSSe	1.66	1.62	1.56	1.51	1.47
MoSTe	1.17	1.12	1.02	0.93	0.85
MoSeTe	1.36	1.32	1.27	1.22	1.47
WSSe	1.75	1.77	1.70	1.63	1.58
WSTe	1.34	1.32	1.23	1.12	1.03
WSeTe	1.43	1.41	1.35	1.29	1.24

Table B.4: Band gaps with -2%,-1%-0%,1%,2% uniaxial strain (along x axis) (in eV units).

Material	-1%	0%	1%
MoS_2	2.21	2.14	2.07
$MoSe_2$	1.95	1.89	1.83
$MoTe_2$	1.56	1.51	1.45
WS_2	2.40	2.31	2.23
WSe_2	2.09	2.01	1.94
WTe_2	1.55	1.48	1.41
MoSSe	2.09	2.02	1.95
MoSTe	1.60	1.50	1.39
MoSeTe	1.76	1.70	1.65
WSSe	2.26	2.18	2.10
WSTe	1.81	1.72	1.60
WSeTe	1.87	1.79	1.72

Table B.5: Band gaps with uniaxial strain (along x axis) and 0% strain with HSE over PBE (in eV units).

	f_4 (PBE)	f_4 (HSE)	f_5 (PBE)	f_5 (HSE)
MoS_2	-2.69	-3.29	2.64	2.57
$MoSe_2$	-2.35	-2.94	2.22	2.17
$MoTe_2$	-1.92	-2.43	1.82	1.77
WS_2	-3.26	-3.82	3.31	3.22
WSe_2	-2.97	-3.53	2.84	2.77
WTe_2	-2.49	-2.99	2.35	2.29
MoSSe	-2.52	-3.10	2.35	2.29
MoSeTe	-2.16	-2.69	1.87	1.82
WSSe	-3.12	-3.68	2.99	2.90
WSeTe	-2.79	-3.32	2.41	2.35

Table B.6: $\mathbf{k} \cdot \mathbf{p}$ parameters f_4 and f_5 calculated based on PBE and HSE results (in eV units).